The Influence of Fuel Sulfur on the Operation of Large Two-Stroke Marine Diesel Engines

Cordtz, Rasmus Faurskov

Publication date:
2015

Document Version
Publisher's PDF, also known as Version of record

The Influence of Fuel Sulfur on the Operation of Large Two-Stroke Marine Diesel Engines

PhD Thesis

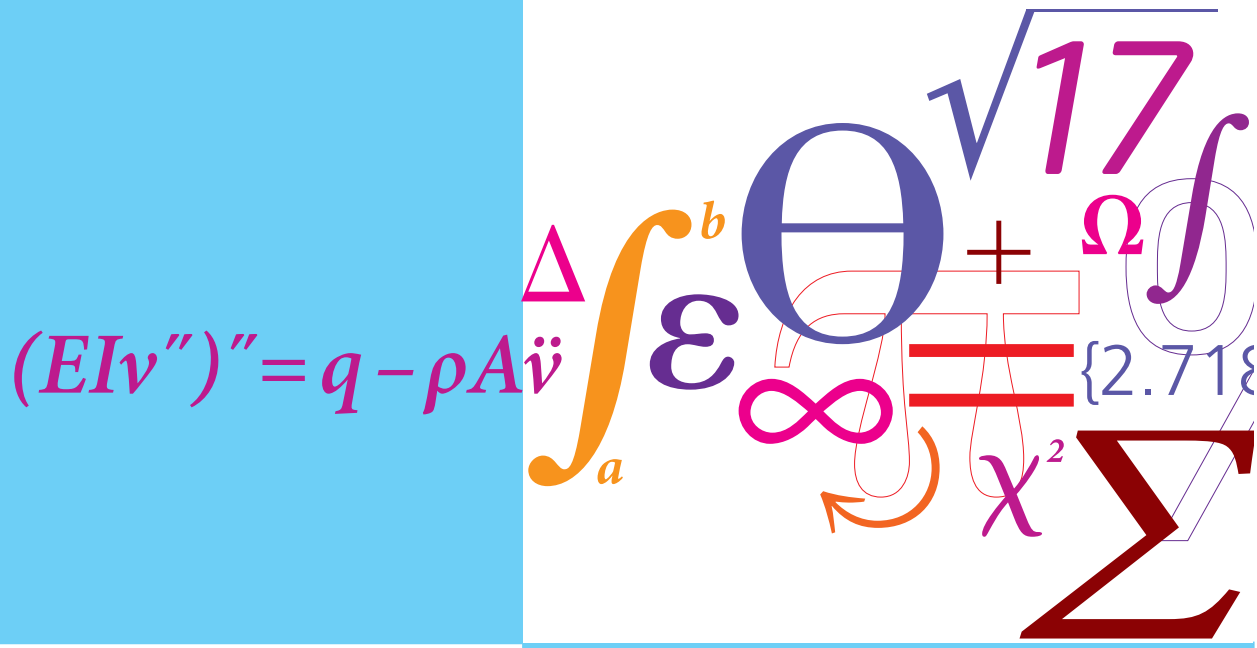

Rasmus Faurskov Cordtz
DCAMM Special Report No. S185
January 2014

DTU Mechanical Engineering
Department of Mechanical Engineering

The Influence of Fuel Sulfur on the Operation of Large Two-Stroke Marine Diesel Engines

By

Rasmus Faurskov Cordtz

A thesis submitted in partial fulfillment of the requirements for the degree of

DOCTOR OF PHILOSOPHY

at the

TECHNICAL UNIVERSITY OF DENMARK

2015

The Influence of Fuel Sulfur on the Operation of Large Two-Stroke Marine Diesel Engines

Rasmus Faurskov Cordtz

Section of Thermal Energy
Department of Mechanical Engineering
Technical University of Denmark
Nils Koppels Allé, Bld. 403
DK-2800 Kgs. Lyngby
Denmark

Ph.D. Thesis

ISBN: 978-87-7475-421-3
DCAMM Special Report no.: S185

Preface

The present thesis is submitted for the partial fulfillment of the PhD degree at the Technical University of Denmark (DTU). The PhD program is carried out at the Department of Mechanical Engineering under the Section of Thermal Energy from September 2010 to January 2014 and included a four months leave. The study is funded by The Technical University of Denmark and the research School DCCAM (Danish Center for Applied Mathematics and Mechanics) and MAN Diesel & Turbo.

The author would like to thank my supervisor Associate Professor Jesper Schramm and colleague Professor Peter Glarborg (DTU) as well as employees at MAN Diesel and Turbo, especially Stefan Mayer, Svend S. Eskildsen and Anders Andreasen for their guidance and support throughout the study. The author is also very grateful for the support offered by PENTOL GmbH that with their SO_3 monitor supported the SO_3 measurement campaign with a heavy duty diesel engine at Rostock University (Lehrstuhl für Kolbenmaschinen und Verbrennungsmotoren). Special thanks are addressed to CEO Olivier Blauenstein, employee Dirk Bogenschneider (PENTOL) and Dr.-Ing. Jean Rom Rabe (Rostock University). The author appreciate the numerous and inspiring discussions with my colleagues at DTU and the patient and caring support from my Joan.

Rasmus Cordtz
Kgs. Lyngby January 2014

Abstract

Cold corrosion of cylinder liners in large low speed two-stroke marine diesel engines is an issue that has gained increasingly interest over the last years. It is believed that the corrosion is primarily caused by sulfur trioxide (SO_3) that is formed from the oxidation of fuel sulfur. Following the SO_3 condenses on the liner surface as aggressive sulfuric acid (H_2SO_4) when the liner temperature is less than the sulfuric acid dew point. To counteract corrosion cylinder liner lubricants are blended with base additives. Controlling corrosion rates are challenging and expensive. Furthermore completely avoiding corrosion is unwanted as mild levels of corrosion is sought to improve conditions of the lubricant film between the moving piston and the liner. The present work focusses on in cylinder SO_3 formation and subsequent H_2SO_4 condensation on the cylinder liner of a large marine engine. Formation of SO_3 is investigated theoretically with a phenomenological multizone engine model that applies a detailed sulfur reaction mechanism. Results show that generally a few percent of the fuel sulfur is converted to SO_3 and the remaining sulfur leaves the engine as sulfur dioxide (SO_2). Model trends agree with experiment work. From a fully homogenized cylinder gas the sulfuric acid dew point trace is calculated by implementing H_2O-H_2SO_4 vapor liquid equilibrium. Theory that couples heat and diffusive mass transfer in the gas species boundary layer adjacent to the liner surface is applied to analyze the characteristics of sulfuric acid condensation. Higher operating pressures and fuel sulfur contents act to increase the deposition that is very sensitive to the applied liner temperature.

Resume

Koldkorrosion af cylinderforinger i store langsomtgående to-takts marine-dieselmotorer har i de seneste år fået meget opmærksomhed som følge af ændrede driftsbetingelser og deraf øgede korrosionsrater. Det menes, at korrosionen skyldes svovltrioxid (SO_3), der dannes ved oxideringen af brændstoffets svovl. Efterfølgende kondenserer SO_3 på foringsoverfladen som aggressiv svovlsyre (H_2SO_4), når overfladetemperaturen er lavere end syredugpunktet. For at hæmme korrosion er smøreolien tilsat basiske komponenter, men det er vanskeligt og dyrt at styre korrosion i praksis. Samtidig ønskes en mild grad af korrosion, der menes at forbedre smøreegenskaberne mellem cylinderforingen og det bevægelige motorstempel. Nærværende afhandling omhandler SO_3-dannelse og følgende H_2SO_4 kondensering på cylinderforingen i en stor langsomtgående to-takts marine-dieselmotor. SO_3-dannelsen er teoretisk behandlet vha. en fænomenologisk multizone simuleringsmodel, der involverer en detaljeret svovl-reaktionsmekanisme. Ifølge modellen omdannes generelt kun få procent af brændstoffets svovl til SO_3, og resten udledes som svovldioxid (SO_2). Modeltrends stemmer overens med resultater fra en række motoreksperimenter. Med udgangspunkt i en homogen cylindergas er svovlsyredugpunkter beregnet vha. H_2O-H_2SO_4 faseligevægt. Koblet varme og diffusionsteori er anvendt til at analyseres egenskaber for svovlsyrekondensering på cylinderforingen. Øget cylindertryk og brændstof-svovlindhold forøger kondensering, der ligeledes er meget følsom over for den anvendte foringstemperatur.

Contents

1. Introduction

Over 90% of the world trade is carried by the international shipping industry. Without shipping the import and export of goods on the scale necessary for the modern world would not be possible. Every year several billion tons of trades are moved primarily by large container ships that often operate on large low speed two-stroke engines. These engines offer high power densities in the megawatt range with thermal efficiencies up to 55% and burn Heavy Fuel Oil (HFO) for many hours a year. HFO is basically the residue from fuel oil refineries and the maritime industry heavily stresses the global environment in terms of air pollution and greenhouse effects. In operation the ships emit significant levels of carbon dioxide (CO_2), particulate matter (PM) also known as soot, nitrogen oxides (NO_x) and sulfur oxides (SO_x). Emissions of NO_x and PM are poisonous and carcinogenic and are subject to international legislations. In large marine engines NO_x formation is a consequence of the efficient low speed process and in near future additional technologies such as Exhaust Gas Recirculation[1] (EGR) and Selective Catalytic Reduction[2] (SCR) are likely combined to meet ever more demanding NO_x legislations. SO_x emissions are the principle cause of acid rain and reduce in line with the fuel sulfur content. Current and future SO_x-legislations that are set by the International Maritime Organization (IMO) are presented in Figure 1.1. The figure presents two SO_x-limits. A global limit and yet a limit that applies to the so called Emission Controlled Areas (ECA's) representing e.g. the North Sea area, the Baltic Sea area, sea ports and near coast areas. Ships that operate outside the ECA's are currently allowed to operate with fuels containing up to 3.5 wt. %. In ECA areas the current limit is 1 wt. % but from 2015 the limit will be as low as 0.1 wt. %. The limits apply unless exhaust gas cleaning is carried out onboard. This can be realized by the use of scrubbers that with seawater can wash out SO_x and other impurities from the exhaust gas.

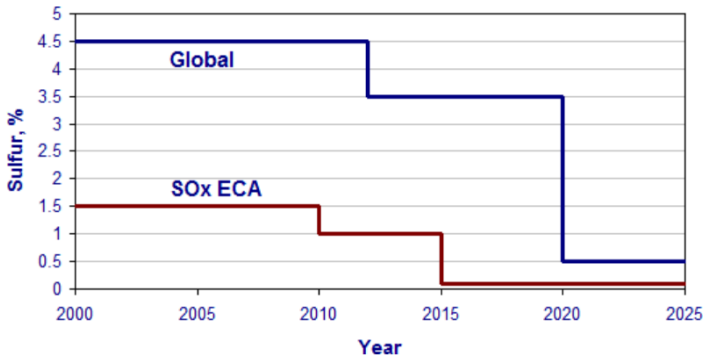

Figure 1.1. Sulfur limits according to the International Maritime Organization[3].

Besides sparing the global environment a reduction of the fuel sulfur content will serve to extend the engine and exhaust system life time. Especially the lifetime of the cylinder liner is affected by the fuel sulfur. The cast iron liner on which the engine piston travels as illustrated in Figure 1.2 is prone to abrasive and corrosive wear. The latter wear type is the dominant[4,5] and is caused by corrosive species that forms in the cylinder gas especially when the fuel contains sulfur. During combustion the fuel sulfur is oxidized to SO_2 from which a fraction is further oxidized to SO_3. High concentrations of water vapor are also present in the combustion products and is known to form gaseous sulfuric acid (H_2SO_4) from a direct reaction with SO_3. The presence of H_2SO_4 implicates elevated dew points and in practice liquid sulfuric acid H_2SO_4 is believed to condense together with water as a corrosive sulfuric acid mixture on the cooled liner although the surface temperature is in the order of ≈170 - 210 °C. The liner temperature increases typically with the engine load but is limited by a maximum lube oil operating temperature. If the temperature gets too high the lube oil film may oxidize or break down. This would lead to engine failure from sudden severe wear as the hydrodynamic lubrication between the liner and the piston can no longer be maintained.

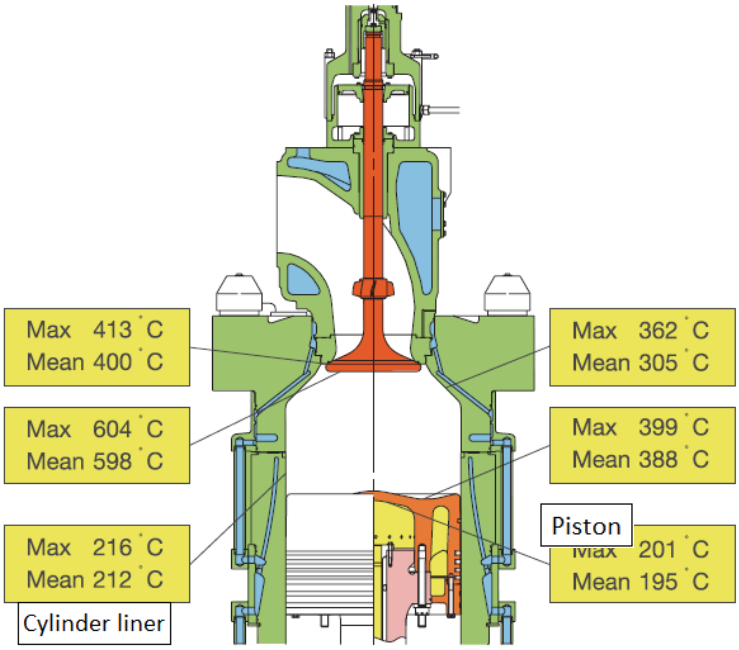

Figure 1.2. MAN B&W K98 engine combustion chamber temperatures

Besides separating the sliding piston from the static cylinder liner the lube oil protects the liner from corrosive attack by means of base additives blended in the oil to neutralize deposited acid. The base strength of the lube oil is expressed by the Total Base Number (TBN) that is a measure of reserve alkalinity that is defined as the quantity of Potassium Hydroxide (KOH) equivalent. A typical fresh two-stroke marine engine lube oil is formulated with a TBN of 70. This corresponds to 70 mg

KOH/ g oil. In large two stroke engines the lube oil is typically supplied via quills in the cylinder liner and is distributed by the reciprocating piston/piston rings. However if the dosing and the distribution of lube oil is not adequate corrosive attack may occur on the liner surface. In addition products of corroded iron (FeOH, $FeSO_4$) and calcium compounds (that perform the major part of the acid neutralization) may build up and contribute to abrasive liner wear[6]. Lubricant dosing is normally in the order of 1 gram per break horse power. Higher dosing rates can result in the buildup of excessive amounts of calcium compounds around the piston ring pack that may scrape of the oil film and provide scuffing (direct metal to metal contact). To avoid scuffing it seems logic to reduce the TBN and lube oil feed rate according to the fuel feed rate and sulfur content, but in reality the answer is not that simple and new lube oil formulations are likely needed in the future to cope with e.g. lower fuel sulfur contents. Throughout the years the design of large marine engines has been modified in order to fulfill increasing demands with respect to cruising speed. However as the fuel prices soared around 2007 many ship owners decided to operate at lower speeds/power outputs and today the fleet is generally ”slow steaming”. This means that the engine power is typically less than 40% which has a positive influence on freight costs and unwanted gas emissions. Yet the “sudden” power reduction has led to problems concerning the lifetime of cylinder liners that now corrode too fast unless the lube oil feed rate is significantly increased. This procedure is impractical as well expensive and more advanced methods that correlate the dosing strategy with operational conditions are generally needed. Moreover the ideal situation is not to avoid liner corrosion completely as was best formulated by Aabo[4]

> *It has been established that a certain level of controlled corrosion enhances lubrication, in that the corrosion (removal of iron) generates small “pockets” in the cylinder liner running surface from which hydrodynamic lubrication from the oil in the pocket is created. The alternative, no corrosion, could lead to bore-polish and, subsequently, hamper the creation of the necessary oil film on the liner surface resulting, eventually, in accelerated wear such as scuffing.*

Online inspections of iron content in drained lube oil[7] can give some insight about the level of liner corrosion. However corrosion is a long term process and not easily correlated directly to the current engine operating conditions. To complicate things further the fuel sulfur content may alter significantly from one fuel bunker to another. Online SO_3 measurements may offer another indirect measure of liner corrosion but the challenging nature of the reactive SO_3 gas has shown to complicate measurements. So far reported results of SO_3 measurements in the exhaust gas of large marine engines are surprisingly absent in the literature. The measurements by Engel[8] seem to be the

only peer reviewed experiments. However Engel only measured SO_3 in the exhaust gas from heavy duty diesel engines (not marine engines) and reported that ~1-8 % of the fuel sulfur is converted to SO_3 depending on the fuel type and operating conditions. This may explain the "rule of thumb" that states that a few percent of the fuel sulfur is converted to SO_3 in a large marine engine as well. However it remains to be reported how SO_3 formation is altered by key parameters such as engine speed, pressure and air-fuel ratio. This is addressed in the present work through a phenomenological model of a large marine engine and a series of SO_3 measurements with a heavy duty test engine. The diesel combustion process combined with chemical reactions can be modeled with different levels of complexity. Computational Fluid Dynamic tools (CFD) are highly advanced and offer detailed information about the complex, multiphase and heterogeneous combustion process. A significant drawback associated with CFD tools however is the computational time required for solving conservation laws of species, momentum and energy through partial differential equations in a 3D domain including chemical sub models. The computational time is typically more than $10^{\wedge 5}$ seconds and is not practical for investigating SO_3 formation in multiple operational conditions. In order to provide a much faster and a fairly detailed model a phenomenological multizone engine model is formulated in this study. Different formulations of this model approach exist in the literature[9]. This work is inspired by the formulation suggested by Andersson[10]. The model is simple compared to CFD tools as it solely solves ordinary differential equations with respect to time and disregards conservation laws with respect to space. But since it is a 0D model the computational time is in the order of $10^{\wedge 2}$ seconds which makes it flexible and suitable for multiple simulations. However the multizone model also fails in predicting "true" gas mixing and turbulence etc. On the other hand with the phenomenological approach the effect of mixing can be induced and thereby evaluated as shown in this work.

The sulfur chemistry has been intensively investigated theoretically[11-17] and experimentally[11,18-22] over the years. Focus on atmospheric sulfur chemistry has provided valuable information about H-S-O complexes and today the sulfur chemistry is considered a well-established science. In the field of power plants and gas turbines SO_3 formation has been studied both theoretically and experimentally[23-28]. It is known that SO_2 is the primary sulfur compound in a combustion process and a fraction of the SO_2 is further oxidized to SO_3 through several reaction pathways involving species of the radical pool and H-S-O complexes. In this work a detailed sulfur reaction mechanism is applied in order to simulate SO_3 formation that is shown to form primarily as the hot gas products cool during expansion stroke.

2. Objective

The aim of this work is to quantify the formation of gaseous SO_3/H_2SO_4 in the cylinder of a large low speed two-stroke marine diesel engine operating on HFO including sulfur and model sulfuric acid condensation on the cylinder liner. For the purpose a phenomenological multizone engine model that applies a detailed sulfur reaction mechanism will be formulated. To simplify computations the multizone model solely considers homogenous gas reactions and disregards multiple phases i.e. liquid fuel and solid matter. Moreover the HFO is modeled as n-dodecane including non-bonded elemental sulfur. The large low speed two-stroke engine specified in Table 4.1 serves as the reference engine for the engine model. In order to simulate realistic fuel burn rates the model will apply experimental operating data such as cylinder pressure histories of the full operational range. The lack of experimental SO_3 exhaust gas data necessitates that the model is calibrated against available NO_x data. For the purpose a simple correlation of mixing between burned fuel products and fresh gas (mostly air) will be proposed. The multizone model will be formulated in MATLAB where chemical reaction rates (species formation) are integrated via the open source software CANTERA[29,30] that is directly compatible with MATLAB. With CANTERA the thermodynamic properties of gas species are expressed through 7 coefficient NASA polynomials and CANTERA efficiently calculates thermodynamic compositions, properties and temperatures etc. of gas mixtures through available subroutines.

By implementing theory that couples heat and diffusive mass transfer the multizone model will be used to predict the rate of sulfuric acid condensation on the cylinder of a marine engine in multiple operating conditions. Condensation takes place if the liner temperature is less than the sulfuric acid dew point that is determined by implementing H_2O-H_2SO_4 VLE.

In order to compare model results with experimental data a comprehensive study of SO_3 formation in a diesel engine that operates on HFO including sulfur will be carried out. To keep the experimental costs at a reasonable level the measurements will be carried out with a fully mapped heavy duty (kilowatt) test engine instead of a large (megawatt) marine engine. Proven techniques for measuring SO_3 in the exhaust gas will be reviewed and the best option will be used.

3. Sulfur chemistry

In order to model the distribution of sulfur compounds in the cylinder gas a detailed sulfur reaction mechanism[11] is applied. The mechanism is the result of a comprehensive literature review, laboratory reactor experiments and theoretical predictions[18,31-34]. It comprises over 130 elementary reactions and more than 30 species divided into three subsets; a sulfur subset, a H_2/O_2 subset and a CO/CO_2 subset. The latter two subsets govern the oxidation of the hydrocarbons in the fuel. Table 3.1 lists important high temperature SO_x-reactions where the O and OH radicals act as key species in terms of SO_2 to SO_3 oxidation[11]. $HOSO_2$ acts as an intermediate component and "opens" an important pathway to SO_3.

Reaction No.	Reaction	A	n	E/R
77	$SO + O_2 \leftrightarrow SO_2 + O$	7.6E3	2.37	2970
86	$SO_2 + O(+M) \leftrightarrow SO_3(+M)$[a]	3.7E11	0.00	1689
	Low-pressure limit	2.4E27	-3.60	5186
	Troe parameters 0.442, 316, 7442			
88	$SO_2 + OH(+M) \leftrightarrow HOSO_2(+M)$[b]	5.7E12	-0.27	0
	Low-pressure limit	1.7E27	-4.09	0
	Troe parameters 0.10, 1E-30, 1E30			
89	$SO_2 + SO_2 \leftrightarrow SO_3 + SO$	5.0E07	2.00	37750
90	$SO_3 + H \leftrightarrow SO_2 + OH$	8.4E09	1.22	2980
92	$SO_3 + O \leftrightarrow SO_2 + O2$	2.8E04	2.57	29200
93	$SO_3 + OH \leftrightarrow SO_2 + HO_2$	4.8E04	2.46	13700
130	$HOSO_2 \leftrightarrow SO_3 + H$	1.4E18	-2.91	54900
131	$HOSO_2 + H \leftrightarrow SO_2 + H_2O$	1.0E12	0.00	0
132	$HOSO_2 + O \leftrightarrow SO_3 + OH$	5.0E12	0.00	0
133	$HOSO_2 + OH \leftrightarrow SO_3 + H_2O$	1.0E12	0.00	0
134	$HOSO_2 + O_2 \leftrightarrow HO_2 + SO_3$	7.8E11	0.00	656

[a]Enhanced third-body coefficients: $N_2 = 0$, $SO_2 = 10$, $H_2O = 10$

[b]Enhanced third-body coefficients: $N_2 = 1$, $SO_2 = 5$, $H_2O = 5$

Table 3.1. High temperature SO_x reactions. Arrhenius parameters in cal, cm, mol, s, K for $k = AT^{\beta}exp(-E/RT)$. Reaction numbers refer to the full reaction mechanism.

The SO_x chemistry in the sulfur subset is decoupled from any NO_x interactions although the oxidation of SO_2 may proceed from a reaction involving NO_2. Nevertheless, reactions between NO_x and SO_x are ignored as NO_2 formation is negligible in large low speed diesel engines[35] and

since direct S/N interactions remain controversial[31]. Neither does the applied sulfur subset contain H_2SO_4 reactions. In this work four additional reactions are applied and shown in Table 3.2. The gaseous H_2SO_4 formation is modeled from a single (very fast) reaction[36] involving SO_3 and H_2O and high temperature NO_x formation is modeled with the extended Zeldovich mechanism[37]. N_2O is ignored in the present study as it merely relates to lean premixed combustion processes like gas turbines[2] and since premixed combustion is practically absent in large low speed diesel engines.

Reaction No	Reaction	A	β	E/R
R.3.1	$N + NO \leftrightarrow N_2 + O$	2.7E13	0	179
R.3.2	$N + O_2 \leftrightarrow NO + O$	9.0E09	1	3270
R.3.3	$N + OH \leftrightarrow NO + H$	3.36E13	0	194
R.3.4	$SO_3 + H_2O \leftrightarrow H_2SO_4$	7.23E08	0	0

Table 3.2. Applied NO and H_2SO_4 reactions. Arrhenius parameters in cal, cm, mol, s, K for $k = AT^{\beta}exp(-E/RT)$

3.1 Thermodynamics of sulfur oxides in diesel engine operation

In Figure 3.1 the adiabatic flame temperature and the thermodynamic distribution of sulfur compounds for dry air and n-dodecane ($C_{12}H_{26}$) including 3.5 % m/m elemental sulfur is illustrated. The temperatures and mole fractions are presented for excess air ratios (λ) between 0.75 and 1.25.

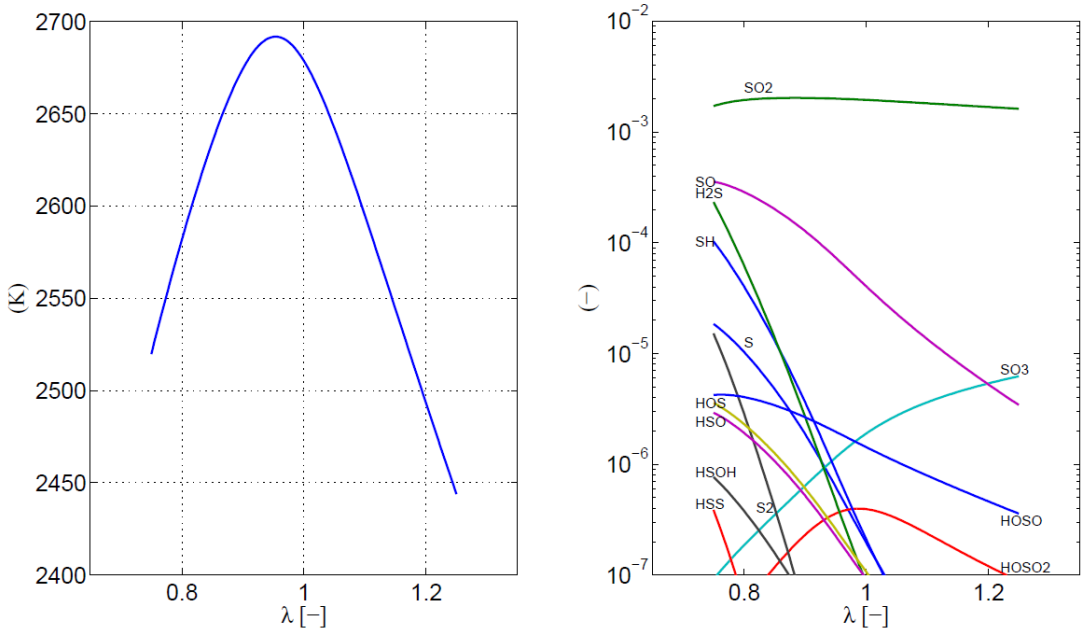

Figure 3.1. The adiabatic flame temperature and mole fractions of sulfur compounds versus the excess air ratio at chemical equilibrium. Reactants are n-dodecane including 3.5 % m/m sulfur in dry air.

At combustion conditions the fuel sulfur is primarily transformed into sulfur oxides with SO_2 being the major sulfur compound even at fuel rich conditions. The overall stoichiometry of a diffusion controlled diesel process is always lean. However diffusion flames burning in air are characterized by a stoichiometric flame front[38] and it is normally assumed that fuel and air reacts (at the flame) at λ=1. As seen in Figure 3.1 the H-S compounds vanish as λ approaches 1 and above. Moreover SO_2 is equilibrated rapidly near the flame front on a time scale comparable to that of the fuel oxidation reactions[22,26,39]. Consequently if rich compositions are neglected and if chemical equilibrium is assumed to exist at flame conditions the H-S compounds can be ignored and the applied sulfur subset can be greatly reduced for a diesel process as examined in a later section.

Gaseous H_2SO_4 is not formed at flame conditions due to thermodynamic restrictions. In fact H_2SO_4 forms at considerably lower temperatures via SO_3 that is neither really preferred at flame conditions (Fig. 3.1). In Figure 3.2 the thermodynamic distribution of important sulfur compounds at 1 bar and 100 bar pressure are shown for the temperature range prevailing during the expansion stroke in a diesel process. The distribution is based on n-dodecane including 3.5 % m/m elemental sulfur and air at λ = 1.25. As shown in the figure the fuel sulfur is distributed in the three species SO_2, SO_3 and H_2SO_4. SO is to some extent present but only at very high temperatures where SO_2 is the primary compound. SO_3 is principally absent at temperatures above 2000 K and H_2SO_4 is confined to temperatures of less than ≈1000 K. At some point during the expansion stroke SO_3 may form at the expense of SO_2 as the gas products cool. According to the thermodynamics the SO_2 will vanish at temperatures of less than 800 K. However, it will be shown later that the governing reactions "freeze" as the cylinder gas cools and only a fraction of the SO_2 is converted. In practice the distribution of SO_x species in the exhaust gas according to Figure 3.2 is not representative. Nevertheless, the fraction of fuel sulfur that is converted to condensable and highly corrosive species is now defined from the ε-expression in eq. 3.1. It is believed that H_2SO_4 forms from a very fast reaction between SO_3 and H_2O. For this reason it makes sense to lump SO_3 and H_2SO_4 and consider both species as highly corrosive.

$$\varepsilon = \frac{[SO_3]+[H_2SO_4]}{[SO_3]+[H_2SO_4]+[SO_2]} \qquad (3.1)$$

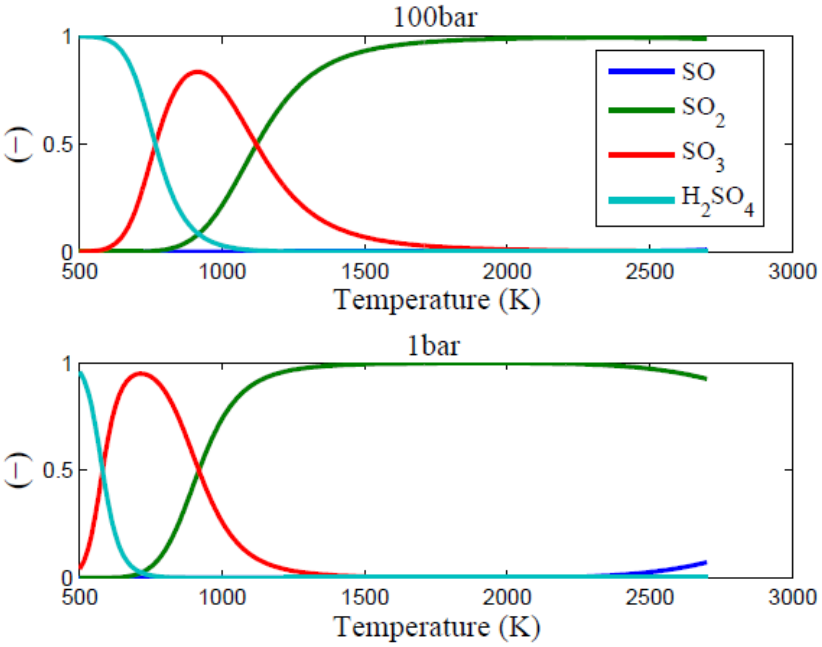

Figure 3.2. Distribution of sulfur compounds versus temperature at chemical equilibrium. Reactants are n-dodecane including 3.5 % m/m sulfur and air at $\lambda = 1.25$.

4. Phenomenological engine model (SO_3 modeling)

An overall description of the engine model is provided in the current section. For a more detailed description the reader is referred to the published material[40] that is enclosed in app A.1. In short the model seeks to reproduce the combustion process of four operating conditions (25%, 50 %, 75 % and 100 % engine load) of the two-stroke engine specified in Table 4.1. Burned fuel products are divided in multiple zones for a more realistic prediction of NO_x and SO_x formation. For each operating case the model applies experimental data such as cylinder pressure history, charge air conditions and valve timings etc.

Number of cylinders	4
Bore/stroke/connecting rod	500mm / 2200 mm / 2885 mm
MCR speed	123 RPM
MCR power	7.050 MW
MEP at MCR	20 bar
Turbocharger	MAN TCA55-VTA

Table 4.1. Reference engine used for the phenomenological engine model.

4.1 General model assumptions

To reduce model complexity a set of general assumptions are introduced:

- The fuel is modeled as n-dodecane ($C_{12}H_{26}$) including non-bonded elemental sulfur.
- The air is modeled as dry air comprising 79 % N_2 and 21 % O_2 only.
- The fraction of injected fuel reflects the fuel burn fraction.
- Injected fuel burns stoichiometrically at the flame temperature.
- Fuel phase changes and particulate matter is not considered.
- Only homogenous gas phase reactions are considered.
- Gas mixtures obey the ideal gas law.
- The model resolution is one crank angle degree.
- The pressure in the cylinder is uniform.
- Blow by affects are neglected.
- Engine cylinder bore, piston position and compression ratio describes the instant cylinder geometry.

- The mixing between fuel products and fresh gas during the expansion stroke is modeled with a simple correlation described in a later section.

4.2 Rate of fuel heat release

A homogenous cylinder gas i.e. a single zone approach is considered in order to evaluate the burned fuel fraction at each crank angle during combustion. For the purpose the first law of thermodynamics of an ideal gas mixture in a closed system is applied (eq. 4.1) where the derivatives are expressed in terms of the crank angle position (θ). A measured cylinder pressure trace $p(\theta)$ and a calculated gas volume $V(\theta)$ is applied to the equation from which the effective net heat release rate $Q_{net}(\theta)$ is approximated.

$$\frac{dQ_{net}}{d\theta} = \frac{\gamma}{\gamma - 1} p \frac{dV}{d\theta} + \frac{1}{\gamma - 1} V \frac{dp}{d\theta} \qquad (4.1)$$

$$\dot{Q}_f = \frac{dQ_f}{d\theta} = \frac{dQ_{net}}{d\theta} + \frac{dQ_{HT}}{d\theta} \qquad (4.2)$$

The liberated heat of the fuel Q_f (eq. 4.2) is the sum of the effective net heat release plus heat transfer/loss Q_{HT} that is approximated from Woschni's heat transfer correlation[41]. In eq. 4.3 $\dot{Q}_f$ is integrated from the point of fuel ignition and throughout the expansion stroke in order to determine the trace of the fuel burn fraction $x_b(\theta)$.

$$x_b(\theta) = \frac{\int_{TOI}^{\theta+\Delta\theta} \dot{Q}_f \cdot d\theta - \int_{TOI}^{\theta} \dot{Q}_f \cdot d\theta}{\int_{TOI} \dot{Q}_f \cdot d\theta} \qquad (4.3)$$

The trapped gas at the time/crank angle where the cylinder gas compression starts is a mixture of fresh gas and hot residual gas products from the previous engine cycle. The share of the residual gas is calculated using Blair's empirical correlation[42] for uniform cylinder scavenging. The unknown temperature of the gas mixture at the start of compression is calculated through an iterative

procedure over a few computational engine cycles. The iteration is stopped once the calculated mixture temperature has converged. In the single-zone approach the gas properties are updated every crank angle and the composition of the cylinder gas is assumed to be in the state of chemical equilibrium if the mean gas temperature is above 1200 K. Otherwise the gas composition remain frozen. The crank angle resolved gas compositions are used to determine the ratio of the specific heats γ needed in eq. 4.1.

Figure 4.1 holds the measured cylinder pressure traces and calculated fuel burn traces of the four model cases. The fuel ignites close to TDC (Crank angles ATDC = 0) but the shape of the burn fraction and the combustion duration varies with the load. The combustion duration (with respect to crank angles) increases with the engine load due to higher engine speeds (as seen in Table 4.2) and since more fuel is added per cycle. According to the fuel burn traces premixed combustion is absent. Premixed combustion is normally depicted as a very high burned fuel gradient close to TDC and is merely linked to the combustion process of smaller engines with higher engine speeds. As a result the multizone model in this work reasonably aims at simulating a fully mixing controlled combustion process.

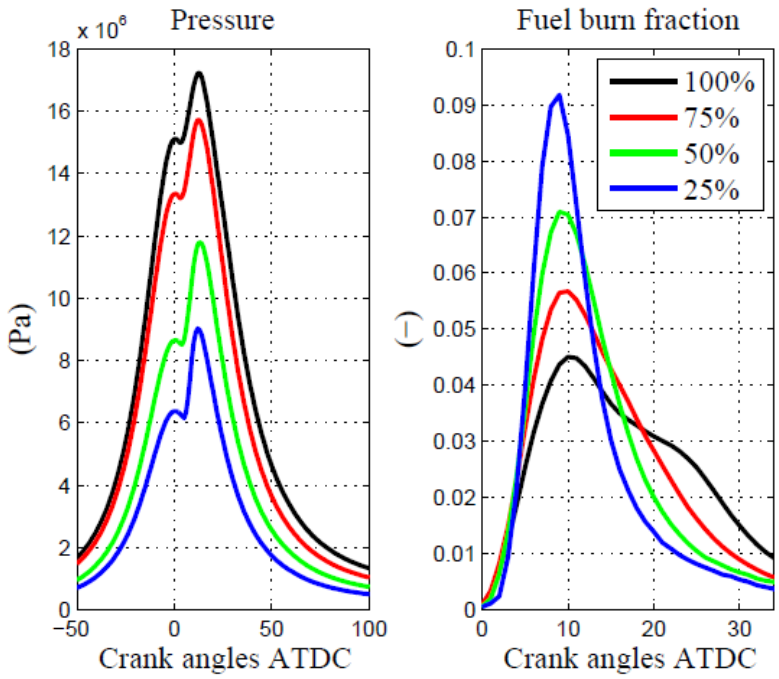

Figure 4.1. Experimental cylinder pressures and modeled fuel burn fractions with respect to crank angle position. The legends refer to the engine load.

4.3 Burned zones and gas mixing

In a compression ignited and mixing controlled diesel combustion process a stoichiometric flame zone encloses the decomposing fuel spray[43]. The complex nature of the spray and flame is not directly modeled in this work. Instead the model seeks to reproduce flame conditions by distributing the injected fuel in multiple burned gas zones with no spatial location (0D model). At each crank angle from the point of fuel ignition and till combustion ends a new burned zone is formed. The burning fuel is initially mixed with fresh gas (air + residual gas) at $\lambda = 1$. The burned zone (flame) temperature is calculated from the assumption that the mixture enthalpy is conserved at chemical equilibrium. This is a common approach[41] due to the high flame temperature of about 2700 K which implies that the chemical reactions between the fuel and the fresh gas proceed very fast. Hereafter a burned zone is diluted with fresh gas every crank angle at a defined rate as described later. No more fuel is added to a burned zone and no gas exchange is considered between burned zones either. Consequently a burned zone grows leaner ($\lambda>1$) throughout the expansion stroke. The process of the burned zones is illustrated in Figure 4.2 from the point of fuel ignition.

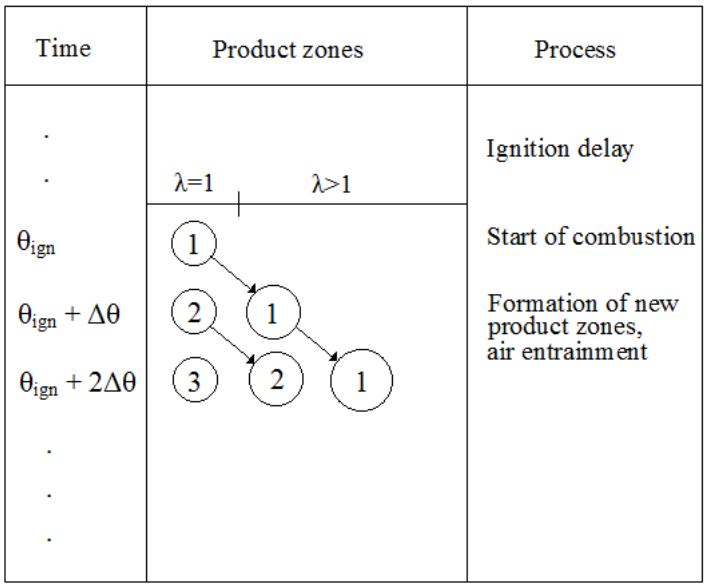

Figure 4.2. The process of the burned zones from the crank angle where fuel ignition takes place θ_{ign}. $\Delta\theta$ represents the model resolution of 1 CAD. The numbers in the figure refer to a burned zone number.

The rate at which fresh gas is mixed into a burned zone is assumed to be constant for every crank angle. Should the local excess air ratio of a burned zone exceed the overall excess air ratio then no more fresh gas is added to the zone. By weighting the overall mass of cylinder charge air according to the fuel burn fraction trace (Figure 4.1) the threshold of fresh air (m_{max}) that can potentially mix

into each burned zone during combustion and expansion until the exhaust valve opens (EVO) is calculated. m_{max} is then used to express the mixing rate as seen in eq. 4.4 where N denotes the number of crank angles between the time of ignition (TOI) and (EVO). In order to investigate the effect of gas mixing the *mixing factor* β is introduced in the equation. Just before TOI the relative fresh gas volume ($\overline{V}$) is one. During combustion and gas mixing the share of fresh gas reduces and the mixing rate of subsequent burned zones is assumed to decrease in line with $\overline{V}$. For a given burned zone $\overline{V}$ represents the relative fresh gas volume exactly at the crank angle where the zone is created. The mixing rate for the burned zones in equation 4.4 now involves m_{max} and $\overline{V}$ that are unique for each burned zone whereas β and N are global parameters. Moreover m_{max}, $\overline{V}$ and N are outputs of the engine model. Hence β acts as the only mixing calibration factor and must be tuned for each simulation case in order reproduce experimental gas data. The mixing rate is a very rough simplification of the complex nature of air entrainment into the flame and combustion products. On the other hand the effect of mixing in terms of gas species formation can be fairly inspected with the suggested correlation.

$$\dot{m}_{mix} = \beta \frac{m_{\max}}{N} \overline{V} \Big|_{bz} \qquad (4.4)$$

Temperature and excess air traces of burned zones

During the expansion stroke the burned zones cool due to gas mixing and expansion. The cooling is assumed to take place in two steps. First the burned zones mix with colder fresh gas at constant pressure. The mixing provides an intermediate temperature T^* that is calculated by conserving the total enthalpy. The gas mixture of a burned zone is assumed to be in the state of general chemical equilibrium if the resulting temperature is more than 1200 K. Otherwise the mixture chemistry is assumed to be frozen. Secondly the ideal gas law on a differential form (eq. 4.5) with respect to θ is applied to calculate the temperature gradient resulting from the expansion. The updated temperature of the burned zone is then determined using Euler integration as shown in eq. 4.6. Temperature and excess air ratio variations throughout the expansion stroke of three selected burned zones (1, 11 and 24) are illustrated in Figure 4.3. The traces correspond to 50 % engine load and will change slightly with the load. Yet for two mixing rates; β = 0.5 and β = 1.0 the figure illustrates the principles of

gas mixing and cooling of the burned zones. By definition; if β = 1 then the first formed burned zone will be mixed with fresh gas to the overall excess air ratio exactly at EVO (110 crank angles ATDC) as seen in the figure. The left most point on each of the traces represents the approximated flame condition where the temperature is around 2700K and the mixture is stoichiometric i.e. λ = 1. If β is increased then more fresh gas is mixed into the burned zones. This results in higher local excess air ratios throughout the expansion stroke but it lowers the local temperatures in turn. The hindered mixing rates of subsequent burned zones (e.g. 11 and 24) by introducing $\bar{V}$ in eq. 4.4 are demonstrated by the ever reducing gradients of the local excess air ratio traces.

$$V\frac{dp}{d\theta}+p\frac{dV}{d\theta}=mR\frac{dT}{d\theta} \qquad (4.5)$$

$$T(\theta+\Delta\theta)\approx T^{*}(\theta)+\frac{dT}{d\theta}\cdot\Delta\theta \qquad (4.6)$$

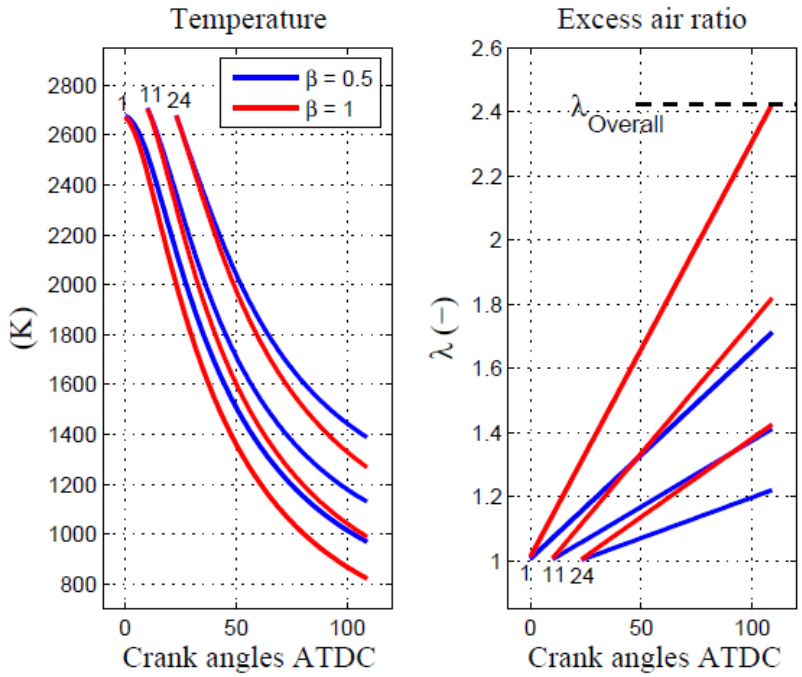

Figure 4.3. Local temperatures and excess air ratios versus gas mixing (β) for three selected burned zones (1, 11 and 24).

Model calibration

In the phenomenological multizone model the chemical reactions take place in the burned zones only. The fresh gas chemistry is essentially frozen throughout the cycle as the temperature is never more than ≈900 °C around max pressure close to TDC. The initial composition of the burned zones is described by chemical equilibrium at the corresponding flame temperature. At every crank angle during the expansion stroke the composition of the burned zones is updated by integrating the chemical reaction rates of the sulfur reaction mechanism through a subroutine in CANTERA. The kinetics is integrated using post process procedure based on the known temperature traces and species balances.

In contrast to the major gas products of fuel combustion such as H_2O and Carbon dioxide (CO_2) NO formation is very sensitive to the temperature and gas mixing history of the burned zones. For the four operating cases listed in Table 4.2 experimental data of NO concentrations in the exhaust gas is provided and the multizone model is calibrated by adjusting the gas mixing rate to all burned zones through β in order to reproduce the measured NO values. This makes NO the key species in terms of model calibration and not SO_3 since no such experimental data were available. The model calibration provides the unknown fresh gas mixing history to the burned zones for the different loads. The procedure is more carefully described in the published material (app. A.1). The resulting β-values are listed in Table 4.2 and show that β is consistently less than one which means that none of the burned zones are mixed fully to the overall excess air ratio. Moreover the magnitude of β is found to reflect the engine speed inversely. This suggests that β is a function of the engine speed which seems rational as lower speeds leaves more time for gas mixing. For the same reason the model predicts higher NO production at reduced speeds in agreement with practical experiences of large low speed marine engines.

4.4 Model Results

According to Figure 3.2 the gaseous H_2SO_4 formation is thermodynamically confined to temperatures of less than ≈1000 K. This is generally less than the minimum temperature of the burned zone traces depicted in Figure 4.3 and H_2SO_4 formation is negligible in the hot gas products throughout the engine cycle. Formation of SO_3 (expressed as ε-traces, eq. 3.1) in selected burned zones at 50 % engine load and 2.0 % m/m fuel sulfur are presented in Figure 4.4. The leftmost point

on each trace represents the approximated stoichiometric flame condition where the very low ε-value indicates that the sulfur compounds are nearly represented by SO_2 only. In the first ≈10 zones SO_3 forms considerably as the gas products cools during the expansion stroke and the fraction of SO_3 can exceed some 4-6 % at EVO. Yet the rapid SO_3 formation is also followed by a quite sudden stagnation. In subsequent zones the oxidation of SO_2 to SO_3 is hampered due to the reducing cylinder pressure (during the gas expansion) resulting in lower partial pressures of reacting species and consequently slower reaction kinetics. In addition the assumption of reduced gas mixing rates for subsequent burned zones as illustrated in Figure 4.3 adds to the suppressing of SO_3 formation through locally lower oxygen concentrations.

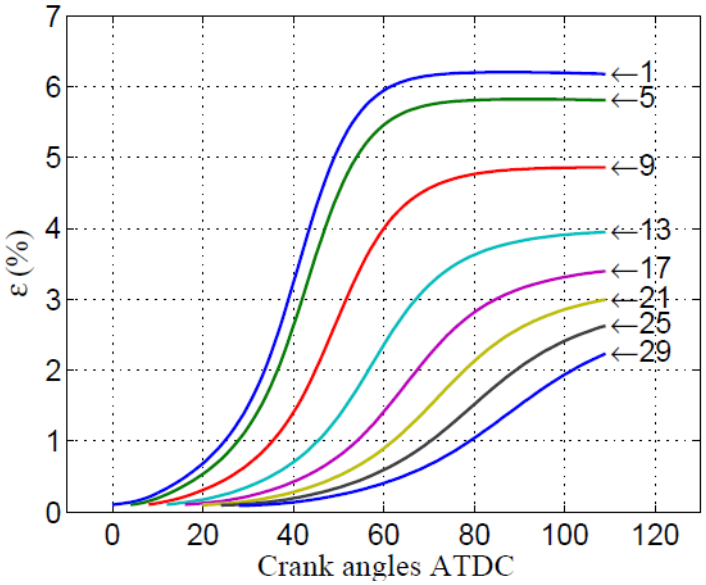

Figure 4.4. Formation of SO_3 in burned zones at 50 % engine load and 2.0 % m/m fuel sulfur. The numbers in the figure refer to selected burned zones.

In Figure 4.5 the ε-traces of the same burned zones as in Figure 4.4 are plotted against the local burned zone temperature instead of crank angle position. The figure also shows the thermodynamic traces of ε that corresponds to chemical equilibrium. According to the figure the SO_3 is rapidly equilibrated at the highest temperatures where the thermodynamic and the kinetic traces are joined. Nevertheless SO_2 is the principal sulfur oxide at conditions close to the flame and SO_3 formation is very limited above 2000 K. The thermodynamic traces indicate that SO_3 is increasingly favored as the temperature decreases. However from about 1650 K the governing SO_3 kinetics is generally too slow to keep up with the thermodynamic growth. It is now concluded that the primary SO_3 formation takes place in the temperature range from 2000 K to 1300 K as seen in the figure and the

governing SO_3 reactions freeze along with the extinction of the free radicals (O and OH) as the burned zones are cooled below 1300 K.

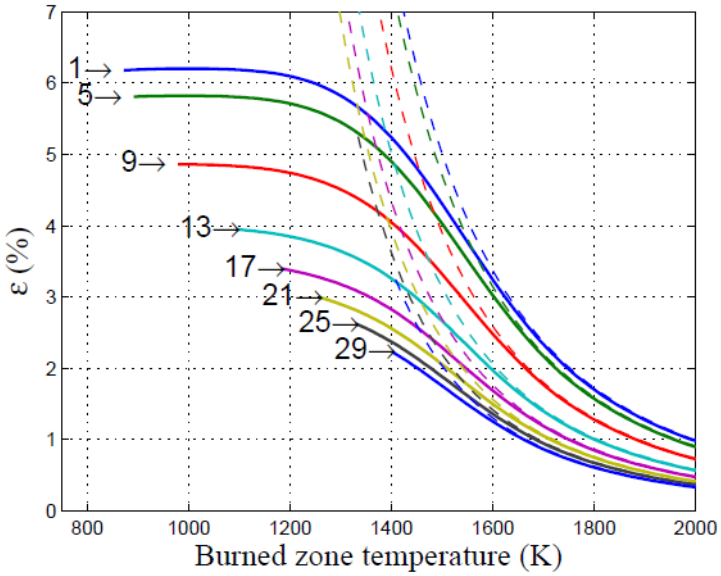

Figure 4.5. Formation of SO_3 in burned zones versus temperature modeled for 50 % engine load and 2.0 % m/m fuel sulfur. The dashed traces represent general chemical equilibrium. The numbers in the figure refer to selected burned zones.

Thru simulations it is realized that elevated cylinder pressures acts to increase the oxidation of SO_2 to SO_3. Yet this trend is not clearly mirrored in Table 4.2 where the maximum cylinder pressure p_{max} of each load case of the reference engine is listed together with the modeled ε-value of the cylinder gas at EVO. The max pressure increases with engine load but the SO_3 formation is also hampered at higher loads due to higher engine speeds. This provides less gas mixing as illustrated by the β-values in the table. The adverse effects of max pressure and engine speed provide that ε is fairly uniform over the full operational range of the large two-stroke marine engine.

Engine load	Speed	NO_{exh}	p_{max}	β	λ_t	ε
%	rpm	ppmv	bar	-	-	-
25	78	1320	90	0.80	2.7	3.7
50	98	1236	118	0.79	2.4	3.9
75	112	1266	157	0.51	2.8	4.1
100	123	1119	172	0.34	2.3	2.7

Table 4.2. Model/reference engine operating data, calibrated β-values and ε-values of the cylinder gas at EVO modeled for 2 % m/m fuel sulfur.

The multizone model is used to investigate how the formation of SO_3 differs with the fuel sulfur content. For the purpose the operating data at 25 % engine load is used and it is assumed that the cylinder pressure trace remains unchanged and does not change with the fuel composition/sulfur content. With the calibrated mixing rate for the particular load case the overall ε-values of the cylinder gas at EVO are calculated and plotted against the sulfur content in Figure 4.6. In the typical sulfur range from 1-4 % m/m the ε-value is quite unaffected. Lower sulfur contents results in higher SO_2 to SO_3 conversion and ε tends to increase asymptotically as the sulfur content approaches zero. This can be explained by the thermodynamics that increasingly favors SO_3 at the expense of SO_2 when the aspect ratio of oxygen to sulfur is increased. This is realized for lower sulfur contents in the current simulations since the gas mixing rate and thus the oxygen content in the burned zones remains unchanged.

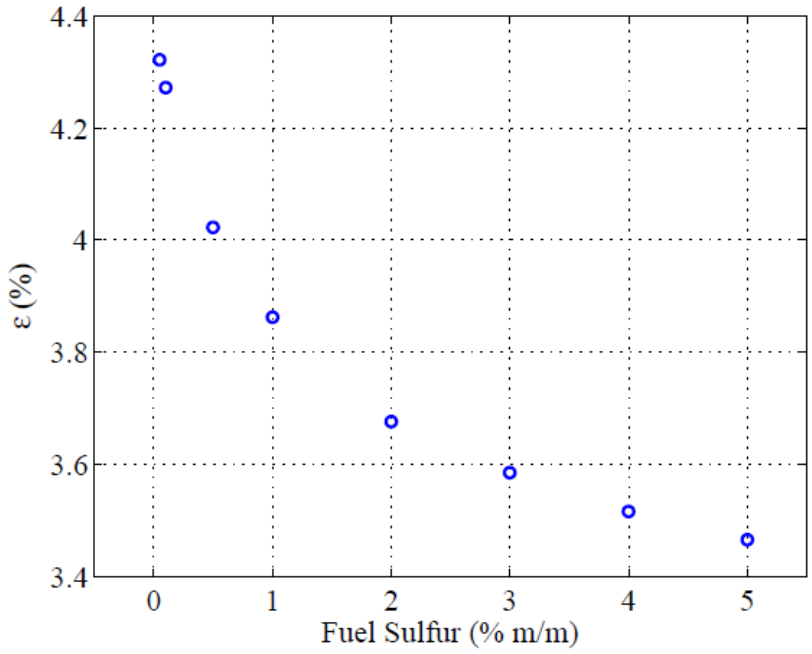

Figure 4.6. The fraction of fuel sulfur that is converted to SO_3 versus the fuel sulfur content modeled at 25 % engine load.

4.5 Reducing the sulfur reaction mechanism

The applied sulfur subset of the sulfur reaction mechanism covers a large number of elementary reactions that may be ignored in the lean post flame conditions prevailing in burned zones in the present model formulation. The sulfur subset can be reduced as long as the distribution of sulfur oxides are not compromised. In order to identify key reactions the multizone model and CANTERA are efficiently combined. Hereby the rate of progress of all elementary reactions can be inspected throughout the engine cycle where the gas composition, pressure and temperatures changes.

Elementary reactions can be eliminated for different reasons. As an example, consider reaction R.4.1 where the molecules A and B react to form two new molecules C and D. R.4.1 can act in both directions and the rate of progress is the net rate between the forward and backward production rates q_f and q_b respectively. Production rates are determined by the rate constants k and the molar concentrations of the acting species as shown in eq. 4.7. The temperature dependent rate constants are calculated by the use of Arrhenius expressions that are partly governed by chemical equilibrium as shown in app. A.4.

$$A + B \leftrightarrow C + D \qquad \text{(R.4.1)}$$

$$q_{net} = q_f - q_b = k_f[A][B] - k_b[C][D] \qquad (4.7)$$

In a reacting chemical system the rate at which A and B are consumed could be balanced by the rate of their production through C and D. In this state the rate of progress of R.4.1 is zero and the reaction does not act in an overall chemistry with multiple reactions. Similarly if the concentration of either C or D is zero and the equilibrium of R.4.1 by far favor A and B then the rate of progress is also zero. In reaction systems like a diesel process the pressure and the temperature is significantly altered during gas expansion and the preferred equilibrium orientation may shift at some point and prefer C and D. This will affect the rate of progress and the particular reaction can no longer be ignored. In this case a negligible effect of R.4.1 would require that the product [A][B] is essentially zero or that the associated activation energy is high enough to act as a reaction barrier. By using a subroutine in CANTERA the rate of progress of all elementary reactions in the sulfur subset is determined for each of the burned zones during the expansion stroke until EVO. With reference to the above considerations any reaction in which the rate of progress throughout the expansion stroke justifies its elimination is considered inactive and is removed from the sulfur subset. For the purpose the H_2/O_2 subset and the CO/CO_2 subset are kept unchanged. For the diesel

process it turns out that the distribution of sulfur oxides in lean post flame conditions can be described by a heavily reduced sulfur subset without compromising the accuracy compared to the full subset. A large part of the explanation lies in the fact that the H-S compounds and H-S-O complexes are thermodynamically not preferred under the lean conditions and are present in such small quantities that they do not contribute to the overall reaction chemistry. The revised sulfur subset comprises the 7 elementary sulfur reactions presented in Table 4.3 wherein the number of sulfur species is now only 4; i.e. SO, SO_2, SO_3 and $HOSO_2$.

Reaction No.	Reaction	A	β	E/R
77	$SO + O_2 \leftrightarrow SO_2 + O$	7.6E3	2.37	2970
86	$SO_2 + O(+M) \leftrightarrow SO_3(+M)$[a]	3.7E11	0.00	1689
	Low-pressure limit	2.4E27	-3.60	5186
	Troe parameters 0.442, 316, 7442			
88	$SO_2 + OH(+M) \leftrightarrow HOSO_2(+M)$[b]	5.7E12	-0.27	0
	Low-pressure limit	1.7E27	-4.09	0
	Troe parameters 0.10, 1E-30, 1E30			
89	$SO_2 + SO_2 \leftrightarrow SO_3 + SO$	5.0E07	2.00	37750
90	$SO_3 + H \leftrightarrow SO_2 + OH$	8.4E09	1.22	2980
93	$SO_3 + OH \leftrightarrow SO_2 + HO_2$	4.8E04	2.46	13700
134	$HOSO_2 + O_2 \leftrightarrow HO_2 + SO_3$	7.8E11	0.00	656

[a]Enhanced third-body coefficients: $N_2 = 0$, $SO_2 = 10$, $H_2O = 10$

[b]Enhanced third-body coefficients: $N_2 = 1$, $SO_2 = 5$, $H_2O = 5$

Table 4.3. Revised sulfur subset for the modeling of SO_3 formation in a large marine diesel engine. Arrhenius parameters in cal, cm, mol, s, K for $k = AT^{\beta}exp(-E/RT)$

A comparison between the full and the revised sulfur subset is presented in Figure 4.7. The comparison is viewed as modeled traces of overall ε-values i.e. the distribution of SO_2 and SO_3 in the cylinder gas products. To challenge the revised subset the effect of modest and excessive gas mixing (β=0.1 and β=1.5 respectively) is investigated. As shown in the figure no difference is observed in the ε-traces for any mixing rate so no accuracy is lost with the revised subset. The current findings are essential as the pathways for SO_3 formation in a large marine engine are clarified. In Figure 4.8 and 4.9 the rate of progress (relative rates) over the expansion stroke of the 7 reactions in the revised sulfur subset are presented for 5 selected burned zones. From the size of the rates it is understood that Reaction 86 and 134 are the primary pathways to SO_3 with the latter being the most dominant. Reaction 134 forms SO_3 via the $HOSO_2$ intermediate produced in

reaction 88. Reaction 89 shifts direction during the process and despite its quite high activation energy shown in Table 4.3 it accounts for about 5 percent of the overall SO_3 formed. Reaction 90 and 93 generally serve to produce SO_3 but their combined contribution is less than 5 percent. Reaction 77 does not act in the production of SO_3 but serves to consume SO that is thermodynamically favored in minor concentrations at very high temperatures.

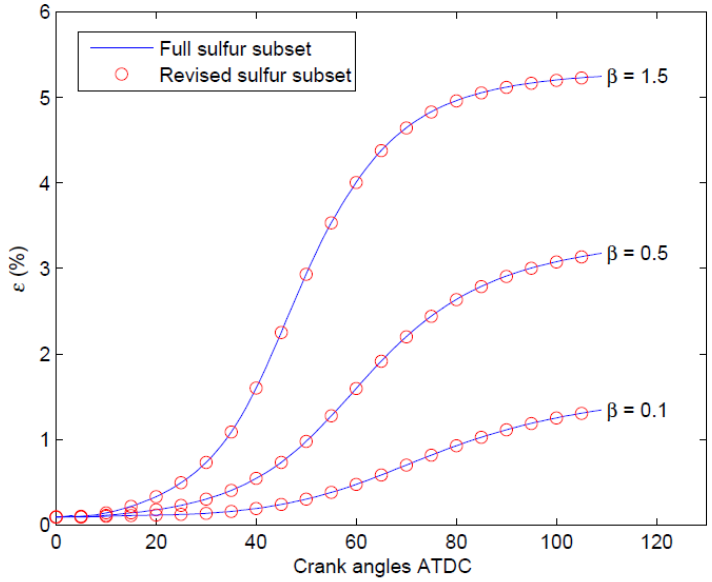

Figure 4.7. Overall SO_3 formation versus crank angle position modeled with the full and the revised sulfur subset at different mixing rates (β), 50% engine load and 4.5 % m/m fuel sulfur.

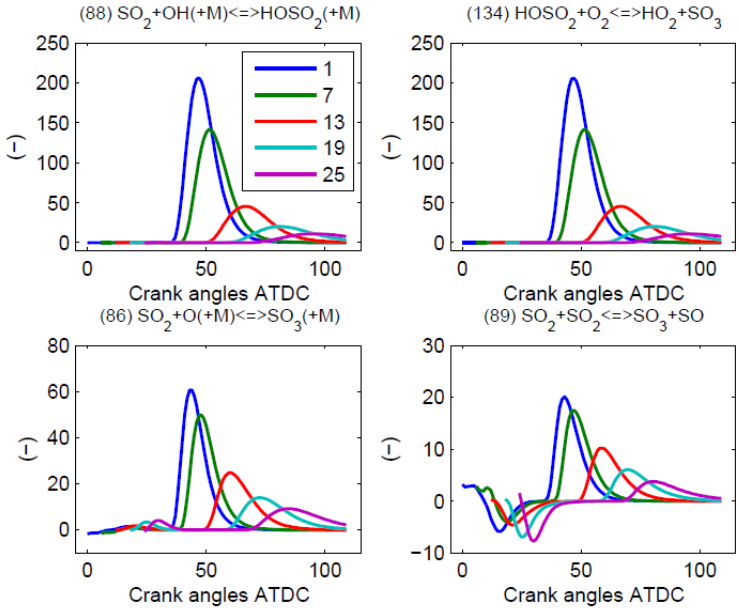

Figure 4.8. Relative rates of progress of reaction number 88, 134, 86 and 89 in Table 4.3. Modeled at 50 % engine load and 4.5 % m/m fuel sulfur.

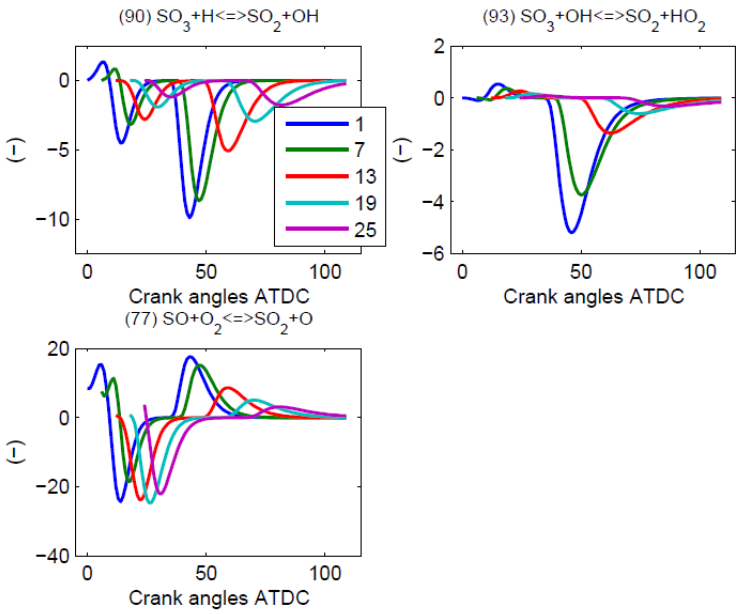

Figure 4.9. Relative rates of progress of reaction number 90, 93 and 77 Table 4.3. Modeled at 50 % engine load and 4.5 % m/m fuel sulfur.

5. Exhaust gas measurements of SO_3

As shown later in this section simulations performed with the multizone model indicate that the fraction of fuel sulfur that is converted to SO_3 (ε) increases in line with the cylinder pressure and reduces with the engine speed. It remains now to be reported if these trends are also reflected in reality. Therefore a series of SO_3 measurements are conducted with a heavy duty single cylinder test engine that operates on HFO including sulfur. In the experiments SO_3 is measured in the exhaust gas under steady operating conditions. In order to alter the SO_3 content the combustion history is varied between experiments by altering the injected fuel mass, fuel injection timing, engine speed and air-fuel ratio.

The response of NO_x is investigated in parallel with SO_3. From a thermodynamic point of view the presence of the two species are not comparable as NO_x is formed primarily at flame conditions (> 2000 K) whereas high temperature SO_3 formation is confined primarily to temperatures less than 2000 K. However both species are sensitive to local gas mixing and rely heavily on species from the radical pool such as OH and O. NO_x formation has been shown to scale with the maximum cylinder pressure in diesel engines[44] and SO_3 is believed to follow a comparable trend. In any case, parallel investigations of NO_x and SO_3 will serve as valuable information and "fingerprints" with respect to model validations. In the published material[45] enclosed in app. A.2 a closer comparison between NO_x and SO_3 measurements are provided but in the present report the results are primarily focusing on SO_3.

5.1 Experimental setup

Test engine specifications are listed in Table 5.1. During the measurements the cylinder pressure trace is recorded with a resolution of 0.25 crank angles over 80 consecutive engine cycles by a piezoelectric pressure transducer located in the combustion chamber. To remove noise the raw pressure data are "smoothened" using the procedure of Harndorf[46]. From the measured cylinder pressures the ROHR-traces are calculated by applying the first law of thermodynamics on a differential form similarly to the procedure previously described in the multizone model. However in the present approach the cylinder gas is considered to be a "real" gas where the internal energy is determined using the technique of Zacharias[47] and wall heat losses follows the procedure of Hohenberg[48,49]. For further details see the published material[45] enclosed in app. A.2.

Number of cylinders	1
Displacement volume	3.18 L
Bore/stroke	150 mm / 180 mm
Compression ratio	15
Rated speed	1500 rpm
Rated Power	80 kW
Fuel injection pressure	Max. 1600 bar
Pressure charging	External (adjustable)
Fuel injection	Single jet

Table 5.1. Specifications of the heavy duty engine used to investigate SO_3 formation.

For practical reasons two HFO's with similar sulfur contents of 1.6 and 2.24 % m/m are used in the experiments. Specific fuel data are listed in Table 5.2. The Calculated Carbon Aromaticity Index (CCAI) is a unit-less number that is frequently used to rank (roughly) the ignition quality of residual fuel oils[50,51]. The number is based on the kinematic viscosity and the fuel density. The lower the number the better are the ignition characteristics. The normal CCAI range is between 800 and 880 and satisfies fuel number 1 only. However ignition performance is also linked to engine design and operating conditions and fuels with higher CCAI's may operate successfully[51] as experienced with the present engine. According to the theoretical conversions of fuel sulfur presented in Figure 4.6 slightly higher SO_3 fractions can in principle be measured with fuel number 1 compared to fuel number 2 due to the lower sulfur content. However the difference of the slight sulfur variations was not measureable.

	C	H	S	H_2O	N+O	Ash	$(A/F)_s^*$	Kin. viscosity at 50 °C	CCAI	LHW
	% m/m						kg_{air}/kg_{fuel}	mm^2/s	-	kJ/kg
Fuel 1	83.47	11.08	1.6	1.68	2.1	0.06	13.4	188	838	38759
Fuel 2	88.5	8.9	2.24	0.01	0.34	0.105	13.3	115	926	40288
*Stoichiometric air fuel ratio										

Table 5.2. Specification of test fuels used to investigate SO_3 formation.

Exhaust gas emissions are sampled in a circular (100 mm) exhaust pipe downstream a gas receiver that works as a gas mixer and damps pressure pulsations produced by the cyclic engine process. A schematic illustration of the experimental facility is shown in Figure 5.1. The engine is operated to produce an exhaust gas temperature that is above the acid dew point temperature all the way to the SO_3 sample location. The dew point can be calculated from an empirical correlation and is a function of the SO_3 and H_2O pressure[52,53]. To avoid acid condensation in the exhaust system a gas/surface temperature of minimum 140-150 °C is required for the present experiments.

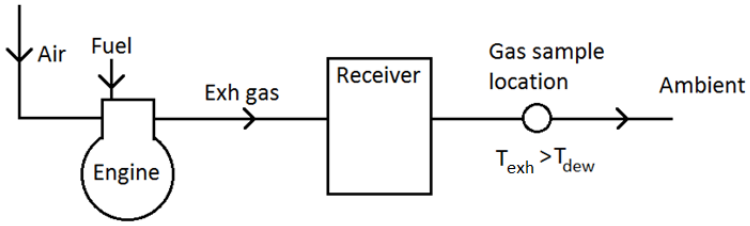

Figure 5.1. Experimental setup used to investigate SO_3 formation.

By compensating for the sulfur bonded to SO_3 and by neglecting any sulfur bonded to particulate mass the SO_2 concentration in the exhaust gas is calculated from the fuel composition and the excess air that is determined from measured exhaust gas compositions. In this respect CO_2/CO and the O_2 concentrations are measured in the exhaust gas with an Infrared Gas Analyzer (IRD) and a Paramagnetic Detector (PMD) respectively. NO_x is measured with a Chemiluminescence Analyzer (CLD). The exhaust gas was analyzed by sampling the exhaust for 4-5 minutes after the thermal response of the exhaust system had stabilized. In contrast SO_3 was sampled for 20-30 minutes in order to assess variations of online SO_3 readings.

5.2 Review of available SO_3 measurement techniques

Complications arise from the highly reactive nature of SO_3 from which SO_3 measurements are challenged and might biased[24,25,54]: 1) SO_3 is a highly reactive gas that reacts with minerals of alkali ash such as magnesium oxide (MgO) and calcium oxide (CaO). 2) SO_3 measurements can be biased due to much higher concentrations of SO_2. 3) SO_3 may react with surfaces e.g. in the sampling line. 4) SO_3 and H_2O form gaseous H_2SO_4 that may condense on “cold” surfaces and on particulate matter. 5) HFO often contain small fractions of vanadium that can be oxidized and catalyze the oxidation of SO_2 to SO_3[55,56].

Current experiences of SO_3 measurements are generally based on gas sampling in the exhaust ducts of coal fired power plants and the gas in those ducts does not fully represent a HFO exhaust gas. As an example the fraction of ash forming matter in typical power plant coals can be as high as 10-30 % by mass[2]. During combustion a fraction of the ash forming matter is thermal decomposed and oxidized into an alkaline ash. Depending on the gas temperature, the alkalinity of the ash as well as the SO_3/H_2SO_4 content significant amounts of SO_3 may be “lost” to the ash[24] which will bias the measurements. However, heavy fuel oils produce much less ash than coal and noncombustible materials such as mineral inclusions are virtually absent[57].

Common methods for measuring SO_3 involves: 1) absorption of SO_3/H_2SO_4 in an isopropanol (IPA) solution, 2) separation of SO_3/H_2SO_4 by controlled condensation and 3) an indirect measurement through the SO_3/H_2SO_4 dew point temperature. A brief description of the methods is provided hereafter. Other methods involving Fourier Transform Infrared Spectroscopy[25] (FTIR), SO_3 capture in salts[54,58], and yet an indirect measurements where the SO_3 content is linked to formation of CO_2 through a plug of calcium oxalate[59] (CaC_2O_4) have shown promising results but are not reviewed in this work. Among the reviewed methods the controlled condensation method (CCD)[60] that is also known as the controlled condensation system (CCS) is the most preferred technique and is recommended by many researchers[58] as well as the U.S Environmental Protection Agency (EPA). However the British and the American standards for CCD have been withdrawn[54]. In this work the PENTOL SO_3 monitor is used. The monitor is a modified version of the instrument formerly known as the Severn Science Analyzer. The principle is described by Jackson[61] and has been used for many years at the Central Electricity Generating Board with apparent succes[62] and in a number of power plants in the USA[25]. The principle is based on SO_3 absorption in an IPA solution where the gas sampling and subsequent SO_3 analysis is automated. Published data on the accuracy does not seem to exist but the manufacturer states that the accuracy of the monitor is ± 5% of reading in the calibrated range. Moreover parallel measurements performed with the SO_3 monitor and the CCD method in a HFO power station resulted in SO_3 concentrations with no significant difference[61].

Acid dew point meter

A stick shaped probe is inserted into the exhaust duct and a sulfuric acid film forms on the probe tip whenever its temperature is below the acid dew point. The highly conductive film enables an electric current between two electrodes that are fabricated into the probe tip together with a thermocouple. The electric current and the probe tip temperature are logged. The tip temperature is regulated by cooling air supplied to the probe tip within the probe. The strength of the electric current is a relative measure of the condensed film thickness. After some adjustment of the cooling air flow rate it is possible to achieve a stable current. A stable current indicates that the rate of acid condensation and evaporation on the probe tip is balanced and the corresponding tip temperature is the measured acid dew point[63] temperature. The dew point measurement relies on the reasonable assumption that the gas phase reaction $H_2O + SO_3 \rightarrow H_2SO_4$ is infinitely fast. Through an

empirical dew point correlation such as the one suggested by Verhoff and Banchero[52] in eq. 5.1 the SO_3 concentration in the sample gas is determined from the measured dew point temperature $T_{a,d}$ and a known H_2O content. The accuracy of the principle is generally good except in gas streams where H_2SO_4 mist is formed as well as in dirty streams where tip deposits may interfere with the readings[62].

$$\frac{1}{T_{a,d}} = 2276E^{-6} - 2943E^{-8}\ln(p_{H2O}) - 858E^{-7}\ln(p_{H2SO4}) + 620E^{-8}\ln(p_{H2SO4})\ln(p_{H2O}) \quad (5.1)$$

EPA Method 8

The EPA method 8 was designed to measure the H_2SO_4 mist from sulfuric acid plants. A steady and known flow of sample gas is continuously sampled for 1-2 hours through a heated glass-lined probe. The gas is then passed through an ice cooled impinger containing a solution of IPA and water. As the gas passes the impinger the H_2SO_4 is absorbed and stored. After the sampling the solution in the impinger is titrated in order to determine the acid strength and thereby the SO_3/H_2SO_4 concentration in the flue gas. Isopropanol is used because of a limited solubility of SO_2 in organic alcohols. Nonetheless it is known that SO_2 from the sample gas may absorb and oxidize in the IPA solution and form acid components. The errors induced can be equal to or greater than the actual concentration of SO_3 in the flue gas[62].

Controlled Condensation Method (CCD)

The better alternative to the EPA Method 8 is the CCD method where a steady and known sample gas flow is continuously sampled for 1-2 hours through a heated glass-lined probe. In the CCD method a heated quartz wool filter placed after the probe is used to capture particulate matter from the sample gas prior to a liquid cooled condenser where the sulfuric acid is fully condensed. The cooling liquid is maintained at ≈80°C which is lower than the sulfuric acid dew point but above the dew point of pure water. Still fractions of water will condense together with the acid according to the H_2O-H_2SO_4 VLE. With the CCD method interference from SO_2 is theoretically excluded and the SO_3/H_2SO_4 concentration in the sample gas is determined through a titration of the condensed acid solution. The CCD method has provided repeatable and accurate measurements in controlled conditions[62].

PENTOL SO_3 Monitor

A steady and known sample gas flow is continuously extracted through a heated (200 °C) glass-lined (quartz) sample probe. Figure 5.2 shows the 1.5 meter probe mounted in the exhaust pipe of the present SO_3 campaign. The probe can be supplied from the manufacturer in different lengths upon request. In the probe head at the probe exit the gas passes a heated quartz wool filter just before it is mixed into an IPA solution. The liquid solution is supplied from an external vessel via the umbilical shown in the figure. The IPA solution absorbs the SO_3/H_2SO_4 compounds from the sample as sulfate ions (SO_4^{2-}). Via the umbilical the solution is then passed through a reaction bed of barium chloranilate crystals where the SO_4^{2-} ions reacts to form acid chloranilate ions as seen in R.5.1

$$SO_4^{2-} + BaC_6O_4Cl_2 + H^+ \rightarrow BaSO_4 + HC_6O_4Cl_2^- \quad \text{(R.5.1)}$$

The acid ions absorb light preferably at 535 nm and are detected in the solution with a photometer. By maintaining a constant flow of IPA solution and sample gas the SO_3/H_2SO_4 concentration in the sample gas is proportional to the absorbed light. Prior to use the monitor is calibrated with calibration liquids equivalent to 5 ppmv and 45 ppmv of SO_3 in sample gas. Chemical conversions and analysis take place in the reaction module shown in Figure 5.2 and via the CPU the photometer signals are transformed to online data readings of SO_3 concentrations.

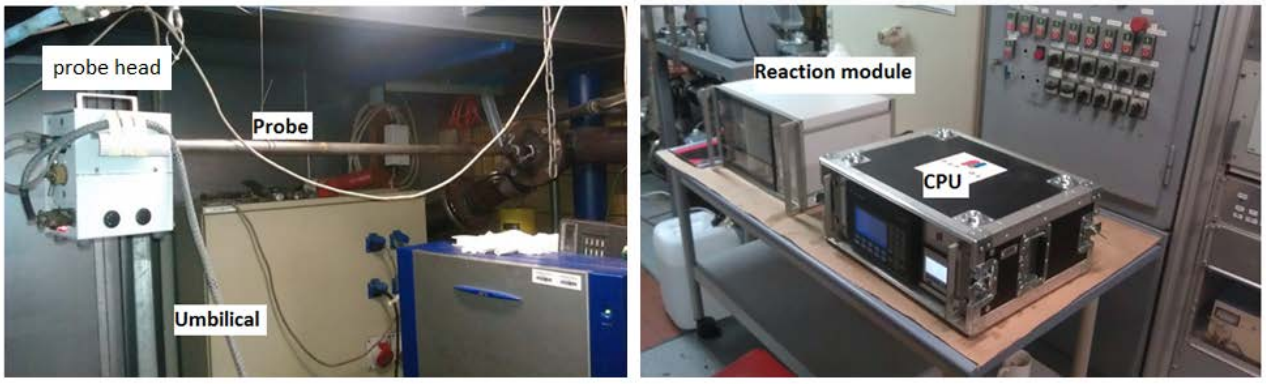

Figure 5.2. Left: Installation of PENTOL SO_3 probe in exhaust system. Right: PENTOL SO_3 monitor

5.3 Experimental results

The effect of cylinder pressure on SO_3 formation is investigated in test series 1 (exp. 1.1-1.4) in Table 5.3. A comparable amount of fuel is burned equally lean but produces different pressure histories (p_{max}) due to altered injection timings (SOI) as seen in the table. The engine speed and power output is the same but SOI is retarded from 25 CA BTDC to 14.25 CA BTDC over the test series. The different timings slightly alter the engine thermal efficiency between the experiments and slight variations of fuel consumption and charge air pressures occur. Yet the fuel consumption did not differ more than ± 7 % of the mean value.

Exp.	rpm	IMEP	p_{max}	p_a	λ	λ_t	T_a	$\dot{m}_a$	SOI	Δt_{inj}	p_{inj}	S	SO_3	SO_2	ε	NO_x	*T_{exh}	Δt_e
	1/min	bar	bar	bar	-	-	K	kg/h	CA BTDC	µs	bar	% m/m	ppmv	ppmv	%	ppmv	K	s
1.1	1500	7.9	90	1.7	2.1	2.1	348	192	25	1480	920	2.2	8.3	685	1.20	1101	712	6.3
1.2	1500	8.0	84	1.7	2.0	2.0	349	191	21	1590	920	2.2	5.8	720	0.80	714	743	6.2
1.3	1500	8.3	83	1.9	2.1	2.1	350	209	17.5	1615	920	2.2	4.4	691	0.63	426	762	5.6
1.4	1500	7.9	81	1.9	2.1	2.1	351	218	14.25	1630	920	2.2	3.8	694	0.54	370	780	5.3
2.1	1200	6.3	89	1.4	3.3	2.8	346	179	21	1230	1020	2.2	10.7	441	2.37	1536	540	8.0
2.2	1200	6.1	83	1.3	2.5	2.5	346	142	21	1050	1020	2.2	13.1	576	2.22	1885	602	9.4
2.3	1200	5.9	75	1.2	2.0	2.0	348	107	21	1280	1020	2.2	14.2	719	1.94	1631	684	11.5
3.1	1500	17.3	124	2.4	2.3	1.6	345	485	23.5	3900	1020	1.6	7.2	443	1.60	648	783	2.3
3.2	1500	17.9	119	2.5	2.3	1.6	343	509	19.25	4220	1020	1.6	6.6	445	1.46	502	806	2.2
3.3	1500	17.7	113	2.6	2.4	1.7	345	530	15.25	4130	1020	1.6	6.2	424	1.44	453	799	2.2
4.1	1500	17.8	120	2.4	2.3	1.7	335	484	19.25	3470	1250	1.6	7.5	441	1.67	730	767	2.4
4.2	1500	12.8	93	2.1	2.5	1.8	346	409	15	3490	920	1.6	4.8	419	1.13	287	802	2.8
4.3	1500	12.8	90	2.0	2.3	1.7	346	395	15	2976	1120	1.6	4.9	445	1.09	340	804	2.9
4.4	1500	14.9	104	2.2	2.4	1.7	345	432	19	3470	1020	1.6	5.0	439	1.13	442	804	2.6
4.5	1500	14.7	100	2.2	2.3	1.7	346	433	18	3578	1020	1.6	4.6	460	0.99	410	815	2.6
4.6	1200	18.2	130	2.3	2.3	1.6	345	379	19	3414	1110	1.6	8.9	452	1.93	1296	702	3.2
4.7	1500	7.9	70	1.6	1.5	1.5	363	154	17.5	1600	920	2.2	4.6	952	0.48	563	863	6.9
5.1	1200	15.9	115	2.1	2.4	1.7	327	352	18.5	3250	1020	1.6	6.9	426	1.59	883	705	3.5
5.2	1200	15.9	105	1.9	2.0	1.5	328	307	18.5	3448	1020	1.6	7.2	516	1.38	1036	764	3.8
5.3	1200	15.8	124	2.4	3.1	2.1	337	416	18.5	3195	1020	1.6	6.3	336	1.84	792	619	3.2
6.1	1400	14.1	98	2.0	2.3	1.7	347	372	18.5	3098	1020	1.6	5.1	452	1.12	556	773	3.1
6.2	1300	13.8	97	1.9	2.2	1.6	347	335	18.5	3058	1020	1.6	5.6	464	1.19	672	759	3.5
6.3	1200	13.7	103	1.8	2.3	1.6	346	311	18.5	2980	1020	1.6	6.3	440	1.41	813	710	3.9
6.4	1100	14.1	105	1.7	2.2	1.6	337	274	18.5	3070	1020	1.6	8.5	463	1.80	1113	694	4.5
6.5	1050	14.4	111	1.8	2.3	1.6	327	272	18.25	3064	1020	1.6	9.3	444	2.05	1254	679	4.6

*Exhaust temperature at the engine exhaust valve

Table 5.3. Complete test matrix of the SO_3 campaign. The left most column represents test series and experiment numbers.

Figure 5.3 illustrates the measured SO_3 profile (ppmv) of the PENTOL monitor of test series 1. Transition from one experiment to another involves a fall in the trace until a new steady condition is

reached. The transition is a combination of engine tuning and response time of the SO_3 monitor. The new steady condition represents the subsequent measurement as indicated by the SOI-numbers in the figure. During each measurement a practically constant concentration is identified with the monitor and it is found that the concentration/formation of SO_3 decreases when the SOI is retarded. Moreover even small SO_3 concentrations of less than 10 ppmv are consistently detected by the monitor.

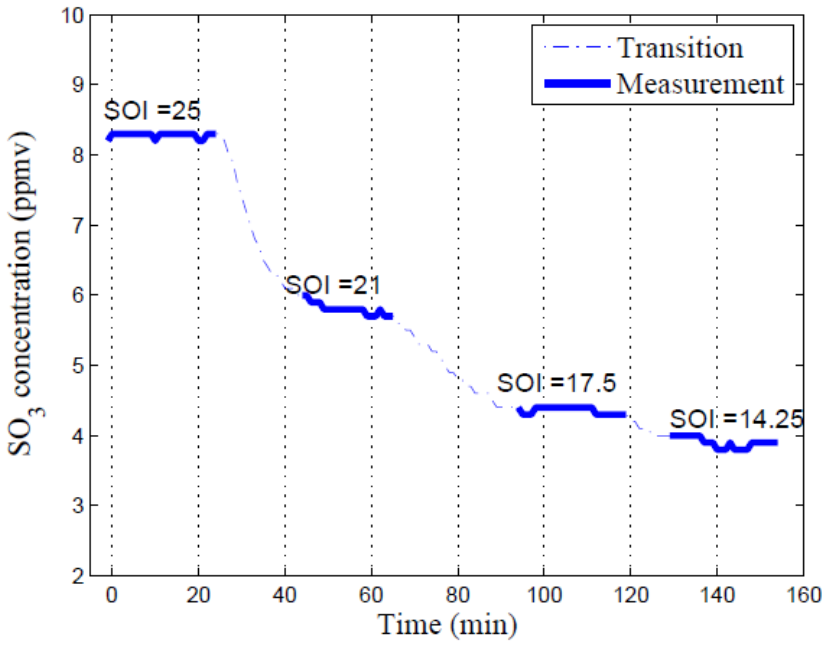

Figure 5.3. Measured SO_3 profile of test series 1. The numbers in the figure refer to the different injection timings in CA BTDC.

The gas temperature at the engine exhaust valve is quite similar in test series 1. It can be shown that the gas residence time Δt_{res} from the engine exhaust valve to the SO_3 sample point is between 5.3 and 6.3 seconds as shown in Table 5.3. The heated probe (200 °C) provides a residence time of ≈2 seconds. At both temperatures SO_3/H_2SO_4 is thermodynamically preferred over SO_2 as seen in Figure 3.2. However SO_3 simulations presented in an earlier section indicate that the governing SO_3 reactions will freeze in the engine cylinder during the expansion stroke. Yet a direct oxidation of SO_2 with molecular oxygen O_2 could potentially form SO_3 in the exhaust system where the gas residence time on a chemical time scale is quite high. On the other hand the reaction is known to be very slow in the absence of appropriate catalysts. A catalytic oxidation of SO_2 to SO_3 may occur in the exhaust system due to the presence of metal oxides; iron oxide, chrome oxide and vanadium oxide among others that originate from the fuel. The metal oxides serve as oxygen-carriers that can catalyze the oxidation of SO_2. Nonetheless the measured SO_3 fraction (ε) in test series 1 is

generally low as seen in Table 5.3. Especially in experiment 1.4 where ε is 0.54. Moreover the exhaust gas conditions are similar with respect to temperature, residence time, SO_2 concentration and excess air ratio in test series 1. With this in mind the measured ε-differences of the test series is most likely caused by the altered operating conditions and the contribution of gaseous or catalytic SO_3 formation in the exhaust system seems very limited.

The ROHR (rate of heat release) traces in Figure 5.4 illustrate the combustion histories of test series 1. It is observed that earlier injections advance the point of ignition relative to TDC. In addition early injections promote the share of premixed combustion that is represented by the area below the ROHR peak close to TDC. With early injections more fuel burns around TDC where the cylinder volume is small and the max pressure is altered from 81 bar to 90 bar in test series 1. As seen in the figure the operating pressure appears to have a similar effect on the measured SO_3 and NOx concentrations in the exhaust gas. This makes sense as elevated pressures provide higher molar densities/partial pressures of governing reactants resulting in faster chemical kinetics. The influence of pressure on SO_3 formation is best illustrated by ε and shown in the figure. The ε-values increase in line with the maximum cylinder pressure meaning that a higher fraction of the fuel sulfur is converted to SO_3 when the operating pressure is increased. Still it is not clear whether the altered pressure histories are solely responsible for that. An argument for this is that the share of premixed combustion is not comparable in test series 1 as indicated in the figure. The share premixed combustion accounts for 34 % of the fuel energy in experiment 1.1 but only 17 % in experiment 1.4.

In test series 2 in Table 5.3 the influence of premixed combustion on SO_3 formation is investigated. In the three experiments premixed combustion is promoted by reducing the engine speed (compared to test series 1) combined with early fuel injections at 21 CA BTDC. Furthermore the cylinder pressure history is altered between the experiments via different charge air pressures p_a that alters the trapped excess air ratio λ_t. Later in this section it is shown that changing the excess air ratio does not seem to effect SO_3 formation. The ROHR traces of test series 2 are presented in Figure 5.5 together with the trace of experiment 1.3 for comparison. The share of premixed combustion is comparably high and heterogeneous mixing controlled combustion is nearly absent in series 2. But in agreement with test series 1 the fraction of SO_3 (ε) in the exhaust gas increases in line with the max pressure as seen in the figure. Yet despite the similar max pressure range of the two series the ε-values are significantly higher in test series 2. The effect of engine speed on SO_3 formation is investigated later in the section and demonstrates that the reduced engine speed in series 2 cannot explain the large ε-differences compared to test series 1. It is concluded that SO_3 formation is

promoted with the share of premixed combustion and the results of ε in test series 1 are influenced by the inconsistent premixed proportions. The measured concentrations of SO_3 versus max pressure of test series 2 in Figure 5.5 are not readily comparable due to the different excess air ratios shown in Table 5.3. The same applies to the NOx measurements. But despite the more lean air fuel mixtures in test series 2 both SO_3 and NOx are present in remarkably higher concentrations compared to test series 1. This is likely explained by the superior fractions of premixed combustion that acts to increase their rate of formation. Premixed combustion refers to injected fuel that evaporates and mixes partly with air prior to the point of fuel ignition. At ignition the premixed portion burns rapidly but incompletely. As a result intermediate gas products like CO are formed in the combustion chamber before the more complete oxidation. CO flames produce high concentrations of oxygen atoms[64] that combined with SO_2 is a significant source of SO_3 formation[11]. This may explain the superior SO_3 fractions experienced in test series 2. Moreover 1D staged combustion reactor experiments i.e. rich combustion prior to secondary air entrainment for completing combustion have shown to increase SO_3 formation[19,20] compared to single stage combustion at the same air-fuel ratios. CO flames doped with sulfur species have also shown to produce increased amounts of SO_3 compared to sulfur doped methane flames[21] that involve smaller concentrations of atomic O.

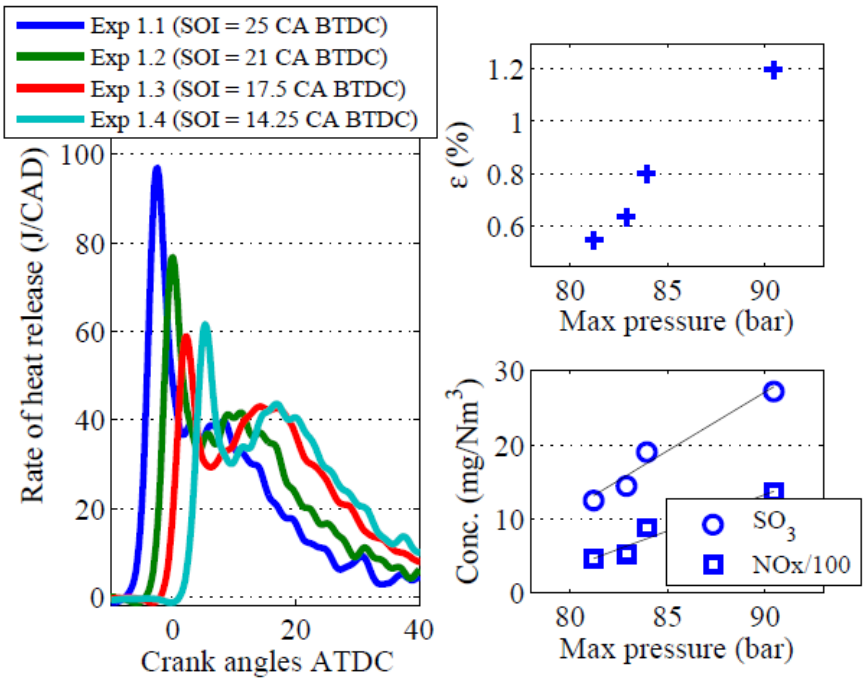

Figure 5.4. Test series 1. Left: ROHR traces. Upper right: Fraction of fuel sulfur converted to SO_3 versus max cylinder pressure. Lower right: Specific emissions of SO_3 and NO_x versus max cylinder pressure. The max pressure increases with earlier fuel injections relative to TDC.

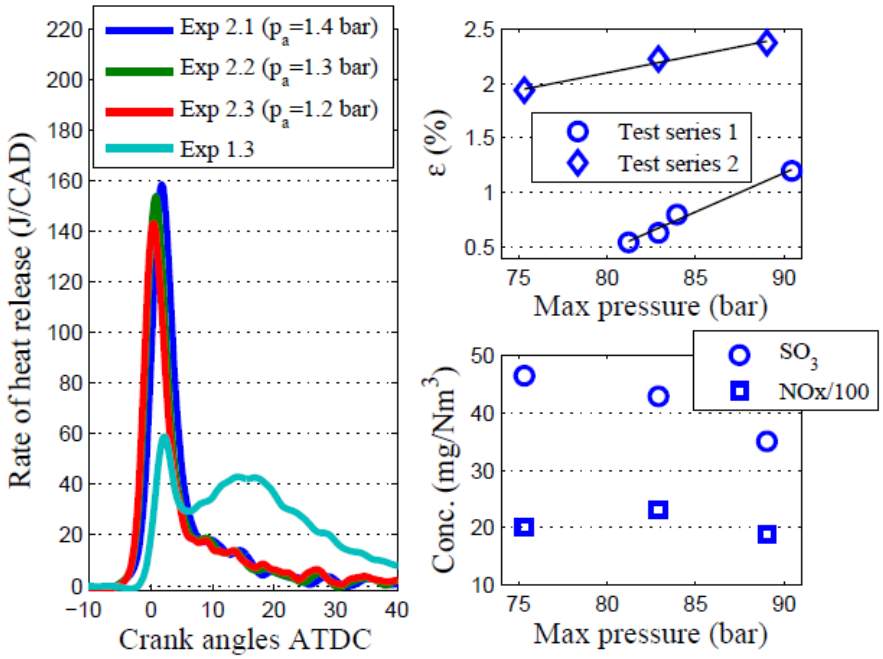

Figure 5.5. Test series 2. Left: ROHR traces. Upper right: Fraction of fuel sulfur converted to SO_3 versus max cylinder pressure. Lower right: Specific emissions of SO_3 and NO_x versus max cylinder pressure. The max pressure increases with elevated charge air pressure p_a.

The correlation between maximum cylinder pressure and SO_3 formation is examined over a widespread pressure range in four additional test series. Herein the SO_3 formation is triggered by operating the engine at different engine loads, excess air ratios and speeds. Unlike large marine engines it is not possible to avoid premixed combustion completely with the heavy duty test engine. To minimize the influence of premixed combustion in the additional test series (3-6 in Table 5.3) the share is less than 20 % and is found to be an acceptable compromise. Test series 3 involves retarded injection timings similar to test series 1 but is conducted at higher engine loads as seen by the effective mean pressures $imep$ in Table 5.3. Higher loads means that more fuel is injected into the cylinder which lowers the share of premixed combustion to a level where the combustion process is nearly fully mixing controlled. In test series 4 the trapped air-fuel ratio λ_t is kept comparably constant but the fuel input is altered as indicated by the air flow rate $\dot{m}_a$ to increase the power and thereby maximum cylinder pressure p_{max} as seen in the table. In Test series 5 the influence of trapped air-fuel ratio λ_t is investigated by altering the charge air pressure p_a relative to the injected fuel mass whereby the resulting pressure history differs as seen by p_{max} in the table. In test series 6 the influence of engine speed rpm is investigated. Basically a fixed fuel mass is burned in a fixed amount of air but the pressure history is altered through the different engine speeds as

indicated by p_{max} in the table. A more detailed description of the experiments can be found in the published material[45] enclosed in app. A.2. Figure 5.6 presents the measured ε-values with respect to maximum cylinder pressure of the 6 different test series. Test series 4 cover the entire max pressure range from 70 bar to 130 bar wherein the ε-values are shown to increase proportionally from 0.5 % to 1.9 %. In fact the resulting ε-values are well represented by a linear fit.

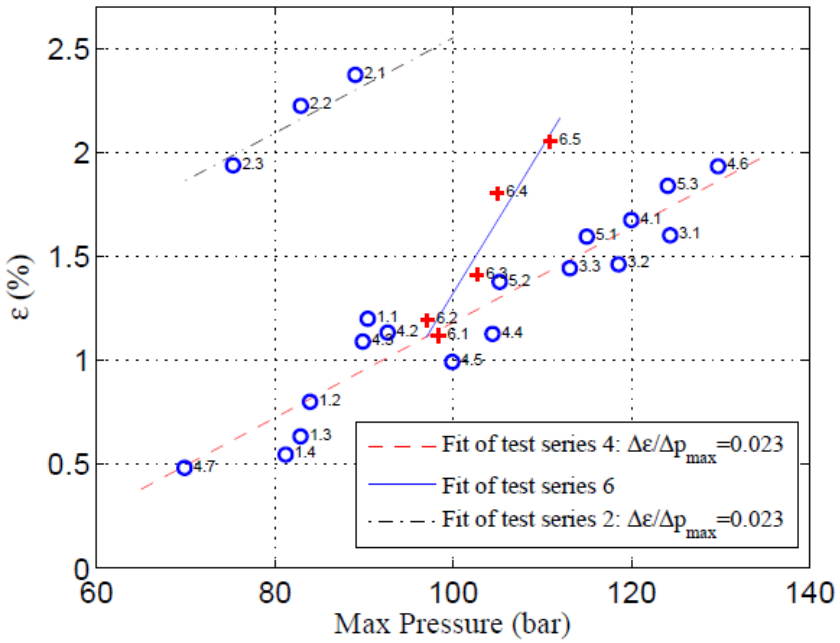

Figure 5.6. Correlation between maximum cylinder pressure and fuel sulfur converted to SO_3. The numbers in the figure refer to the experiments in Table 5.3.

The max pressure range of test series 3 is moderate. Yet there is no clear indication that the altered injection timings influences SO_3 formation apart from the accompanied pressure changes and the ε-values tend to follow the general trend of test series 4 as seen in Figure 5.6. Neither does the trapped air fuel ratio seem to affect SO_3 formation. This is illustrated by the results of test series 5 in the figure where the response of ε does not deviate from the general trend of test series 4. This suggests that ε in series 5 is elevated by the increased pressure histories rather than the excess air ratio. The statement is supported by the results of test series 2 where the charge air pressure is altered likewise to alter the air fuel ratio. As seen in Figure 5.6 the resulting ε-values of series 2 follow a linear fit with the same gradient as the linear fit of test series 4. This leads to a general conclusion that elevated operating pressures yield higher molar densities/partial pressures of gas species that improve the governing reaction kinetics in terms of SO_2 to SO_3 conversion.

The linear fit through the dataset of test series 6 in Figure 5.6 deviates from the general trend as demonstrated by a steeper slope compared to series 4. In test series 6 the ε-value decreases with the engine speed. In other words a reduction of the engine speed promotes SO_3 formation but the ε-values in the series are possibly affected in more than one way. When the speed is reduced the operating pressure increases. But more important more time is available for chemical reactions and gas mixing i.e. air entrainment into the hot gas products in the cylinder.

5.4 Multi zone model vs. experimental results

In order to validate the phenomenological multizone approach (combined with the sulfur reaction mechanism) it is desired to adapt the engine model to the heavy duty test engine and seek to reproduce the experimental data presented in this section. Currently this task has not been undertaken. Instead a rough validation is performed by reproducing experimental trends only. If it is assumed that the net heat release trace $Q_{net}(\theta)$ of a simulation case (Table 4.2) is independent of the engine speed then the resulting cylinder pressure trace $p(\theta)$ is also independent of the engine speed. This is not rational in practice as the rate of combustion cannot be directly controlled. Anyway in the multizone model the rate of fresh gas mixing into the hot combustion products/burned zones is determined by $\dot{m}_{mix}$ in eq. 4.4. The mix gain factor β likely decreases with the engine speed since less time is available for gas mixing. As a result β is considered as a relative measure of engine speed. In Figure 5.7 the effect of β on SO_3 formation is illustrated for the 50 % load case. Elevated gas mixing promotes SO_3 formation as seen from ε in the figure. Stating that β scales linearly with the engine speed is a postulate. Nevertheless this assumption is now used to correlate SO_3 formation to the engine speed. The calibrated β-value at 50 % engine load is 0.79 and the engine speed is 98 rpm. With the linear approximation β should be 0.079 at 980 rpm etc. The engine speed results in Figure 5.7 now suggest that ε is proportional to $\left(\frac{1}{\sqrt{rpm}}\right)$ which means that ε-gradients are highest at lower engine speeds. At 1500 rpm the resulting ε-value is close to 1 %. This number fits reasonably with the experimental results of Tests series 4 (at similar max pressures) in Table 5.3. In addition the suggested curvature of the engine speed results explains the differences between modeled and measured ε values of the large marine engine and the heavy duty engine (Table 4.2 and Table 5.3 respectively).

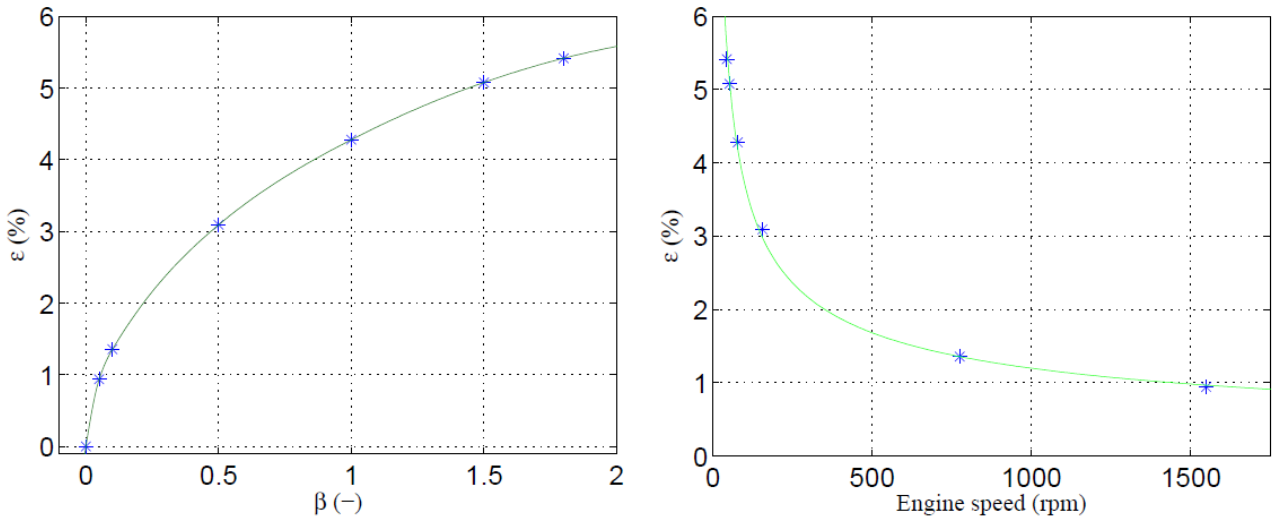

Figure 5.7. Left: Fraction of fuel sulfur converted to SO_3 versus gas mixing (β). Right: Fraction of fuel sulfur converted to SO_3 versus engine speed. Model conditions correspond to 50 % engine load and 2.0 % m/m fuel sulfur.

It is shown in Figure 5.6 that ε increases linearly with the maximum cylinder pressure. A reasonable way to alter the cylinder pressure in simulations is by slightly shifting the $Q_{net}(\theta)$ trace relative to the base trace determined from the thermodynamic analysis in Figure 4.1. It is also fair to assume that the rate of fresh gas mixing into the burned zones remains unchanged when $Q_{net}(\theta)$ is only shifted a few crank angle degrees. To vary the cylinder pressure history $Q_{net}(\theta)$ at 25 %, 50 % and 75 % engine load is shifted ±2 CAD relative to the base trace. For each load three different max pressures and ε-values are then simulated as shown in Figure 5.8.

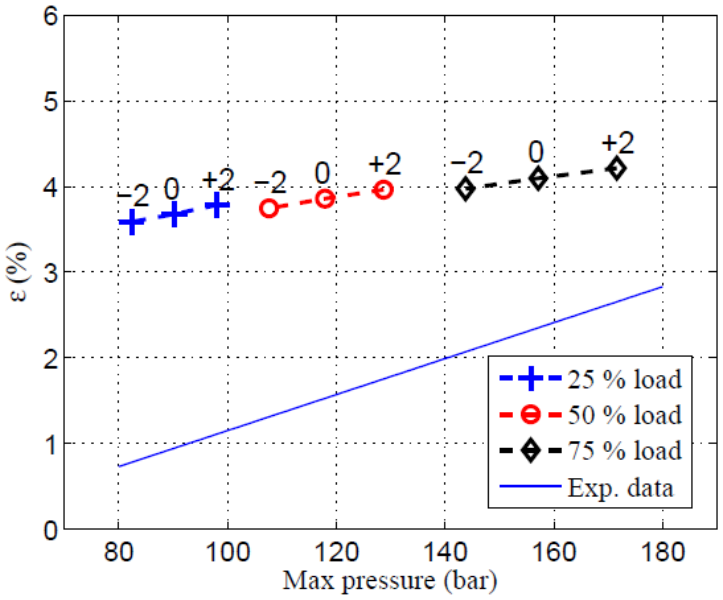

Figure 5.8. Modeled and measured ε-values with respect to max cylinder pressure (fuel sulfur content 1.6 wt. %). The numbers in the figure refer to the shift of the $Q_{net}(\theta)$ trace (in crank angles degrees) relative to a base case.

The resulting ε-values of the model now follow a linear trend similar to the experimental data. However the experimental ε-slope (from Figure 5.6) is slightly higher than the model predictions. It is unclear what causes the slight difference. The very simple mixing approach may be one reason. Another reason could be the accuracy of the experimental data. In order to examine the observed ε-differences the first task would be to adapt the multizone model to the experimental data of the heavy duty engine. This could give an indication whether the applied mixing correlation should be modified. However it is important to keep in mind that accurate SO_3 measurements are challenging as explained earlier.

6. Modeling the characteristics of sulfuric acid condensation on the cylinder liner

Gaseous sulfuric acid and water vapor from the bulk/cylinder gas may condense on the cylinder liner (Figure 1.2) if the surface temperature is lower than the sulfuric acid dew point temperature. In this situation the condensing rates of acid and water are comparable. However if the liner temperature is also lower than the dew point of pure water vapor then the rate of water greatly exceeds the acid that is highly diluted. Condensation can be considered as molecular gas diffusion of condensable species through a very thin gaseous boundary layer. The species are forced to the gas-liquid interphase due to partial pressure gradients[63,65,66]. Conversion from gas to liquid is not rate limiting[66]. I.e. vapor liquid equilibrium (VLE) is assumed to exist at the interphase. The process of condensation is sketched in Figure 6.1. Gaseous sulfuric acid does not really form in the hot bulk cylinder gas due to thermodynamic restrictions. However from the kinetics of R.3.4 (Table 3.2) the SO_3 in the bulk gas is assumed to react instantly with water vapor very close to the cooled liner surface to form gaseous H_2SO_4, and throughout this section SO_3 in the bulk gas is lumped with H_2SO_4.

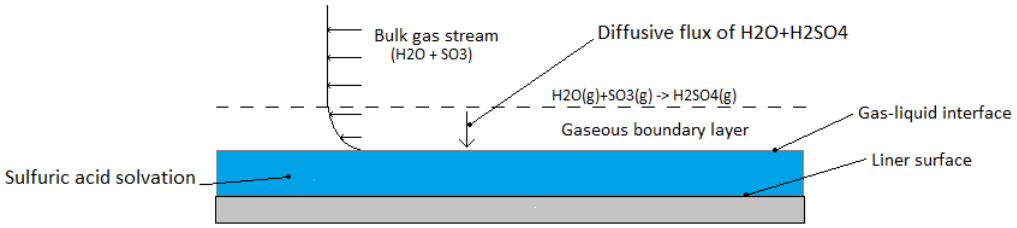

Figure 6.1. The principles of H_2SO_4 and H_2O diffusion through the gaseous boundary layer and subsequent condensation on the cylinder liner.

In reality a thin lube oil film is distributed on the liner surface that acts to prevent acid corrosion by means of base additives that are blended in the lube oil. In combination with the lube oil dosing strategy the base additives basically provide the means to hamper corrosion. Nevertheless high lubricant feed rates are sometimes required to avoid corrosion which is impractical as well as expensive. Moreover the dosing strategy and the state of the protective oil film is influenced by several parameters such as the operating conditions, fuel quality, sulfur content, operating environment, lube oil formulation, liner temperature and mechanical interactions from the moving piston etc. In addition the distribution and refreshment of lube oil on the whole liner area is not

ideal. Measurements indicate that the oil film thickness is generally in the order of micro meters. However thermal degradation of the oil provides that the film thickness is several times less on the liner surface that corresponds to the piston position at TDC[6]. This is also the location where corrosion is mostly pronounced in practice. It would require a very complex model in order to consider all the operating effects that influence the state of the oil film. Since corrosion is believed to be closely linked to the amount of deposed sulfuric acid on the cylinder liner the intention with this work is to model the characteristics of sulfuric acid condensation on the liner. It is believed that valuable information in terms of liner corrosion can be retrieved from the condensation analysis. To simplify things further the condensation is assumed to take place on a surface with no oil film and the surface temperature is assumed constant throughout the stroke. The bulk gas is treated as a homogenous gas mixture i.e. the gas species in the burned zones and the fresh gas is fully mixed at each instant cylinder gas volume.

The sulfuric acid dew point may be determined from empirical formulas[52,53] that correlate the dew point temperature to the bulk gas pressure of SO_3/H_2SO_4 and H_2O. However these correlations do not provide information about the share of condensing sulfuric acid and water. A more convenient approach for the present study is to apply VLE of the H_2O-H_2SO_4 system. Theoretical correlations of this type are based on thermodynamic properties of the components in the gas and the liquid phase. Abel[67] was among the first to derive the vapor-phase above a liquid solution of sulfuric acid and water. He used the best available thermodynamic data at that time. The theoretical models have been improved over the years as the data has been gradually upgraded. Today several correlations are suggested[67-71]. In this study the work of Bosen and Engels[72] is used to describe the complex nature of the H_2O-H_2SO_4 VLE. The model treats ideal gasses above a liquid solution where the partial pressures p_i (index i refers to H_2O or H_2SO_4) are calculated from the general expression in eq. 6.1. χ_i is the liquid mole fraction, γ_i is an activity coefficient and p_i^0 is the vapor pressure of the pure substance[73,74]. The activity coefficient is derived from the NRTL (Non-Random Two Liquid model) equation[75] (eq. 6.2) wherein adjustable parameters are fitted to reproduce experimental data of total pressure, vapor phase composition and liquid molar enthalpy. The references of the experimental data are cited in the work of Bosen and Engels and the VLE is valid for liquid acid concentration up to 96 % m/m in the temperature range between 0 - 240 °C.

$$p_i(T, c_a) = x_i \gamma_i {p_i}^0 \qquad (6.1)$$

$$\ln(\gamma_i) = \frac{\sum_j^N \tau_{ji} G_{ji} x_j}{\sum_j^N G_{ji} x_j} + \sum_k^N \frac{G_{ik} x_k}{\sum_j^N G_{jk} x_j} \left(\tau_{ik} - \frac{\sum_n^N \tau_{nk} G_{nk} x_n}{\sum_j^N G_{jk} x_j} \right) \qquad (6.2)$$

$$G_{ij} = \exp(-\alpha_{ij}\tau_{ij}) \qquad \tau_{ij} = a_{ij} + \frac{b_{ij}}{T}$$

The number of phases P and chemically independent constituents C in the H_2O-H_2SO_4 VLE is 2. According to Gibbs phase rule in eq. 6.3 the system therefore yields 2 degrees of freedom F. This means that a given liquid acid strength c_a combined with a system temperature T can be applied to eq. 6.1 in order to determine the saturation pressures of H_2SO_4 and H_2O. In this work it is convenient to reverse the process and apply known bulk gas pressures of H_2SO_4 and H_2O (to eq. 6.1) in order to determine the acid dew point temperature and the condensing acid strength. I.e. the share of condensing acid and water.

$$F = C - P + 2 \qquad (6.3)$$

6.2 Modeling cases

Over the life time a large 2-stroke marine engine will operate at different loads, with various fuel compositions and in different environments. Consequently the cylinder liners will be subject to gas species of varying densities that alter the properties of sulfuric acid condensation. In order to limit the number of simulations a constant fuel sulfur content of 2 % m/m is used in this work for the operating conditions representing 25 % and 100 % engine load. In addition at each load the residual gas fraction is set to 3 % and 6 % m/m as seen in Table 6.1.

Case	load %	rpm rev/min	S % m/m	x_{res} % m/m	p_a bar	T_a °C	p_{max} bar	λ_t -	ε^* %
1	100	123	2.0	6	3.8	37	167	2.13	2.70
2	100	123	2.0	3	3.8	37	172	2.32	2.74
3	25	78	2.0	6	1.5	33	89	2.47	3.65
4	25	78	2.0	3	1.5	33	90	2.67	3.69

*at exhaust valve opening

Table 6.1. Cases studied to investigate the characteristics of sulfuric acid condensation on the cylinder liner of a large marine engine.

In section 4.2 the fuel heat release rate is determined for the two engine loads through a measured cylinder pressure trace. In this section the process is reversed and the “known” heat release rate is used to calculate the cylinder pressure history for the two engine loads at the different residual gas fractions. This is a fair approach since the effect of the residual gas fraction is small. The cylinder pressure plays a key role as it affects SO_3 formation and alters the properties of condensation

throughout the cycle. The resulting pressure histories are presented in Figure 6.2. If the residual gas fraction is increased the mass of trapped fresh gas reduces a little and leads to a slight reduction of the pressure trace as seen for the two engine loads in the figure.

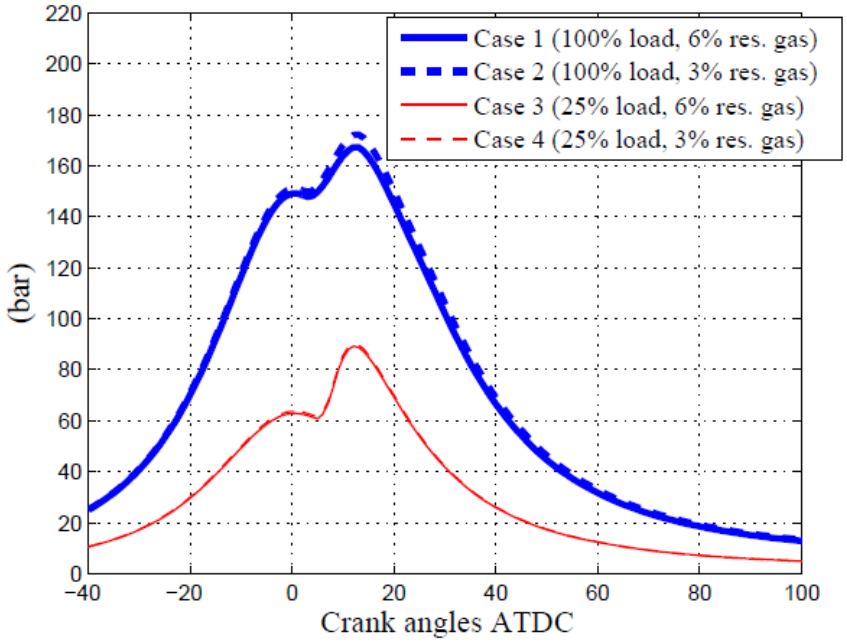

Figure 6.2. Cylinder pressure traces of the studied cases in Table 6.1.

6.3 Cylinder gas dew points

Modeled SO_3 concentrations over the expansion stroke of the cases in Table 6.1 are presented in Figure 6.3. Residual gasses from the prior engine cycle provide the initial SO_3 concentrations of less than 2 ppmv around TDC. As illustrated in an earlier section SO_2 is the primary sulfur compound in the hot gas products when the fuel sulfur burns and SO_3 forms at the expense of SO_2 during the expansion stroke at lower gas temperatures. Nevertheless the governing SO_3 reactions cease when the radical pool vanishes. As a result the final SO_3 concentrations are quite low and in the order of 14-18 ppmv. Formation of H_2O reflects the fuel burn rate and H_2O exists in much higher concentrations than SO_3. Since the two species forms in different stages during the expansion stroke the shape of the H_2O and the SO_3 pressure traces are quite different as seen in Figure 6.4. In general the SO_3 pressure peaks some 50-80 CA ATDC when SO_3 is formed in the cylinder gas. However as a result the high max pressure combined with the residual gas fraction the SO_3 pressure also tends to peak a little after TDC in case 1.

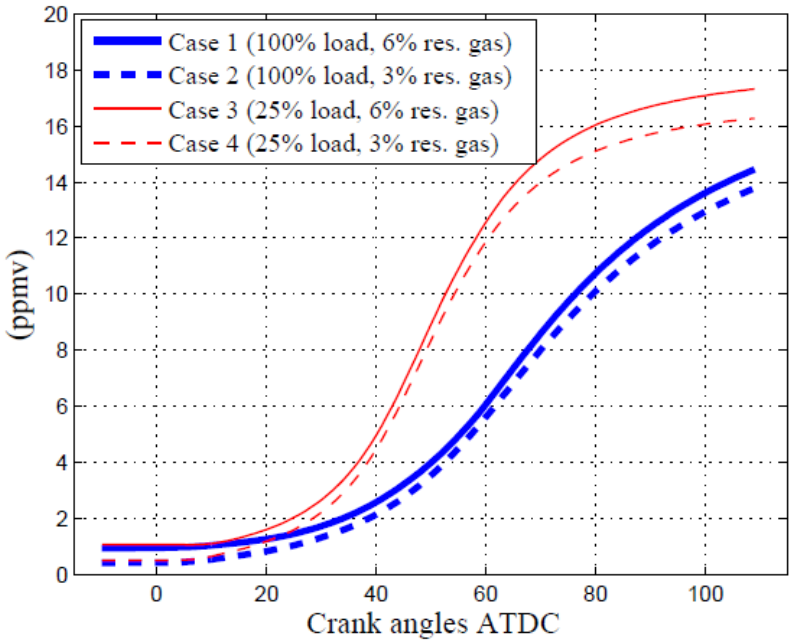

Figure 6.3. Modeled SO_3 concentrations of the cylinder gas of the studied cases in Table 6.1.

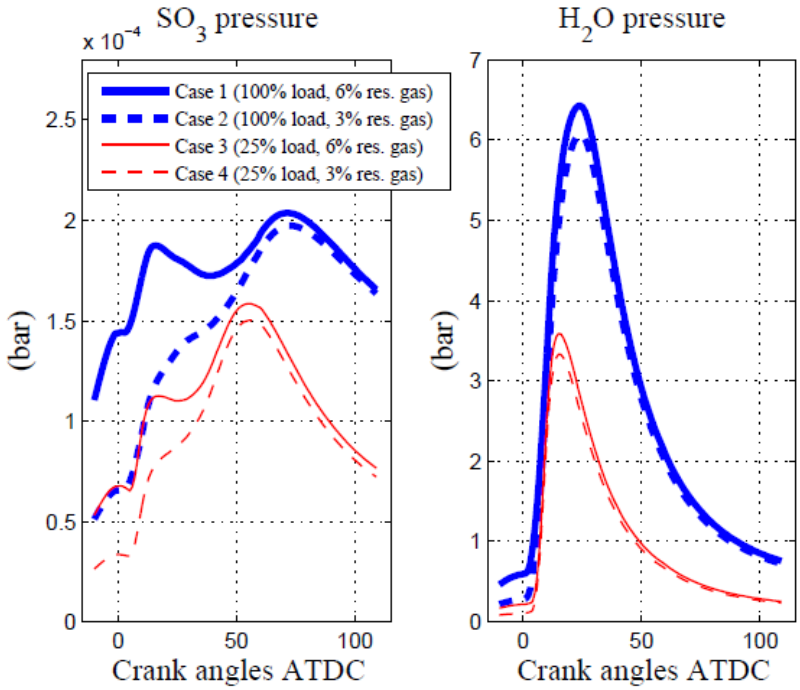

Figure 6.4. Modeled SO_3 and H_2O pressures of the studied cases in Table 6.1.

The sulfuric acid dew points presented in Figure 6.5 are calculated with eq. 6.1 and are based on the SO_3 and H_2O pressure traces in Figure 6.4. Max dew points of typically more than 200 °C are

located a little after TDC where the H_2O pressure is high. The ever reducing cylinder pressure during the expansion stroke provides that the acid dew point is comparably low even when SO_3 is formed in the cylinder gas. Nonetheless the acid dew point is strongly influenced by the minor SO_3 concentrations in the cylinder gas as it clearly exceeds the dew point of pure H_2O vapor as shown for case 1 and case 3 in the figure. The dashed horizontal lines in the figure represent constant liner temperatures of 170 °C and 210 °C that roughly correspond to the liner temperature at 25 % and 100 % engine load respectively. The temperature difference is rational but the liner temperature is highly variable in practice. It depends e.g. on the operating strategy and reduces from the piston position at TDC and throughout the expansion stroke. Nevertheless the anticipated liner temperatures are reasonably applied to illustrate the characteristics of sulfuric acid condensation on a cylinder liner.

When the sulfuric acid dew point of the cylinder gas is higher than the liner temperature sulfuric acid and water condense on the liner surface. Deposited liquid acid and water evaporates back into the gas phase if the dew point temperature is lower than the liner temperature. The liner area that is exposed to condensation scales with the number of crank angles between the point where condensation starts and stops. For instance in case 3 the liner area is exposed to condensation from ≈5 - 70 CA ATDC. The higher liner temperature in case 1 provides that the exposed surface is comparably low (≈15 - 40 CA ATDC) despite its higher dew point trace. At both 25 % and 100 % engine load the exposed area increases slightly with the residual gas fraction and from Figure 6.5 it can also be seen that the exposed liner area is reduced if the liner temperature is increased. As shown in the figure the dew point of H_2O remains lower than the anticipated liner temperatures. Consequently pure water does not condense on the liner under the given conditions. Should pure water condense on the liner then the liquid acid will be highly diluted.

In reality the H_2O pressure in the engine cylinder is affected by the humidity of the intake air and the applied assumption of a dry intake air acts to underestimate real dew points because marine engines often operate in very humid environments. In Figure 6.6 the relative humidity (φ) of the intake air in case 4 is varied from 0 to 1. Engine simulations show that the SO_3 formation is very weakly hampered by the humidity whereas the sulfuric acid dew point temperature and the H_2O concentration are clearly elevated as shown in the figure. The effect is most pronounced before TDC and the max dew point temperature is elevated ≈15 °C when the intake air is fully saturated instead of dry ($\varphi = 0$). In the remainder of the cycle the difference of the moist air is lower since H_2O forms during combustion in the cylinder gas. Nevertheless moist air significantly increases the liner area that is exposed to condensation. When $\varphi = 1$ condensation of sulfuric acid initiates before

TDC and condensation stops some 10-15 crank angles later than the case of dry intake air as seen in Figure 6.6.

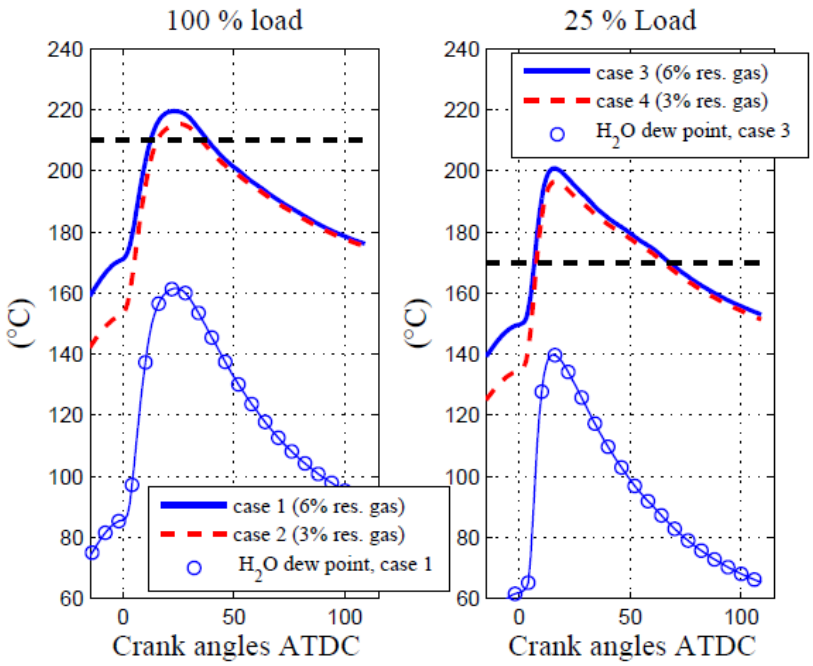

Figure 6.5. Sulfuric acid dew points of the cylinder gas of the studied cases in Table 6.1. The dashed horizontal lines represent constant cylinder liner temperatures of 170 °C and 210 °C.

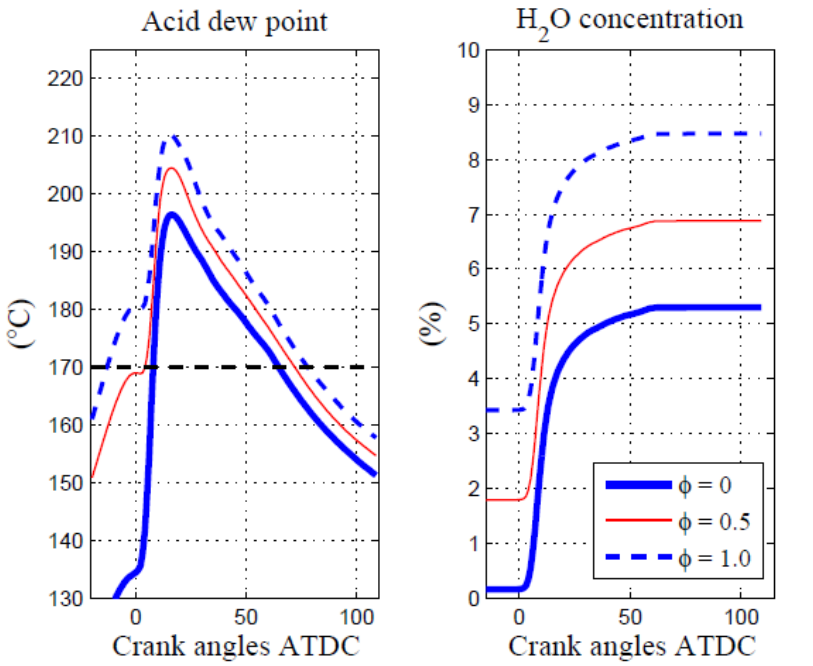

Figure 6.6. Sulfuric acid dew points and H_2O concentrations of the cylinder gas at different charge air humidities (φ) for case 4 in Table 6.1. The dashed horizontal line represents a fixed cylinder liner temperature.

6.4 Sulfuric acid condensation

Condensing acid strengths on the cylinder liner

The share of condensing sulfuric acid and water on the cylinder liner can be found from eq. 6.1. For the purpose either the H_2O or the H_2SO_4 pressure at the gas liquid interface must be applied together with a specified liner temperature. As was shown in Figure 6.5 the anticipated liner temperatures are always higher than the dew point of pure water. Furthermore the H_2O content in the bulk gas is orders of magnitude higher than the SO_3 content. This means that the amount of water that condenses together with sulfuric acid is very small compared to the H_2O contained in the bulk gas. Therefore the share of condensing acid and water (acid strength) is reasonably determined at each crank angle during the expansion stroke by assuming that the H_2O pressure at the gas-liquid interface equals the H_2O pressure in the bulk gas. In Figure 6.7 calculated values of the condensing acid strength $\frac{m_{acid}}{m_{acid}+m_{water}}$% are plotted against a specified liner temperature and the molar concentration of H_2O at 60 bar pressure. At high temperatures (> 200 °C) the acid strength is generally more than 50 % m/m and the influence of H_2O is low. However for lower temperatures the acid strength may approach zero and the H_2O concentrations acts to reduce the acid strength. When the acid strength is zero it means that the temperature is equal to or lower than the dew point of pure water.

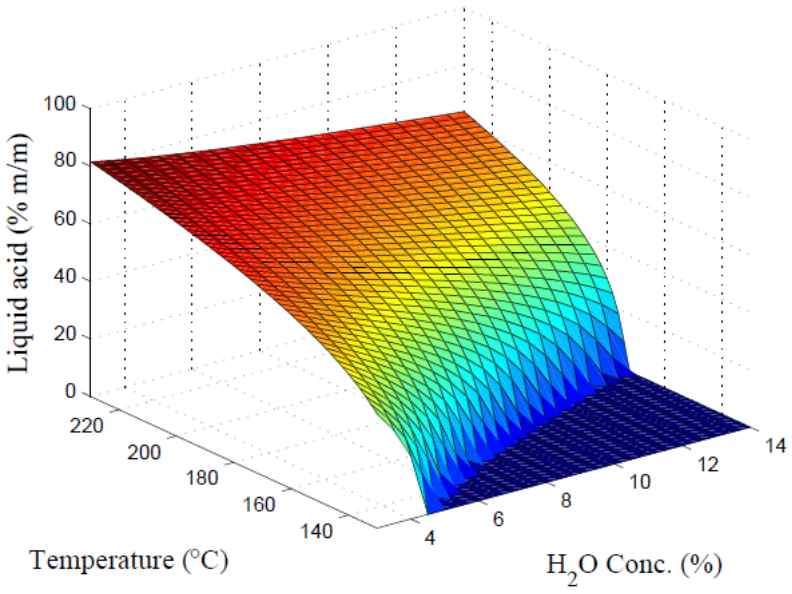

Figure 6.7. Liquid sulfuric acid strength relative to temperature and H_2O molar concentration at 60 bar pressure.

For each of the studied cases in Table 6.1 the resulting H_2O pressure trace in Fig. 6.4 is used together with the applied liner temperatures in order to determine the condensing acid strength over the expansion stroke. In agreement with Figure 6.7 the most diluted acid is formed on the liner when the H_2O pressure peaks close to p_{max} as seen in Figure 6.8. Furthermore the lower liner temperature (170 °C) at 25 % load results in lower acid strengths compared to 100 % load (210 °C). In addition the acid is slightly more diluted when the residual gas fraction is increased. If the intake air of case 4 is fully saturated (shown as case 4* in the figure) instead of dry the H_2O pressure is elevated by up to ~60 % during the expansion stroke and the condensing acid is somewhat more diluted as seen in the figure.

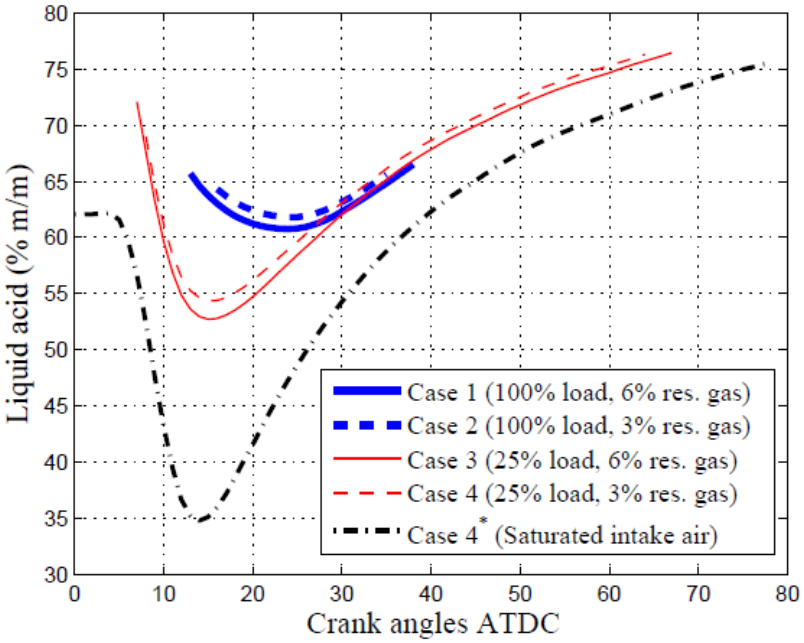

Figure 6.8. Condensing sulfuric acid strengths on the cylinder liner of the studied cases in Table 6.1.

The H_2O pressure peaks when the piston is still located in the upper part of the cylinder liner. At the same time the stability of the protective lube oil film is challenged by thermal degradation from the very hot cylinder gas, and the means to prevent acid corrosion via base additives may be hampered. Later in the expansion stroke the lube oil is likely more resistant to the colder cylinder gas and probably in a better condition to neutralize condensed acid. Different researchers states that dilute acid is most aggressive[65,76,77] and the results in Figure 6.8 therefore suggests that the most aggressive acid is condensing in the upper third of the liner. Clearly sulfuric acid corrosion needs also to be linked to the amount of deposited acid as well which is not yet considered. However

practical experiences from large marine engines shows in fact that acid corrosion is most pronounced in the top of the cylinder liner and could be related to the traces in Figure 6.8.

Deposition of sulfuric acid on the cylinder liner

Müllers analytic rate expressions of mass diffusion[66] in eq. 6.4 and 6.5 are used to calculate the rate of water and sulfuric acid condensation on the cylinder liner. The analytic expressions are based on the analogy between heat and mass transfer. In his theoretical approach Müller implemented the theory of a semi permeable gas-liquid interface that acts to hamper condensation due to convective motions of non-condensable gas species in the gaseous boundary layer. In addition Müllers rate expressions are based on the assumption of fully developed turbulence. g_w and g_a denotes the diffusion/condensation rates of water and sulfuric acid respectively. In eq. 6.4 the H_2SO_4 pressure at the gas liquid interface ($p_{a,w}$) is found by applying the known acid strength (c_a) and the liner temperature to eq. 6.1. In eq. 6.5 the H_2O pressure at the interface ($p_{w,w}$) cannot be approximated as before by its pressure in the bulk gas ($p_{w,b}$) since one would have to evaluate ln(1)=0. Instead the definition of the condensing acid strength in eq. 6.6 is applied. Hereby the system of equations 6.4-6.6 comprises the three unknowns g_a, g_w and $p_{w,w}$ that can be solved for each crank angle degree.

$$g_a = g_w \frac{k_w}{k_a}\frac{R_w}{R_a}\frac{\frac{p_{a,b}}{p}-\frac{p_{a,w}}{p}\left(\frac{p-p_{w,b}}{p-p_{w,w}}\right)^{\frac{k_w}{k_a}}}{1-\left(\frac{p-p_{w,b}}{p-p_{w,w}}\right)^{\frac{k_w}{k_a}}} \quad (6.4)$$

$$g_w = h\frac{R_g}{R_w c_{p,g}} ln\left(\frac{p-p_{w,w}}{p-p_{w,b}}\right) \quad (6.5)$$

$$c_a = \frac{g_a}{g_a+g_w} \quad (6.6)$$

Consistent with the heat and mass transfer analogy the diffusion rates in eq. 6.4 and 6.5 scale with the heat transfer coefficient (h). In this work the heat transfer coefficient is determined by applying Woschnis heat transfer correlation[41]. The coefficient is closely coupled to the system pressure and reduces throughout the expansion stroke after peaking around max pressure. The rate expressions also involve diffusion coefficients of H_2O and H_2SO_4 (k_w and k_a respectively). k_a is approximated from the binary diffusion coefficient of H_2SO_4 in a large excess of air[78] at 296 K (k_a = 0.08 atm

$cm^2\ s^{-1}$). Combined with the binary diffusion coefficient of H_2O in air[79] at 293 K (k_w = 0.260 atm $cm^2\ s^{-1}$) the aspect ratio of k_w/k_a is around 3. If the coefficients are equally dependent on temperature and pressure the ratio is not altered throughout the engine cycle. In any case the condensation rates of the present study are highly independent of k_w/k_a ratios up to 100.

Modeled rates of sulfuric acid condensation (g_a) on the cylinder liner over the expansion stroke are shown in Figure 6.9. The rates are expressed in mg/m^2 (deposited mass per exposed liner area) which means that the traces of case 3 and 4 benefit from a lower engine speed compared to case 1 and 2 (Table 6.1). Condensation takes place when $g_a > 0$. When g_a is negative liquid sulfuric acid evaporates from the liner surface and back into the gas phase. According to the dew point traces in Figure 6.5 the condensation begins when the crank angle is positioned a few CAD's after TDC. With reference to the SO_3 concentrations in Figure 6.3 it is understood that the high condensation rates at ≈10-20 CA ATDC must be caused by the SO_3 in the residual gasses combined with a high pressure and heat transfer rate. Even though SO_3 is formed in the gas products during the expansion stroke the reduction in pressure and heat transfer provides that the rate of acid condensation reduces as the piston moves away from TDC. In fact in case 1 and 2 the applied liner temperature of 210 °C provides that the evaporation of deposited sulfuric acid initiates even before any significant SO_3 has yet been formed. The lower liner temperature of 170 °C in case 3 and 4 involves more crank angles/time before the evaporation begins and the deposition of acid significantly profits from the SO_3 formed in the cylinder gas. As also indicated in Figure 6.9 the rate of condensation represents large negative numbers after the evaporation begins and deposited acid will under the given conditions evaporate completely form the liner surface before condensation starts in the following cycle.

To isolate the effect of the liner temperature with respect to sulfuric acid condensation the operating conditions of case 4 are used with two additional liner temperatures of 170 °C ±10 °C as seen in Figure 6.10. The initial deposition rates are basically the same. However the traces in the figure illustrate that the exposed liner area is very sensitive to the liner temperature as the position where the evaporation begins is "delayed" when the temperature is reduced. At 160 °C condensation takes place over more than 80 crank angles ATDC. Moreover the impact from SO_3 formed in the engine cycle increases when the liner temperature reduces. This is illustrated by the size of the peak rate that develops during the expansion stroke when temperature is lowered.

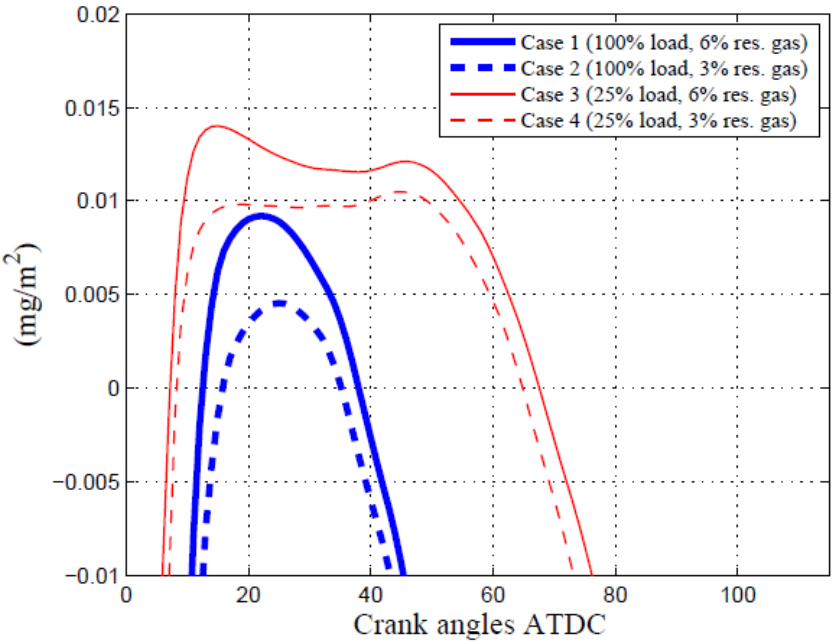

Figure 6.9. Condensation of sulfuric acid on the cylinder liner for the studied cases in Table 6.1.

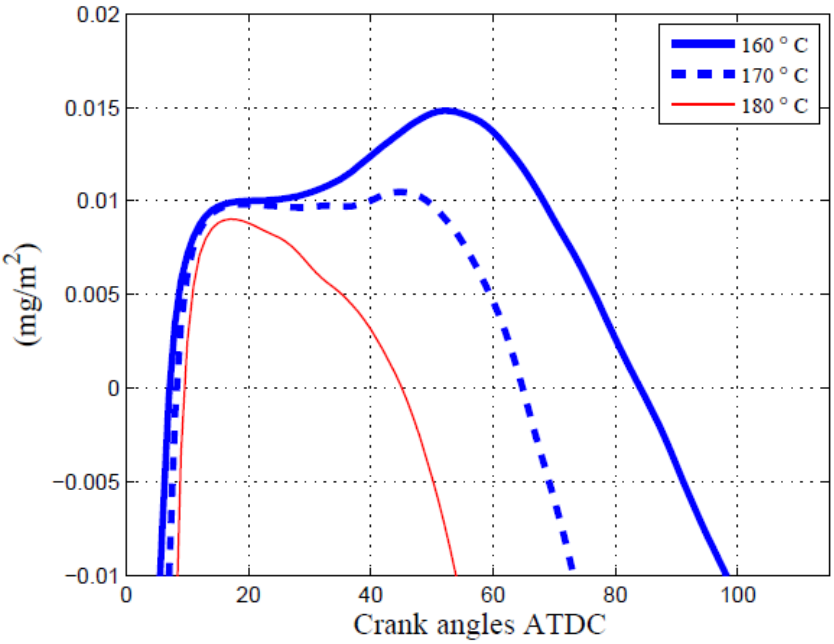

Figure 6.10. Condensation of sulfuric acid on the cylinder liner for case 4 in Table 6.1 at different liner temperatures.

The accumulated sulfuric acid mass over the expansion stroke until EVO are illustrated in Figure 6.11. The mass is assumed to be uniformly distributed on the exposed liner area and is at a max when the evaporation of acid begins. From the assumption that the condensate is uniformly

distributed on the liner area the following removal/evaporation of deposited acid is completed before EVO. The influence of the operating conditions becomes clearer when the peak points in the figure are compared. At 100 % engine load (case 1 and 2) the high liner temperature provides that the exposed liner area is comparably small and the deposited acid mass is relatively low. For the same load the mass is reduced by ≈ 60 % when the residual gas fraction is reduced from 6 % to 3 %. At 25 % engine load (case 3 and 4) the SO_3 that forms in the cylinder gas significantly adds to the deposition of acid. Yet the effect of the higher residual gas fraction is reduced to ≈22 %. The lower engine speed at 25 % engine load implies that the number of operating cycles is reduced by 1/3 relative to 100 % load. As a result the weight of case 3 and 4 ought to be reduced accordingly. Anyway the deposited acid mass per time unit will under the given conditions be several times higher at 25 % load.

Case 4* in Figure 6.11 are based on the same operating conditions as case 4 but the liner temperature is reduced by 10 °C to 160 °C. The difference between case 4 and 4* illustrates the influence of the lower temperature/larger exposed liner area. At the reduced temperature the deposited acid mass increases by a factor of more than 2 under the given conditions. It was shown in Figure 6.6 that moisturized intake air elevates the exposed surface area through a higher dew point trace. Case 4** in Figure 6.11 represents the same operating conditions as case 4 but the intake air is fully saturated. As illustrated the moist air basically doubles the deposited acid mass under the given conditions.

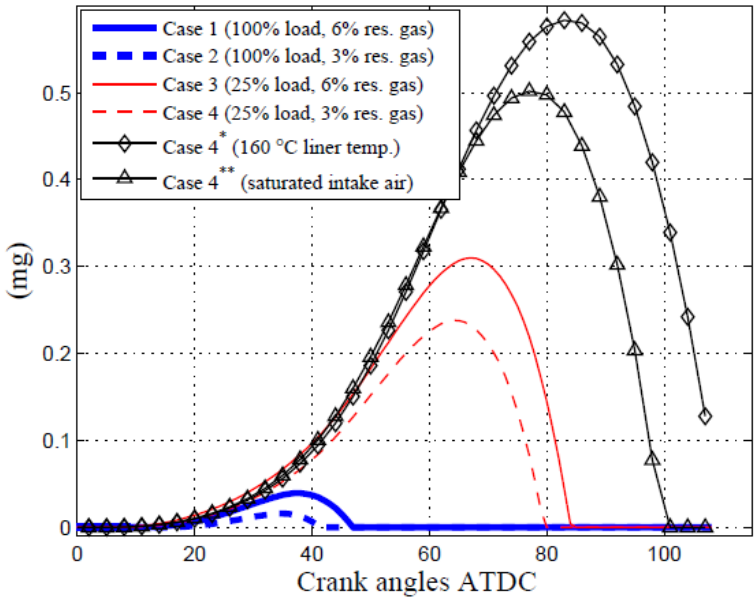

Figure 6.11. Accumulated sulfuric on the cylinder liner of the studied cases in Table 6.1. *The liner temperature is reduced 10 °C relative to case 4. **The intake air is saturated

In Figure 4.6 the fraction of fuel sulfur that is converted to SO_3 (ε) at EVO and at 25 % engine load is plotted against the fuel sulfur content. For the same operating conditions the deposited acid mass on the cylinder liner is shown in Figure 6.12. The values in the figure correspond to the point where evaporation starts like at the peak points in Figure 6.11. Under the given conditions the combined effect of elevated SO_3 pressures and exposed liner areas provide that the deposition of sulfuric acid scales with a quadratic regression relative to the sulfur content as illustrated in Figure 6.12.

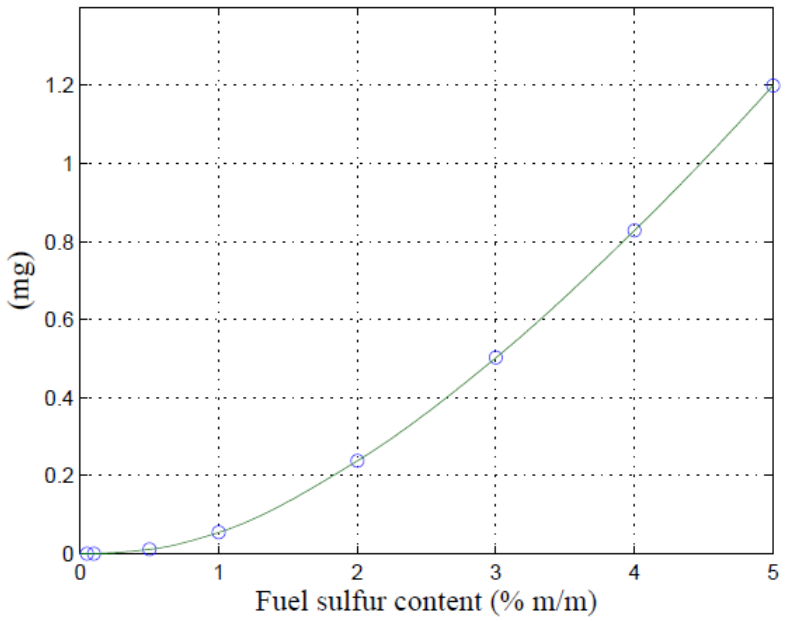

Figure 6.12. Deposited sulfuric acid on the cylinder liner during the expansion stroke for different fuel sulfur contents at 25 % engine load.

6.5 Acid mist formation

A flue gas that contains SO_3 and H_2O may form a sulfuric acid mist in the gaseous boundary layer very close to the gas liquid interphase if the gas is abruptly cooled e.g. by a cold surface. This was shown by Land[63] in his work with acid dew point meters. Mist formation is not considered in Müllers expressions that only consider mass diffusion in the boundary layer. Therefore condensation rates could well be overestimated as the mist tends to stay as small droplets in the gas. In order to treat acid mist formation the rate expression in eq. 6.7 is applied. Although rewritten in this work the expression is identical to the one provided by Land and is based on combined heat and mass transfer theory. The expression is always applicable and describes the rate of acid

condensation directly at the gas liquid interphase. However the sulfuric acid pressure gradient $\left(\frac{dp_a}{dT}\right)_s$ at the interface is not known. The gradient expresses the resulting gradient that exists at the gas liquid interphase whether or not mist is formed. A way to approach the gradient is by neglecting super saturation of the sulfuric acid. If super saturation is ignored a least gradient can be determined from the acid dew point curve[63]. To do this small temperature variations around a specified temperature (liner temperature) are considered at each crank angle degree. From eq. 6.1 the change in acid pressure (with respect to temperature variations) are then determined and the resulting $\left(\frac{dp_a}{dT}\right)_s$ gradient is evaluated. Moreover Land concluded that the Lewis number Le in eq. 6.7 is approximately 2.3 for SO_3/H_2SO_4 in a typical exhaust gas. This is in reasonably agreement with Müller[66] who stated that Le = 2.6 ± 5% throughout a motoring cycle.

$$g_a = \left(\frac{h}{pc_{p,g}Le}\frac{MW_a}{MW_g}\right)\left(\frac{dp_a}{dT}\right)_s \left(T_g - T_W\right) \quad (6.7)$$

In a situation where a sulfuric acid mist forms eq. 6.7 now represents the least rate of condensation. Eq. 6.4 represents the upper extreme. In practice the rate can be anywhere in-between the two extremes. Modeled traces of the two scenarios are compared in Figure 6.13 for case 3 in Table 6.1. At a liner temperature of 155 °C the traces intersects at 9 and 37 CA ATDC. In this interval acid mist may form in the boundary layer and potentially limit the rate of deposition by as much as the trace of eq. 6.7. Outside the interval eq. 6.7 combined with the least pressure gradient approach is no longer appropriate and the rate of deposition follows eq. 6.4. At a liner temperature of 165 °C the interval of mist formation is reduced and the lower extreme is increased. At a liner temperature of 175°C mist formation is no longer an issue. According to this simplified analysis the possibility of mist formation is very sensitive to the liner temperature. The possibility increases inversely with the liner temperature as illustrated in Table 6.2 for the model cases in Table 6.1. The plus symbols in the table symbolizes that mist may form. The cases are ranked from left to right in terms of increasing SO_3 and H_2O bulk gas pressures and the table shows that the probability of mist formation increases accordingly, especially due to a higher H_2O pressure. For the same reason humid intake air will add to the probability of acid mist formation. Moreover for a given case there is a tendency that mist is more likely to form when the liner temperature reduces.

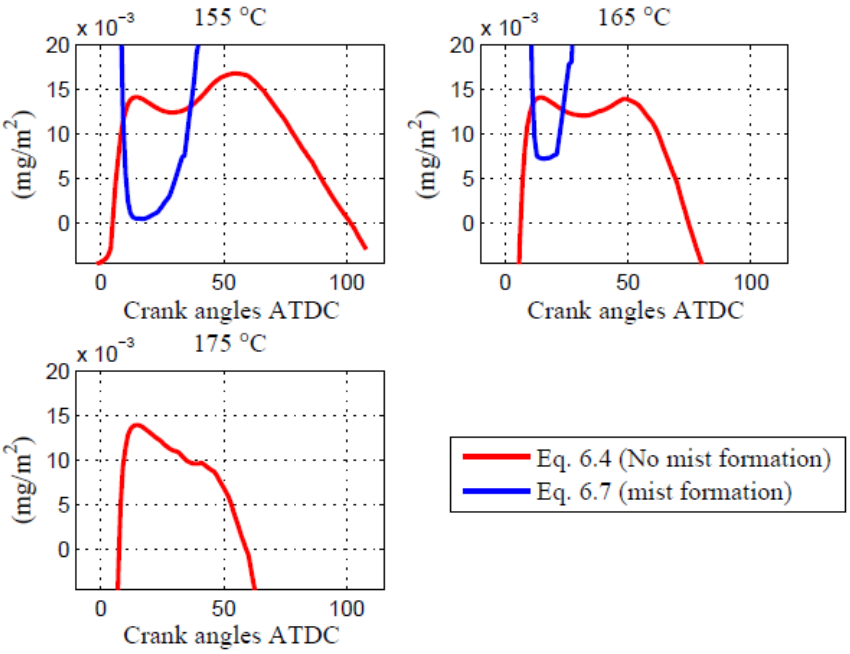

Figure 6.13. Sulfuric acid condensation rates on the cylinder liner for case 3 in Table 6.1 with and without mist formation in the gas species boundary.

	25% load x_{res} 3%	25% load x_{res} 6%	100% load x_{res} 3%	100% load x_{res} 6%
160 °C	+	+	+	+
170 °C	-	+	+	+
180 °C	-	-	+	+
190 °C	-	-	-	-

Table 6.2. The possibility of sulfuric acid mist formation in the gaseous boundary layer (for the cases in Table 6.1) at different liner temperatures. Plus symbols illustrate that mist may form.

Discussion

The results of sulfuric acid condensation presented in this work only clarify the characteristics of condensation on the cylinder liner of a large low speed marine engine. There are several reasons for this. First of all the assumption of a homogenous gas mixture eliminates the possible effect of higher condensation rates locally caused by stratified/heterogeneous SO_3 concentrations and turbulence intensities in the cylinder gas. The homogenous gas assumption also challenges the findings in terms of acid mist formation. Furthermore the dew point of sulfuric acid is based on the H_2O-H_2SO_4 VLE. The VLE is theoretically derived and show that even for fairly concentrated acid

strengths the saturation pressure of H_2O can be orders of magnitude higher that the H_2SO_4 pressure. This probably explains why the VLE to the authors' knowledge is not validated against experimental data. It is also shown in the present work that the cylinder liner temperature is a crucial parameter in terms of deposited sulfuric acid. In reality the applied assumption of a constant liner temperature trace over the expansion stroke is not correct as the temperature typically decreases throughout the stroke which increases the surface area that is exposed to acid condensation. For a better prediction of acid deposition a true temperature trace should be applied that will also indicate whether pure water is condensing on the liner in practice. It cannot be ruled out that much higher levels of water than acid is condensing on the liner surface. Pure water may play a significant role in terms of corrosion as diluted acid tends to be more aggressive than concentrated acid. Water itself is corrosive in the presence of oxygen and SO_2 may dissolve in water and form corrosive sulfurous acid.

Sulfuric acid mist formation in the gaseous boundary layer can serve to reduce sulfuric acid corrosion by hampering the deposition of acid onto the liner surface. According to results of this work the mist formation is most prominent at higher engine loads. On the other hand the probability of mist formation tends to reduce with the liner temperature that normally increases with the engine load. Thus, at higher engine loads the higher liner temperature might counteract the mist formation.

Conclusions

A phenomenological 0D multizone engine model that applies a detailed sulfur reaction mechanism is formulated in order to examine SO_3 formation (from oxidation of fuel containing sulfur) in a large low speed two-stroke marine diesel engine. By splitting the injected fuel into multiple burned gas zones and by applying experimental data as model input and calibration data the model simulates realistic gas conditions at 25 - 100 % engine load. Due to thermodynamic restrictions SO_3 is unlike SO_2 hardly present at the highest gas temperatures in a diesel process. SO_3 is increasingly favored at the expense of SO_2 as the hot gas products cool during the expansion stroke and is primarily formed in the temperature range between 1300 K and 2000 K. Above 1650 K SO_3 is in equilibrium but since the governing reactions freeze at around 1300 K the presence of SO_3 in the exhaust gas is much less than thermodynamically predicted. The fraction of fuel sulfur that is converted to SO_3 (ε) in the exhaust increases with the cylinder pressure (engine load) but decreases

with the engine speed. The trends agree with engine tests performed with a heavy duty single cylinder HFO-fueled medium speed engine. In addition high shares of premixed combustion are found to increases SO_3 formation remarkably. The adverse effects of operating pressure and engine speed of a large marine engine means that the resulting ε-values are quite similar for the full operational range. A few percent of the fuel is generally converted to SO_3. For a diffusion controlled (diesel) combustion process SO_3 is primarily formed from a reaction involving $HOSO_2$ and O_2 where the $HOSO_2$ intermediate is formed by the mayor sulfur compound SO_2 and OH. Another significant pathway to SO_3 is the direct reaction between SO_2 and O(+M). The two reactions contribute to about 90% of the SO_3 formed in the engine cylinder. Formation of H_2SO_4 is confined to temperatures of less than 1000 K and no significant H_2SO_4 is modeled in the cylinder gasses. It is likely that gaseous H_2SO_4 forms prior to condensation very close to the liner surface (due to the abrupt cooling) from a nearly instant reaction between SO_3 and H_2O. For that reason SO_3 and H_2SO_4 are reasonably lumped together. With a homogenous cylinder gas composition the characteristics of sulfuric acid condensation on a directly exposed cylinder liner (no lube oil film) of constant temperature is examined by combining engine model results with diffusive mass transfer and H_2O-H_2SO_4 VLE. Results demonstrate that SO_3 from the residual gasses is responsible for the peak acid dew points of typically more than 200 °C close to max cylinder pressure. The operating pressure, fuel sulfur content and residual gas fraction elevates the SO_3 pressure and increases the rate of condensation. Similarly the deposition may increase with the charge air humidity through a higher dew point trace and exposed liner area. However higher liner temperatures associated with higher engine loads hampers the deposition compared to lower loads. Even small increments of the liner temperature will under the given conditions reduce the deposition significantly.

Nomenclature

Symbol		Unit
A	Arrhenius pre-exponential factor	Depends on the reaction
c_a	Condensing acid strength	kg/kg
$c_{p,g}$	Specific heat capacity of gas	J/kg-K
E	Activation Energy	J/mol, cal/mol
g_a	Rate of condensing sulfuric acid	mg/m^2-s
g_w	Rate of condensing water	mg/m^2-s
h	Heat transfer coefficient	W/m^2-K
H_k^o	Standard state molar enthalpy of the *k*th species	joule/mole
k_a	Binary diffusion coefficient of H_2SO_4 in air	atm cm^2 /s
k_w	Binary diffusion coefficient of H_2O in air	atm cm^2 /s
k_f	Forward reaction rate	Depends on the reaction
k_b	Backward reaction rate	Depends on the reaction
K_c	Equilibrium constant in concentration units	Depends on the reaction
K_p	Equilibrium constant in pressure units	Depends on the reaction
Le	Lewis number	-
m	mass	kg
$\dot{m}_a$	Charge air flow	kg/h
m_{max}	Potential mass of air in a burned zone	kg
$\dot{m}_{mix}$	Gas mixing in burned zone per CAD	kg/CA°
MW_a	Molecular weight of H_2SO_4	g/mole
MW_g	Molecular weight of gas mixture	g/mole
n	Number of species in the reaction	-
N	Number of CAD's from TOI to EVO	-
P^o	Pressure of one standard atmosphere	dynes/cm^2
p_i^0	Vapor pressure of a pure substance	Pa
p_{H2O}	Vapor pressure of H_2O	mm Hg
p_{H2SO4}	Vapor pressure of H_2SO_4	mm Hg
p_{max}	Maximum cylinder pressure	Pa
p_a	Charge air pressure	Pa
p_{inj}	Fuel injection pressure	Pa
$p_{a,b}$	Partial pressure of H_2SO_4	Pa
$p_{a,b}$	Partial pressure of H_2SO_4 in bulk gas	Pa
$p_{a,w}$	Partial pressure of H_2SO_4 at gas-liquid interface	Pa
$p_{w,b}$	Partial pressure of H_2O in bulk gas	Pa
$p_{w,w}$	Partial pressure of H_2O at gas-liquid interface	Pa

Symbol		Unit
q_{net}	Rate of progress	mole/cm3
Q_f	Fuel heat	kJ
Q_{HT}	Heat transfer	kJ
Q_{net}	Net heat release	kJ
R	Gas constant	J/mole-K
R_a	Specific gas constant of H_2SO_4	J/kg-K
R_w	Specific gas constant of H_2O	J/Kg-K
R_g	Specific gas constant of cylinder gas	J/Kg-K
S_k^o	Standard state molar entropy of the *k*th species	joule/mole-K
T	Gas temperature	K
T_a	Charge air temperature	K
T^*	Intermediate gas temperature	K
$T_{a,d}$	Acid dew point temperature	K
T_{exh}	Exhaust gas temperature	K
T_g	Mean cylinder/bulk gas temperature	K
T_w	Gas-liquid interface/liner wall temperature	K
$T_{w,d}$	Dew point temperature of pure water	K
Δt_e	Gas residence time in exhaust system	s
Δt_{inj}	Duration of fuel injection	μs
v	Stoichiometric coefficient	-
V	Cylinder volume	m^3
$\bar{V}$	Relative fresh gas volume	-
x_b	Fuel burn fraction	-
x_i	Mole fraction in the liquid solvation	-
β	Arrhenius temperature exponent	-
β	Gas mixing constant	-
θ	Crank angle position	CA°
θ_{ign}	Point of ignition	CA°
Δθ	Computational step	CA°
ε	Fraction of fuel sulfur converted to SO_3	-
λ	Excess air ratio	-
λ_t	Trapped excess air ratio	-
γ	Ratio of specific heats	-
γ_i	Activity coefficient	-

Abbreviations

BDC	Bottom dead center
CA	Crank angle
CAD	Crank angle degrees
CA ATDC	Crank angles after top dead center
CA BTDC	Crank angles before top dead center
CCD	Controlled condensation
CCAI	Calculated carbon aromaticity index
CCS	Controlled condensation system
EVO	Exhaust valve opening
ECA	Emission controlled areas
FTIR	Fourier transform infrared spectroscopy
IMEP	Indicated mean effective pressure
IMO	International maritime organization
IPA	Iso-propanol
LHW	Lower heating value
MCR	Maximum continuous rating
MEP	Mean effective pressure
NRTL	Non-random two-liquid model
ROHR	Rate of heat release
rpm	Revolutions per minute
SOI	Start of injection
S	Sulfur
TBN	Total Base Number
TDC	Top dead center
TOI	Time of ignition
VLE	Vapor liquid equilibrium

References

1. Heywood, J. B. *Internal combustion engine fundamentals;* McGraw-Hill: New York, 1988; .

2. Turns, S. R. *An introduction to combustion / concepts and applications*; McGraw-Hill: New York, 2012.

3. International Maritime Organization: http://www.imo.org/Pages/home.aspx.

4. Aabo, K. CIMAC Heavy Fuel Oil Working Group, and Experience from Operation on Today's Fuels and Low Sulphur Fuels. In *24th International Bunker Conference*; Rotterdam, 2003; .

5. Hengeveld, J.; Schenk, C.; Aabo, K. The Role of Temperature and Pressure in the Wear Process in Low Speed Diesel Engines. Shell, 2000.

6. Weiss, E. K. J.; Busenthuer, B.; Hardenberg, H. O. Diesel Fuel Sulfur and Cylinder Liner Wear of a Heavy-Duty Diesel Engine. *SAE paper* **1987**, *872148*.

7. Chew, F.; McGeary, T. Study of the Relationship between Cylinder Lubricant Drain Condition and Performance Parameters of 2-Stroke Crosss-head Engines. In *CIMAC Congress*; Hamburgh, 2001; .

8. Engel, P. K.; Thompson, R. E.; Silvestrinin, R. Corrosion and Fouling Potential in Diesel Exhausts. *Mech. Eng.* **1979**, *101*, 598-606.

9. Stiesch, G., Ed.; *Modeling Engine Spray and Combustion Processes;* Springer: 2003; .

10. Schramm, J.; Henningsen, S.; Sorenson, S. C. Modeling of Corrosion of Cylinder Liner in Diesel Engines Caused by Sulphur in the Diesel Fuel. *SAE paper* **1994**, *940818*.

11. Hindiyarti, L.; Glarborg, P.; Marshall, P. Reactions of SO3 with the O/H radical pool under combustion conditions. *J. Phys. Chem. A* **2007**, *111*, 3984-3991.

12. Levy, A.; Merryman, E.; Reid, W. Mechanisms of Formation of Sulfur Oxides in Combustion. *Environ. Sci. Technol.* **1970**, *4*, 653-&.

13. Gleason, J. F.; Sinha, A.; Howard, C. J. Kinetics of the Gas-Phase Reaction HOSO2+O2=>HO2+SO3. *J. Phys. Chem.* **1987**, *91*, 719-724.

14. Gleason, J. F.; Howard, C. J. Temperature Dependence of the Gas-Phase Reaction HOSO2+O2=>HO2+SO3. *J. Phys. Chem.* **1988**, *92*, 3414-3417.

15. Laakso, D.; Smith, C. E.; Goumri, A.; Rocha, J.; Marshall, P. Theoretical Studies of the RSOO, ROSO, RSO(2) and HOOS (R=H, CH(3)) Radicals. *Chem. Phys. Lett.* **1994**, *227*, 377-383.

16. Goumri, A.; Laakso, D.; Rocha, J.; Smith, C. E.; Marshall, P. Computational studies of the potential energy surface for O(3P)+H2S: Characterization of transition states and the enthalpy of formation of HSO and HOS. *J. Chem. Phys. (USA)* **1995**, *102*, 161-169.

17. Goumri, A.; Rocha, J.; Laakso, D.; Smith, C. E.; Marshall, P. Computational studies of the potential energy surface for O(1 D)+H2S: Characterization of pathways involving H2 SO, HOSH, and H2OS. *J. Chem. Phys.* **1994**, *101*, 9405-9411.

18. Glarborg, P.; Kubel, D.; DamJohansen, K.; Chiang, H.; Bozzelli, J. Impact of SO2 and NO on CO oxidation under post-flame conditions. *Int. J. Chem. Kinet.* **1996**, *28*, 773-790.

19. Merryman, E. L.; Levy, A. Enhanced SO3 Emissions from staged Combustion. *Symp. Int. Combust.* **1979**, 727-736.

20. Hedley, A. B. Sulphur trioxide in combustion gases. *Fuel Soc. J.* **1962**, *13*, 45-54.

21. Dooley, A.; Whittingham, G. The Oxidation of Sulphur Dioxide in Gas Flames. *Trans. Faraday Soc.* **1946**, *42*, 354-366.

22. Johnson, G. M.; Matthews, C. J.; Smith, M. Y.; Williams, D. J. Distribution of sulfur species in the burnt gas of fuel-rich propane-air flames. *Combust. Flame* **1970**, *15*, 211-214.

23. Schneider, D. R.; Bogdan, Z. Modelling of SO3 Formation in the Flame of a Heavy-oil Fired Furnace. *Chem Biochem Eng Q* **2003**, *17*, 175-181.

24. Srivastava, R. K.; Miller, C. A.; Erickson, C.; Jambhekar, R. *Emissions of Sulfur Trioxide From Coal-Fired Power Plants,* Riley Power Inc. Report No. RPI-TP-0178, 2002.

25. Denne, C.; Himes, R. *Continuous Measurement Technologies for SO_3 and H_2SO_4 in Coal-Fired Power Plants,* Technical Report, EPRI (Electric Power Research Institute): Palo Alto, 2004.

26. Hunter, S. C. Formation of SO3 in gas turbines. *J. Eng. Power* **1982**, *104*, 44-50.

27. Lebedev, A. B.; Secundov, A. N.; Starik, A. M.; Titova, N. S.; Schepin, A. M. Modeling study of gas-turbine combustor emission. *Proc. Comb. Inst.* **2009**, *32*, 2941-2947.

28. Moniruzzaman, C. G.; Yu, F. A 0D aircraft engine emission model with detailed chemistry and soot microphysics. *Combust. Flame* **2012**, *159*, 1670-1686.

29. Goodwin, D. G. Defining phases and interphases - Cantera 1.5. Tech. rep. California Inst. of Technology, 2003.

30. Goodwin, D. G. Cantera C++ users guide. California Inst. of Technology, 2002.

31. Alzueta, M.; Bilbao, R.; Glarborg, P.; Alzueta, M.; Bilbao, R.; Glarborg, P. Inhibition and Sensitization of Fuel Oxidation by SO2. *Combust. Flame* **2001**, *127*, 2234-2251.

32. Yilmaz, A.; Hindiyarti, L.; Jensen, A. D.; Glarborg, P.; Marshall, P. Thermal dissociation of SO3 at 1000-1400 K. *J Phys Chem A* **2006**, *110*, 6654-6659.

33. Rasmussen, C. L.; Glarborg, P.; Marshall, P. Mechanisms of radical removal by SO2. *Proceedings of the Combustion Institute* **2007**, *31*.

34. Glarborg, P.; Glarborg, P. Hidden interactions - Trace species governing combustion and emissions. *Proceedings of the Combustion Institute* **2007**, *31*, 77-98.

35. Zabetta, E. C.; Kilpinen, P. Improved NOx submodel for in-cylinder CFD simulation of low- and medium-speed compression ignition engines. *Energy & fuels* **2001**, *15*, 1425-1433.

36. Reiner, T.; Arnold, F. Laboratory Investigations of Gaseous Sulfuric-Acid Formations via SO3+H2O+M=>H2SO4+M: Measurements of the Rate-Constant and Product Identification. *J. Chem. Phys.* **1994**, *101*, 7399-7407.

37. Lavoie, G. A.; Heywood, J. B.; Keck, J. C. Experimental and Theoretical study of Nitric Oxide Formation in Internal Combustion Engines. *Combust. Sci. Technol.* **1970**, *1*, 313-26.

38. Sorenson, S. C. *Engine Principles and Vehicles;* Sorenson , Spencer C.: Lyngby, Denmark, 2012; , pp 736.

39. Bartok, W.; Sarofim, A. *Fossil fuel combustion / A source book*; Wiley: New York, 1991.

40. Cordtz, R.; Schramm, J.; Andreasen, A.; Eskildsen, S. S.; Mayer, S. Modeling the distribution of sulfur compounds in a large two stroke diesel engine. *Energy Fuels* **2013**, *27*, 1652-1660.

41. Ferguson, C. R.; Kirkpatrick, A. T., Eds.; *Internal combustion engines / applied thermosciences;* Wiley: New York, 2001; .

42. Blair, G. P., Ed.; In *Design and Simulation of Two-Stroke Engines;* SAE: Warrendale, PA, 1996; .

43. Dec, J. E.; Espey, C. Soot and Fuel Distributions in a D.I. Diesel Engine Via 2-D Imaging. *SAE paper* **1992**, *922307*.

44. Scholl, K. W.; Sorenson, S. C. Combustion of soybean oil methyl ester in a direct injection diesel engine. *SAE Spec Publ SP* **1993**, 211-223.

45. Cordtz, R.; Schramm, J.; Rabe, R. Investigating SO_3 Formation from the Combustion of Heavy Fuel Oil in a Four-Stroke Medium-Speed Test Engine. *Energy and Fuels* **2013**, *27*.

46. Harndorf, H.; Kösel, R.; Volkart, A. Optimierung der Mess- und Auswerteparameter zur Analyse von Zülinderdruckverlaufen. *MTZ* **1992**, *53*, 136 ff.

47. Zacharias, F. *Analytische Darstellung der Thermodynamischen Eigenschaften von Verbrennungsgassen*, Dissertation TU Berlin, 1966.

48. Hohenberg, G. *Experimentelle Erfassung der Wandwärme in Kolbenmotoren*, Habilitationsschrift, Technische Universität Graz, 1983 , .

49. Hohenberg, G. F. Advanced Approaches for Heat Transfer Calculations. *SP* **1979**, 61-79.

50. Zeelenberg, A. P.; Fijn, v. D.; Barker, H. L. Ignition Performance of Fuel Oils in Marine Diesel Engines. *Int Congress Combus Engines* **1983**, 1455-1469.

51. Valencia, F. A.; Armas, I. P. Ignition Quality of Residual Fuel Oils. *J. Mar. Res* **2005**, *2*, 77-96.

52. Verhoff, F. H.; Banchero, J. T. Predicting Dew Points of Flue Gases. *Chem. Eng. Prog.* **1974**, *70*, 71-72.

53. Pierce, R. Estimating Acid Dewpoints in Stack Gases. *Chem. Eng.* **1977**, *84*, 125-128.

54. Fleig, D.; Vainio, E.; Andersson, K.; Brink, A.; Johnsson, F.; Hupa, M. Evaluation of SO3 Measurement Techniques in Air and Oxy-Fuel Combustion. *Energy Fuels* **2012**, *26*, 5537-5549.

55. Froment, G. F.; Bischoff, K. B. Chemical reactor analysis and design. **1990**.

56. Livbjerg, H.; Villadsen, J. Kinetics and effectiveness factor for SO2 oxidation on an industrial vanadium catalyst. *Chemical Engineering Science* **1972**.

57. Flagan, R. C.; Seinfeld, J. H. *Fundamentals of air pollution engineering*, Prentice Hall, Inc. , Englewood Cliffs, New Jersey, 1988.

58. Vainio, E.; Fleig, D.; Brink, A.; Andersson, K.; Johnsson, F.; Hupa, M. Experimental Evaluation and Field Application of a Salt Method for SO3 Measurement in Flue Gases. *Energy Fuels* **2013**.

59. Ibanez, J. G.; Batten, C. F.; Wentworth, W. E. Simultaneous determination of SO3(g) and SO2(g) in a flowing gas. *Ind. Eng. Chem. Res. Industrial & engineering chemistry research* **2008**, *47*, 2449-2454.

60. United States Environmental Protection Agency (EPA): Available online: http://www.epa.gov/ttn/emc/ctm-013.pdf.

61. Jackson, P. J.; Hilton, D. A.; Buddery, J. H. Continuous Measurement of Sulphuric Acid Vapour in Combustion Gases using a Portable Automatic Monitor. *J. Inst. Energy* **1981**, *54*, 124-135.

62. Jaworowski, R. J.; Mack, S. S. Evaluation of Methods for Measurements of SO3/H2SO4 in Flue-Gas. *J. Air Pollut. Control Assoc.* **1979**, *29*, 43-46.

63. Land, T. Theory of Acid Deposition and its Application to the Dew-Point Meter. *J. Inst. Fuel* **1977**, *50*, 68-75.

64. Gaydon, A. G. Continuous Spectra in Flames: The Role of Atomic Oxygen in Combustion. *Proceedings of the Royal Society of London.Series A, Mathematical and Physical Sciences* **1944**, *183*, 111-124.

65. Teetz, C. Investigation into Reducing Low Temperature Corrosion in Diesel Engines. *VDI Forschungsh.* **1984**.

66. Mueller, P. Dew point temperatures in cylinders of diesel engines working with fuel that contains sulfur (Taupunkttemperaturen im Zylinder von Dieselmaschinen bei schwefelhaltigen Kraftstoffen, Nr 486). *VDI -- Forschungsheft* **1961**, *27*, 1-56.

67. Abel, E. The Vapour-phase above the System Sulphuric Acid-Water. *J. Phys. Chem.* **1946**, *50*, 260.

68. Greenewalt, C. H. Partial pressure of water out of aqueous solutions of sulfuric acid. *Ind. Eng. Chem.* **1925**, *17*, 522-523.

69. Gmitro, J. I.; Vermeulen, T. Vapor-Liquid Equilibria for Aqueous Sulfuric Acid. *A. I. Ch. E J.* **1964**, *10 No 5*, 740-746.

70. Wilson, R. W.; Stein, F. P. Correlation of sulfuric acid-water partial pressures. *Fluid Phase Equilib.* **1989**, *53*, 279-288.

71. Pessoa, F. L. P.; Siqueira Campos, C. E. P.; Uller, A. M. C. Calculation of vapor-liquid equilibria in aqueous sulfuric acid solutions using the UNIQUAC equation in the whole concentration range. *Chemical Engineering Science* **2006**, *61*, 5170-5175.

72. Bosen, A.; Engels, H. Description of the phase equilibrium of sulfuric acid with the NRTL equation and a solvation model in a wide concentration and temperature range. *Fluid Phase Equilib.* **1988**, *43*, 213-230.

73. Nist Chemistry WebBook: http://webbook.nist.gov/chemistry/.

74. Luchinskii, G. P. Physical-chemical Study of the H2O-SO3 System, I. Equilibrium in the vapor and the liquid phase. *Zh. Fiz. Khim.* **1956**, *30*, 1207.

75. Renon; Prausnitz Local compositions in thermodynamic excess functions for liquid mixtures. *AIChE J.* **1968**, *14*, 135-144.

76. van Helden, A. K. *A Physio-chemical Model of Corrosive Wear in Low-Speed Diesel Engines. CIMAC Conference Report D-9;* 1987; .

77. Yahagi, Y. Corrosive wear of diesel engine cylinder bore. *Tribol. Int.* **1987**, *20*, 365-373.

78. Poschl, U.; Canagaratna, M.; Jayne, J. T.; Molina, L. T.; Worsnop, D. R.; Kolb, C. E.; Molina, M. J. Mass Accommodation Coefficient of H2SO4 Vapor on Aqueous Sulfuric Acid Surfaces and Gaseous Diffusion Coefficient of H2SO4 in N2/H2O. *J. Phys. Chem.* **1998**, *102*, 10082.

79. Reid, R. C.; Sherwood, T. K., Eds.; *The properties of gases and liquids. Their estimation and correlation;* McGraw-Hill Book Company: New York, 1958; .

Appendices

energy&fuels

Article

pubs.acs.org/EF

Modeling the Distribution of Sulfur Compounds in a Large Two Stroke Diesel Engine

Rasmus Cordtz,*[,†] Jesper Schramm,[†] Anders Andreasen,[‡] Svend S. Eskildsen,[‡] and Stefan Mayer[‡]

[†]Technical University of Denmark, Kgs. Lyngby, Denmark 2800

[‡]MAN Diesel & Turbo, Denmark

ABSTRACT: In many years large low speed marine diesel engines have consumed heavy fuel oils with sulfur contents in the order of 2.5−4.5 wt %. Present legislation requires that the fuel sulfur is reduced, and in the near future the limit will be 0.5 wt % globally. During combustion most of the sulfur is oxidized to SO_2 from which a fraction is further oxidized to SO_3. SO_3 may combine with H_2O and condense as liquid sulfuric acid that promotes corrosive wear on e.g. cylinder liners. To extend engine lifetime and reduce costs for lubrication it is pivotal to identify formation of SO_3 with respect to operational conditions and sulfur feed. This work presents a computational model of a large low speed two-stroke diesel engine where a 0D multizone approach including a detailed reaction mechanism is employed in order to investigate in cylinder formation of gaseous SO_3 where fuel burn rates are based on experimental pressure traces. In contrast to NO the SO_3 does not really form at the highest combustion temperatures, but like NO the formation of SO_3 is very sensitive to the rate that fresh air mixes with hot combustion products. Consequently a simple mixing rate is proposed and calibrated in order to meet experimental results of NO. For a large low speed diesel engine the model shows that 3−5% of the injected sulfur is oxidized to SO_3 that is formed primarily in the temperature range from 2000 to 1300 K during cylinder expansion. In addition the model is used to reduce the full reaction mechanism from 96 to 7 elementary sulfur reactions without compromising the SO_3 to SO_2 ratio.

INTRODUCTION

Many industries as well as the maritime industry are forced to deal with environmental concerns and reduce harmful gaseous emissions such as sulfur oxides which are the principal cause of acid rain. In this context the International Maritime Organization (IMO) has defined future legislation that will globally lead to a maximum of 0.5 wt % fuel sulfur in 2020 and 0.1 wt % from 2015 in some environmentally controlled areas (ECA) unless after treatment equipment such as scrubbers are installed onboard.

During combustion the sulfur is oxidized primarily to SO_2 beside a small fraction of SO_3. Experimental results on the fraction of SO_3 to sulfur oxides in diesel exhaust gas range from 1−8%[1,2] depending on operational conditions and fuel quality. In practice SO_3 is known to promote corrosive wear on surfaces as it forms liquid sulfuric acid (H_2SO_4) in combination with H_2O.[3−5] H_2SO_4 may condense on a cylinder liner either as concentrated acid or diluted acid in water[3] if the surface temperature is less than the respective dew point temperatures. In order to neutralize the acid and hamper corrosion commercial lube oils are formulated with a high alkalinity expressed by the total base number (TBN). Nevertheless in operation an acceptable level of surface corrosion is sought to assist the lube oil layer between the liner and the moving piston rings. Reducing the TBN and lube oil feed rate according to the fuel sulfur seems logical, but in reality the answer is not that simple and new lube oil formulations are likely needed in the future to cope with lower sulfur feed rates.

Commercial lube oils are typically formulated to operate with a fuel sulfur content of around 3 wt % on average, and recent examples of operational difficulties with low sulfur fuels in large two-stroke engines are reported. For instance severe wear rates due to scuffing (local metal to metal contact)[6] and heavy deposits of thermal degraded lube oil on piston and ring pack that may ultimately lead to severe wear.[7] Thus in practice the sulfur is believed to contribute to antiwear.

Despite a large concern especially in the 1990s with respect to SO_3 formation in diesel engines no results on experimental measurements of SO_3 from large two-stroke diesel engines have been published in peer reviewed journals in the past.[8] This may be explained by the challenging nature of the molecule. The present work employs a theoretical approach wherein cylinder formation of SO_3 is modeled in order to assess the risk of corrosive attack with respect to operational conditions. The model does not apply a predictive fuel spray combustion model including fuel phase changes but treats multiple homogeneous gas zones similar to the procedure suggested by Anderson[9] and used by Andreasen[8] who modeled formation of sulfur oxides in a large low speed diesel engine at a low sulfur content of 0.05 wt %. Treating multiple gas zones is not a crude simplification since SO_3 basically forms only in post flame regions as hot gas products are diluted with air.

The model is formulated in MATLAB and applies the open source software CANTERA[10,11] that is efficiently used to integrate chemical reaction rates, computing general chemical equilibrium and thermodynamic gas properties. With CANTERA thermodynamic properties of gas mixtures and species are expressed through 7 coefficient NASA polynomials.

Background on SO_3 Formation and Applied Reaction Mechanism. Theoretical investigations of SO_3 formation in

Received: November 4, 2012
Revised: January 31, 2013
Published: February 1, 2013

diesel engines is absent in contrast to gas turbines where considerable attention has been found throughout the years.[12−14] Also in standard textbooks[15,16] on the subject of combustion and internal combustion engines formation of sulfur oxides is weakly covered compared to e.g. nitrogen oxides.

Thermodynamic considerations of hydrocarbon/hydrogen flames containing sulfur shows that SO_2 is the principal sulfur containing species in the product gas.[17,18] Experimental results confirm this trend and indicate that SO_2 is equilibrated rapidly near the flame front on a time scale comparable to that of the fuel oxidation reactions.[12,16,18] In a flat flame furnace Headley[19] measured SO_3 concentrations in excess than thermodynamically "allowed" by the overall reaction between SO_2 and O_2. Headley concluded that SO_3 is rather formed from the reaction between SO_2 and atomic O and that a strict thermodynamic criterion is not appropriate to describe SO_3 formation at high temperatures. The statement is supported by other researchers,[2,20] and rather simple SO_3 mechanisms involving SO_2, O, and H are provided in refs 16 and 17.

Focus on atmospheric sulfur chemistry has provided theoretical and experimental work on thermochemistry and reactions of H−S−O complexes.[21−25] Based on experimental results from the literature as well as theoretical tools Glarborg[26] evaluated thermodynamic properties and analyzed reaction systems involving H−S−O complexes. A revised detailed reaction mechanism comprising a sulfur subset, a H_2/O_2 subset, and a CO/CO_2 subset is formulated[27] and applied in this work. The mechanism covers 35 species and the sulfur subset alone contains 96 elementary reactions. On oxidation of SO_2 to SO_3 the mechanism is validated against a range of high temperature experimental data based on various reactor experiments. Additionally a single reaction describing gaseous H_2SO_4 formation is applied in the present work. Published data on H_2SO_4 formation is limited, yet kinetic rate coefficients of a reaction between SO_3 and H_2O are suggested.[28] The rates are investigated in a low pressure environment far from combustion conditions. Nevertheless the rate is fast and considered rational in describing gaseous H_2SO_4 formation.

In low speed diesel engines emissions of nitrogen oxides are primarily represented by NO and reactions involving NO_2 are negligible.[29] Correspondingly N_2O formation is ignored in the present study as it is more appropriate in a lean premixed combustion like e.g. gas turbines.[15] Hence, the extended Zeldovich mechanism[30] is applied in the present work to simulate NO formation.

EXPERIMENTAL SECTION

A large test engine from MAN Diesel & Turbo is used to generate experimental data needed to calibrate the multizone model. Four steady state experiments are conducted at 100, 75, 50 and 25% engine load at engine speeds of 123, 112, 98, and 78 rpm respectively. The speed decreases with the load according to a simulated propeller curve.[8] General engine specifications are presented in Table 1.

THEORETICAL MODEL

To reduce model complexity and computational time a number of important assumptions are introduced. However from the author's point of view these simplifications will not alter the general depiction of SO_3 formation.

- The fuel is treated as n-dodecane ($C_{12}H_{26}$) including nonbonded elemental sulfur.
- The air is treated as dry air with 79% N_2 and 21% O_2.

Table 1. Test Engine Specifications

parameter	remarks
engine type	4T50ME-X
number of cylinders	4
bore/stroke/connecting rod	500 mm/2200 mm/2885 mm
MCR[a] speed	123 rpm
MCR power	7050 kW
MEP[b] at MCR	20 bar
turbocharger	MAN TCA55-VTA

[a]Maximum continuous rating. [b]Mean effective pressure.

- The fraction of injected fuel is directly reflected by the fuel burn fraction.
- Gas mixtures obey ideal gas conditions.
- Gas properties are updated every crank angle.
- The gas pressure in the cylinder is uniform.
- Blow by affects are neglected.
- Only cylinder bore, piston position, and compression ratio is used to define cylinder geometry.

Single-Zone Model. Initially a homogeneous cylinder gas (single zone) is considered in order to evaluate the burned fuel fraction of each crank angle during combustion. For this purpose the first law of thermodynamics of an ideal gas mixture in a closed system (1) is applied. In this form a measured cylinder pressure trace can be applied to determine the heat release of combustion. A closed system approximation is not entirely true since the fuel is injected directly into the combustion chamber. However the consequence of neglecting injection effects in the overall energy balance is typically small compared to the inaccuracies associated with heat transfer correlations[31] as provided in the literature of combustion engines. The correlations typically involve empirical constants that need to be calibrated for the specific engine under consideration. Otherwise the correlations only provide qualitatively predictions in particular during combustion. Nevertheless the well-known Woschni correlation is applied in this work using constants suggested by Ferguson.[32]

$$\frac{dQ_{net}}{d\theta} = \frac{\gamma}{\gamma - 1} p \frac{dV}{d\theta} + \frac{1}{\gamma - 1} V \frac{dp}{d\theta} \tag{1}$$

$$\dot{Q}_f = \frac{dQ_f}{d\theta} = \frac{dQ_{net}}{d\theta} + \frac{dQ_{HT}}{d\theta} \tag{2}$$

The liberated heat from the fuel $\dot{Q}_f$ in 2 is the sum of an effective net heat release plus the heat transfer/loss. In 3 $\dot{Q}_f$ is integrated in order to determine the trace of the fuel burn rate/burn fraction $x_b(\theta)$.

$$x_b(\theta) = \frac{\int_{\theta_{start}}^{\theta+\Delta\theta} \dot{Q}_f \cdot d\theta - \int_{\theta_{start}}^{\theta} \dot{Q}_f \cdot d\theta}{\int_{\theta} \dot{Q}_f \cdot d\theta} \tag{3}$$

The trapped cylinder gas at the time where compression starts is a mixture of fresh air and residual gas products from the previous engine cycle. Still the mixture temperature and the share of the two gas types are unknown. The share of residual gas X_{res} depends on the quality of the prior gas exchange where most of the combustion products are replaced by fresh air. X_{res} is calculated using Blair's empirical correlation[33] which is the result of numerous cylinder gas exchange/scavenging experiments with different porting configurations.

The mass of air and residual gas is calculated from eqs 4 and 5 respectively where the inlet air temperature is provided experimentally. In contrast the temperature of the residual gas is not known in advance but is calculated through an iterative engine cycle procedure. Following the mixture temperature at the start of compression is calculated assuming that the enthalpy of the two gas types is conserved. In the single-zone approach gas properties are updated every crank angle assuming that the cylinder gas is in a state of general chemical equilibrium if the temperature is above 1200 K. The gas temperature (during compression and expansion) is linked to the measured cylinder pressure. Below 1200 K the gas composition is assumed to be frozen.

$$m_{Air} = \frac{p_{EVC}}{R_{Air} \cdot T_{Air}} V_{EVC} \cdot (1 - X_{res}) \tag{4}$$

$$m_{res} = \frac{p_{EVC}}{R_{res} \cdot T_{res}} V_{EVC} \cdot X_{res} \tag{5}$$

Multizone Model. Traces of experimental cylinder pressure with respect to engine load are presented in Figure 1 next to

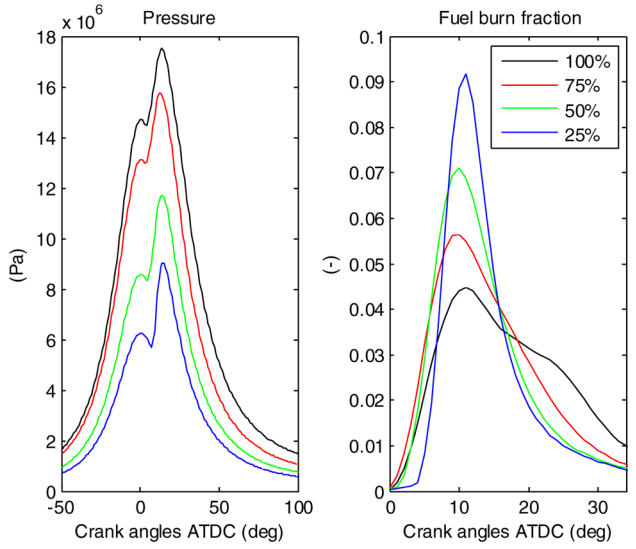

Figure 1. Traces of experimental cylinder pressure and fuel burn fraction with respect to engine load.

the traces of the burned fuel fraction as predicted by the single-zone model. The fuel starts to burn just after TDC, but the shape of the combustion depends on the engine load. For instance the combustion duration is reduced at lower loads because less fuel is added per cycle. For a given load the multizone model is coupled to the single-zone model in the sense that it applies the cylinder pressure trace and the corresponding fuel burn trace. Another adopted feature is the gas composition and temperature at the time where the fuel starts to burn. However in contrast to the single-zone approach multiple gas zones are treated from this instant and until EVO.

Burned Zones and Gas Mixing. A compression ignited diesel combustion process with direct fuel injection is basically diffusion controlled with a stoichiometric flame zone enclosing a decomposing fuel spray.[34] Nonetheless the complex nature of the spray and flame is not modeled. Instead the model seeks to reproduce high temperatures close to the flame by separating the overall fuel mass in multiple burned gas zones. At each crank angle during fuel combustion a new burned zone is created where the burning fuel fraction is mixed stoichiometrically with air and residual gas from the fresh gas zone. The local flame temperature is calculated assuming that the product species attain general chemical equilibrium. This implies that chemical reactions between the fuel and fresh gas proceed very fast which is a common assumption[32] due to the high flame temperature of more than 2500 K. After combustion a burned zone is diluted with fresh gas (air + residual gas) every crank angle at a defined rate as described below. No more fuel is added to a burned zone, and no gas exchange is considered between burned zones either. Consequently a burned zone grows leaner throughout the expansion stroke.

The rate at which fresh gas is mixed into a burned zone per crank angle is assumed to be constant, but if the local excess air ratio should exceed the overall excess air ratio, then no more gas is added to the zone. By applying the overall excess air ratio the integrated mass of air m_{max} that may potentially mix into each zone until EVO is calculated and used to express the mixing rate for each zone eq 6 where N is the number of crank angles between EVO and the point where combustion starts. The mixing rate is a rough simplification of the complex nature of air entrainment into the flame and combustion products. Therefore an adjustable mix gain factor β is introduced with the aim of investigating mixing sensitivity, and moreover β can be calibrated in order to meet experimental results of NO. In addition, since the share of fresh gas reduces as more fuel is burned, the mixing rate of subsequent zones is assumed to decrease accordingly. This is done by introducing the relative fresh gas volume $\bar{V}$ at the angle where a given burned zone is created.

$$\dot{m}_{mix} = \beta \frac{m_{\max}}{N} \bar{V} \tag{6}$$

Burned Zone Temperature Trace. During cylinder expansion the burned zones cools every crank angle due to gas mixing and expansion. The cooling is assumed to take place in two steps. First the burned zones mix with colder fresh gas at constant pressure. The mixing provides an intermediate temperature T^* that is calculated by conserving the total enthalpy. The gas mixture of a burned zone is assumed to be in the state of general chemical equilibrium if the resulting temperature is more than 1200 K. Otherwise the mixture chemistry is assumed frozen. Second the ideal gas law on a differential form 7 is applied to calculate the temperature drop due to expansion, and the updated temperature of the burned zone is determined using Euler integration 8.

$$V\frac{dp}{d\theta} + p\frac{dV}{d\theta} = mR\frac{dT}{d\theta} \tag{7}$$

$$T(\theta + \Delta\theta) \approx T^*(\theta) + \frac{dT}{d\theta} \cdot \Delta\theta \tag{8}$$

Modeled temperature and excess air ratio traces of selected burned zones are illustrated in Figure 2 for two different mixing rates represented by a β-value of 0.5 and 1. The leftmost point on the traces represents a flame condition where the temperature is around 2700 K and the mixture is stoichiometric i.e. $\lambda = 1$. Increasing β means that more fresh gas will mix into the burned zones. This provides higher local excess air ratios throughout the expansion stroke but lowers the local temperatures in turn as seen in the figure. By definition, if $\beta = 1$, then the first created burned zone will attain the global

dx.doi.org/10.1021/ef301793a | Energy Fuels 2013, 27, 1652−1660

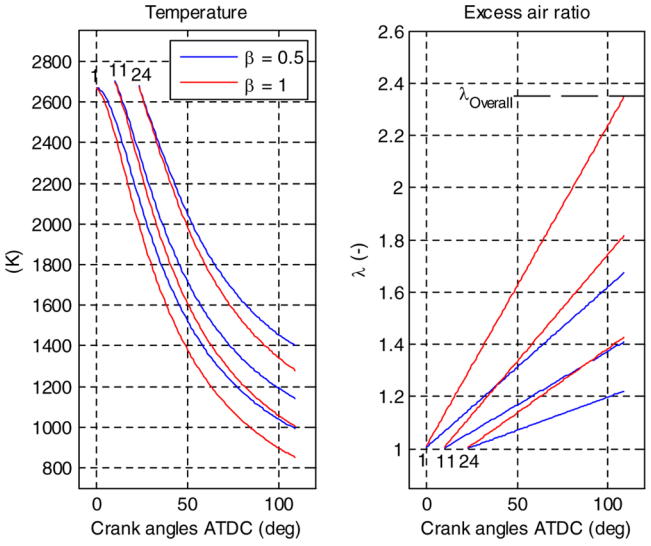

Figure 2. Temperature and excess air ratio traces of selected burned zones at 50% engine load and two different mixing rates represented by β. Numbers in the figure refer to burned zones.

excess air ratio exactly at EVO. Additionally the hindered mixing rates of subsequent zones by introducing $\overline{V}$ in eq 6 are demonstrated by the ever reducing gradients of the local excess air ratio traces.

KINETIC MODEL

Suggested high temperature key reactions including rate coefficients applied to model SO_3 formation are listed in Table 2 with reaction numbers referring to the full sulfur reaction mechanism.[27] Formation of SO_3 proceeds from a direct oxidation of SO_2 involving $HOSO_2$ as an intermediate.

Table 2. Key Reactions Including Rate Coefficients Describing High Temperature Oxidation of SO_2 to SO_3[27c]

reaction no.	reaction	A	n	E/R
86	$SO_2 + O(+M) \leftrightarrow SO_3(+M)$[a]	3.7E11	0.00	850
	low-pressure limit	2.4E27	−3.60	2610
	troe parameters 0.442, 316, 7442			
	low pressure limit (N2)	2.9E27	−3.58	2620
	troe parameters (N2) 0.43, 371, 7442			
88	$SO_2 + OH(+M) \leftrightarrow HOSO_2(+M)$[b]	5.7E12	−0.27	0
	low-pressure limit	1.7E27	−4.09	0
	troe parameters 0.10, 1×10^{-30}, 1E30			
89	$SO_2 + SO_2 \leftrightarrow SO_3 + SO$	5.0E07	2.00	37750
90	$SO_3 + H \leftrightarrow SO_2 + OH$	8.4E09	1.22	1670
92	$SO_3 + O \leftrightarrow SO_2 + O_2$	2.8E04	2.57	14700
93	$SO_3 + OH \leftrightarrow SO_2 + HO_2$	4.8E04	2.46	13700
130	$HOSO_2 \leftrightarrow SO_3 + H$	1.4E18	−2.91	27630
131	$HOSO_2 + H \leftrightarrow SO_2 + H_2O$	1.0E12	0.00	0
132	$HOSO_2 + O \leftrightarrow SO_3 + OH$	5.0E12	0.00	0
133	$HOSO_2 + OH \leftrightarrow SO_3 + H_2O$	1.0E12	0.00	0
134	$HOSO_2 + O_2 \leftrightarrow HO_2 + SO_3$	7.8E11	0.00	330

[a]Enhanced third-body coefficients: N_2 = 0, SO_2 = 10, H_2O = 10. [b]Enhanced third-body coefficients: N_2 = 1, SO_2 = 5, H_2O = 5. [c]Arrhenius parameters are in cal, cm, mol, s, and K for $k = AT^n \exp(-E/RT)$.

Oxidation with O_2 is hampered compared to atomic O or OH due to a large energy barrier. The full sulfur mechanism does not include H_2SO_4 reactions. Hence in the present work the gaseous formation of H_2SO_4 is modeled from a single reaction between SO_3 and H_2O with rate coefficients suggested by ref 28 and listed in Table 3 together with the extended Zeldovich

Table 3. NO and H_2SO_4 Reactions Including Rate Coefficients[a]

reaction	A	n	E/R
$N + NO \leftrightarrow N_2 + O$	2.7E13	0	179
$N + O_2 \leftrightarrow NO + O$	9.0E09	1	3270
$N + OH \leftrightarrow NO + H$	3.36E13	0	194
$SO_3 + H_2O \leftrightarrow H_2SO_4$	7.23E08	0	0

[a]Arrhenius parameters in cal, cm, mol, s, and K for $k = AT^n \exp(-E/RT)$.

mechanism applied to model NO formation. NO rate coefficients are obtained from the Zeldovich route of the GRI-MECH 3.0 mechanism.[35] The Zeldovich mechanism involves atomic O and OH radicals in competition with SO_3 formation.

MODELING CHEMICAL REACTIONS

The temperature of the fresh gas zone (air and residual gas) increases as a result of compression; yet the peak temperature near TDC is typically not more than 1200 K, and therefore the fresh gas chemistry is assumed frozen throughout the cycle. In contrast the initial gas composition of the burned zones is described by general chemical equilibrium. Subsequently fresh gas mixes into the burned zones every crank angle whereby chemical reactions takes place. The gas species that are mixed into a burned zone is governed by the fresh gas composition and the mixing rate, see eq 6. The composition of a burned zone is updated every crank angle assuming instant and frozen fresh gas mixing before the composition is integrated adiabatically at constant volume where the local temperature and overall pressure is used as input. The integrated burned zone composition is passed to the succeeding time step where the procedure is repeated until the point where the exhaust valve opens.

MODEL CALIBRATION

Formation of SO_3 is very sensitive to the rate at which fresh gas mixes into the burned zones as illustrated in Figure 3. The two subplots present traces of overall concentrations of modeled SO_3 and NO during cylinder expansion at fixed engine load and fuel sulfur content but at different mixing rates represented by β. Moreover the NO plot shows the experimental NO concentration in the trapped cylinder gas exactly at EVO which is used to calibrate the model at the present load.

The rate of SO_3 increases significantly with β, and the final concentration is more or less doubled if $\beta = 2$ compared to $\beta = 0.5$. Moreover SO_3 is not really formed if no fresh gas is assumed to mix with the burned zones i.e. $\beta = 0$. Even though NO formation is very fast compared to SO_3 the response due to mixing is quite similar for the two species as seen in the figure.

In order to calibrate the multizone model and thereby simulate realistic concentrations of SO_3 a reasonable mixing rate is proposed by tuning β at each engine load in order to meet respective experimental NO concentrations. In the two stroke engine a part of the supplied fresh air bypasses the

dx.doi.org/10.1021/ef301793a | Energy Fuels 2013, 27, 1652−1660

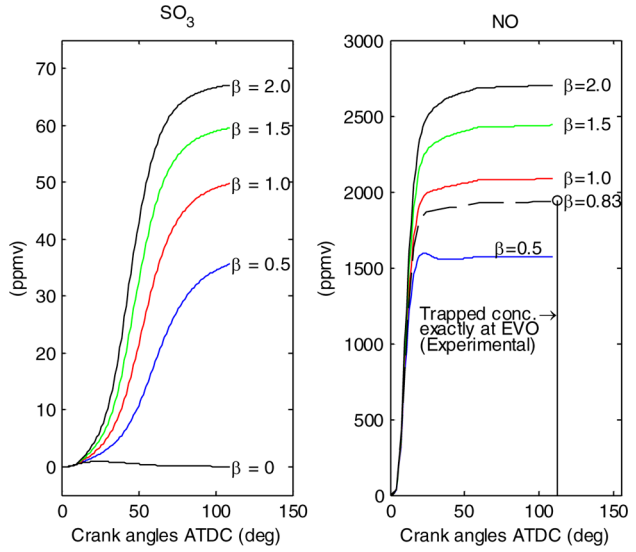

Figure 3. Gas mixing sensitivity (illustrated by β) of SO_3 and NO modeled at 50% engine load and 4.5 wt % fuel sulfur. The NO plot includes an experimental concentration exactly at EVO.

cylinder during the scavenging process and dilutes the outgoing/replaced exhaust gases. This means that the overall NO concentration of the cylinder gas exactly at EVO (when the exhaust valve is still closed) is higher than the measured exhaust pipe concentration presented in Table 4. By compensating for

Table 4. Measured Exhaust Pipe NO Concentrations and Calibrated β Values with Respect to Operational Conditions

engine load (%)	rpm	NO_{exh} (ppmv)	β (-)
25	78	1320	0.89
50	98	1236	0.83
75	112	1266	0.59
100	123	1119	0.41

the gas dilution the trapped experimental NO concentration exactly at EVO is determined and shown for the 50% load case in Figure 3 (1965 ppmv). Following the model is calibrated by tuning the β-value in order to reproduce this value as seen in Figure 3 where the calibrated β-value is found to be 0.83.

Calibrated β-values for the different engine loads are listed in Table 4. At all loads β is less than 1. Computationally this means that none of the burned zones will attain the overall excess air ratio during cylinder expansion. β also reflects the engine speed inversely as seen in the table. At 100% load the mixing is found to be rather low due to the increased engine speed leaving less time for gas mixing.

COMPUTATIONAL RESULTS

The sulfur species of relevance in the burned gases are SO_2 and SO_3 beside a very small fraction of H_2SO_4. To illustrate SO_3 formation expression 9 is used where ε practically describes the competition between SO_2 and SO_3 formation.

$$\varepsilon = \frac{[SO_3]}{[SO_3] + [SO_2] + [H_2SO_4]} \quad (9)$$

Kinetically determined SO_3 formation in burned zones with respect to the crank angle from the point of creation and until EVO at 50% engine load and 4.5 wt % fuel sulfur is illustrated in Figure 4. The leftmost point on each trace represents a condition very close to the stoichiometric flame zone where the

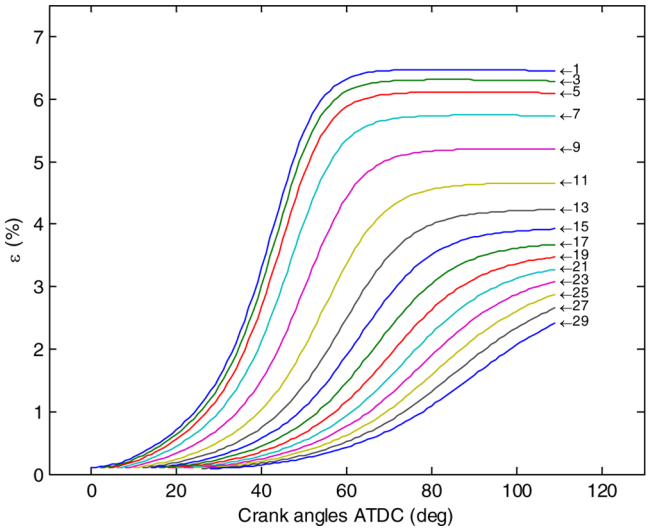

Figure 4. Formation of SO_3 in burned zones at 50% engine load and 4.5 wt % fuel sulfur. Numbers in figure refer to burned zones.

sulfur oxides are more or less represented by SO_2 only. A little after the rate of SO_3 in the first 12−15 zones increases rapidly as the gas expands and mixes with fresh gas. However the rapid formation is also followed by a rapid slow down, and at some point the SO_3 formation stagnates. Yet locally the fraction of SO_3 may be more than 6%. In subsequent zones the fraction is considerably lower, and their contribution to the overall SO_3 output is small as they typically hold a small share of the injected fuel sulfur.

In Figure 5 the former ε-traces of the burned zones are illustrated with respect to temperature together with the theoretical traces of ε as prescribed by general chemical equilibrium. Although SO_3 is rapidly equilibrated at the highest temperatures, SO_2 is the principal sulfur oxide close to the flame, and SO_3 formation is very limited above 2000 K. Thermodynamically SO_3 is increasingly favored as the temper-

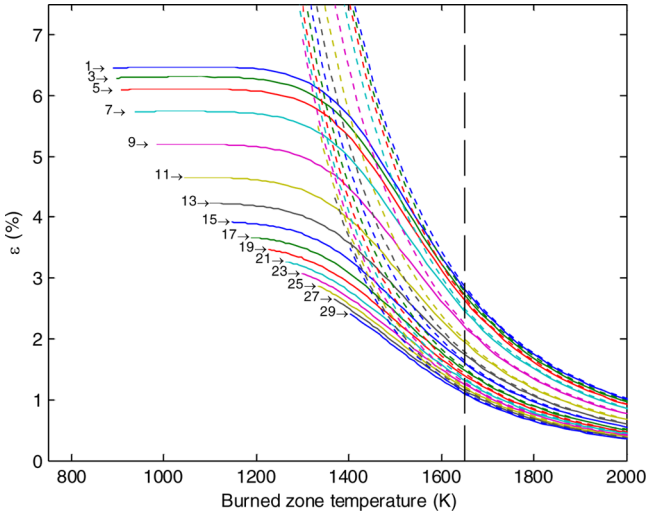

Figure 5. Formation of SO_3 in burned zones versus temperature at 50% engine load and 4.5 wt % fuel sulfur. Dashed traces represent general chemical equilibrium and trace numbers refer to burned zones.

dx.doi.org/10.1021/ef301793a | Energy Fuels 2013, 27, 1652−1660

ature reduces during cylinder expansion. However at around 1650 K the SO_3 kinetics is too slow to keep up with the theoretical growth. The primary SO_3 formation takes place within the temperature range from 2000 K to 1300 K, and the governing reactions freeze close to the latter.

According to the present model gaseous formation of H_2SO_4 in high temperature burned zones is very limited and results in an overall concentration of less than 1 ppmv at EVO. However H_2SO_4 is thermodynamically favored over SO_3 if the hot gases are cooled sufficiently for instance upon contact with the cooled liner surface (this aspect is not covered by the model though). Moreover, SO_3 and H_2SO_4 concentrations have been used interchangeably for acid dew point calculations[36,37] which is rational due to the fast $H_2O + SO_3 \leftrightarrow H_2SO_4$ reaction as indicated in Table 3. Consequently a sensible depiction of gaseous H_2SO_4 formation is illustrated by the theoretical curves in Figure 6. The curves represent the fractional conversion of

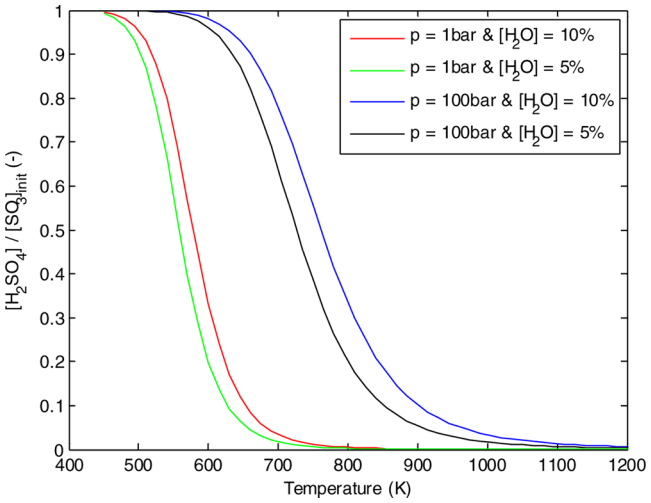

Figure 6. Fraction of initial SO_3 converted to gaseous H_2SO_4 with respect to temperature, overall pressure, and H_2O vapor concentration.

initial SO_3 to gaseous H_2SO_4 at general chemical equilibrium with respect to temperature, overall pressure, and H_2O vapor concentration. As shown the H_2SO_4 onset is moved toward higher temperatures if the pressure and or the concentration of H_2O increases. In any case most of the SO_3 is converted to H_2SO_4 if the hot gases are cooled for instance to 550 K. The liner temperature is typically around 475 K,[38] and a considerable amount of H_2SO_4 may form at the gas-to-liner interface in practice. Concentrated acid or more important diluted acid in water is known to condense on the liner surface providing that the temperature is lower than the dew point temperature. The revised SHELL acid dew point curves[38] indicates that the dew point of a gaseous mixture of H_2SO_4 and H_2O can exceed 475 K at the current sulfur levels and cylinder gas conditions. However, if the surface temperature is still above the dew point of pure water the condensed acid is highly concentrated but quite harmless compared to a condition where pure water also condenses. Such a condition results in a much more aggressive/corrosive solution.[39]

The traces of ε in Figure 7 illustrate the overall formation of SO_3 from TDC until EVO at different engine loads and sulfur contents. In all cases except one any possible surface formation of H_2SO_4 and condensation is omitted. This implies that ε at EVO is the same as when combustion starts in the subsequent

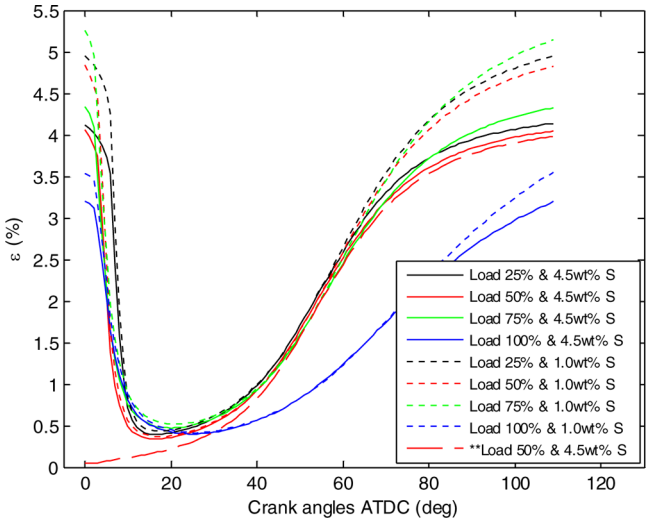

Figure 7. Overall formation of SO_3 with respect to engine load and fuel sulfur content. (**no SO_3 or H_2SO_4 present in residual gas.)

cycle. Just after TDC a sudden drop of ε is observed in the figure and demonstrates formation of SO_2, while SO_3 from the fresh gas is rapidly converted to SO_2 as it is mixed into the high temperature burned zones. During the second half of fuel combustion ε reaches a minimum at around 0.5% but then starts to increase considerably demonstrating formation of SO_3. Depending on the load the final share of SO_3 at EVO is in the order of 3.5−5.2% and 3.2−4.3% at 1 wt % and 4.5 wt % fuel sulfur respectively. This shows that the fraction of SO_3 increases inversely with the fuel sulfur content in agreement with experimental results.[1] Generally ε increases slightly with the engine load (providing that the speed is unchanged) which seems reasonable due to elevated pressures providing a higher degree of SO_2 oxidation in the latter part of the expansion stroke. Especially at 100% load the fresh gas mixing is comparably low as indicated by the small β-value in Table 4 and explained by the elevated engine speed leaving less time for mixing and chemical reactions. As a consequence, SO_3 formation is hampered and ε deviates from the general trend.

If it is assumed that no SO_3 or H_2SO_4 is present in the residual gas when combustion starts a slightly different trace of ε develops as also demonstrated in Figure 7 in the case of 50% engine load and 4.5 wt % sulfur. In contrast the trace of ε now starts close to zero, but soon after the trace is almost identical to the former case at the equivalent conditions. In the present case ε is a bit lower at EVO though since the fresh gas holds no SO_3.

Model results of overall concentrations of SO_2 and SO_3 from TDC and until EVO are presented in Figure 8 with respect to engine load and fuel sulfur content. Irrespective of the load SO_2 forms rapidly just after TDC and seeks toward a more or less fixed concentration. At 4.5 wt % sulfur the final concentration is between 1000−1200 ppmv depending on the engine load. Changing from 4.5 wt % to 1 wt % fuel sulfur will reduce the SO_2 concentration proportionally. SO_3 formation is slow compared to SO_2 and the onset is about 20−30 crank angles past TDC, yet the majority is formed within the first 75 crank angles. Final differences in SO_3 concentrations are fairly small with respect to engine load. For instance at 4.5 wt % sulfur the range is between 38−47 ppmv, and at 1 wt % the concentration is between 9−12 ppmv.

dx.doi.org/10.1021/ef301793a | Energy Fuels 2013, 27, 1652−1660

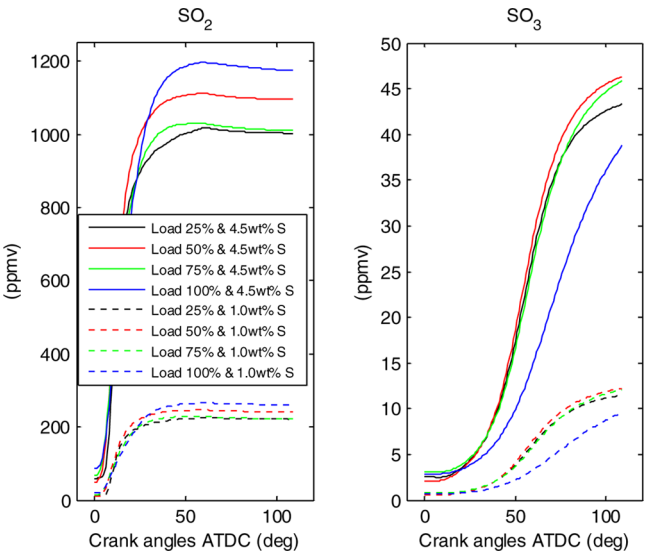

Figure 8. Overall concentrations of SO_2 and SO_3 with respect to engine load and fuel sulfur content.

RELATIVE RISK OF LINER CORROSION

In practice the fuel is injected into the combustion chamber through a multihole injector in the top of the cylinder and above the liner. Unfortunately the present 0D multizone approach cannot locate the burned zones throughout combustion and expansion. Yet the local concentration of SO_3 (mol/m^3) in the burned zones with respect to time (i.e., the number of crank angles that has passed after a given zone is created) is depicted in Figure 9. The traces indicate that the local concentration typically peaks at about 50−60 crank angles past creation and then reduces rapidly due to expansion and mixing with fresh gas.

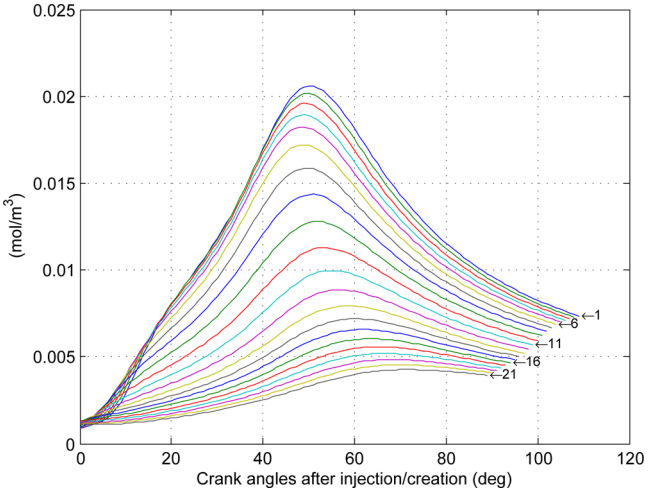

Figure 9. SO_3 concentration in burned zones during cylinder expansion at 50% engine load and 4.5 wt % fuel sulfur. Numbers in figure refer to burned zones.

The rate of acid condensation on an exposed surface increases with the partial pressure of H_2SO_4 in the gas phase.[5,40] Combined with the former proposal regarding surface H_2SO_4 formation the figure can be used to depict the risk of corrosive attack along the cylinder liner. It appears that the risk is highest within the first 60 crank angles after TDC (i.e.in the upper third of the liner) providing that the surface temperature is sufficiently low. The results are consistent with practical experience of large two stroke engines where corrosive attack is pronounced in the top of the liner around the ring pack position at TDC.

REDUCING THE SULFUR SUBSET

Basically SO_3 forms only in post flame regions where the excess air ratio is above 1. Still the full sulfur subset contains 96 elementary reactions, and many of these are not relevant in the high pressure environment of a large low speed diesel engine. In combination with CANTERA the present model is well suited to reduce the number of chemical reactions as well as the number of sulfur species in order to reduce the computational time. To do this the net formation rate of each elementary reaction of each burned zone is investigated throughout the expansion stroke wherein the zones meet high pressure and temperature gradients and mix with fresh gas. Moreover the sulfur chemistry is reduced by keeping the H_2/O_2 and the CO/CO_2 subset unchanged. Based on the investigation a largely reduced sulfur subset is suggested comprising only 6 of the elementary reactions in Table 2 but includes reaction number 77 from the full sulfur subset. The revised subset comprises reaction numbers 86, 88, 89, 90, 93, 134, and 77 with rate coefficients as listed in Table 5. In addition the number of sulfur species is reduced from 14 to 4.

Table 5. Elementary Sulfur Reaction of the Revised Sulfur Subset[a]

reaction no.	reaction	A	n	E/R
77	$SO + O_2 \leftrightarrow SO_2 + O$	7.6E3	2.37	2970

[a]Arrhenius parameters in cal, cm, mol, s, and K for $k = AT^n \exp(-E/RT)$.

The revised sulfur subset is compared with the full subset in Figure 10 at different mixing rates expressed by β that is varied between 0.1 and 1.5. The traces in the figure illustrate overall SO_3 formation (expressed by ε) from TDC and until EVO. As

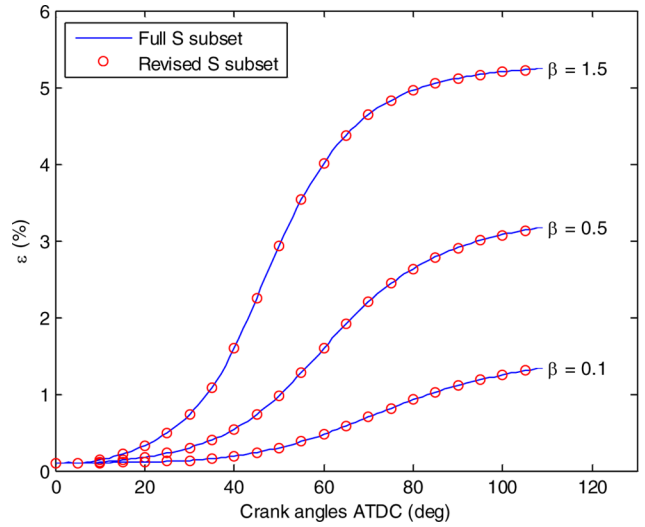

Figure 10. Overall SO_3 formation modeled with a full and a revised sulfur subset at different mixing rates (β) at 50% engine load and 4.5 wt % fuel sulfur.

dx.doi.org/10.1021/ef301793a | Energy Fuels 2013, 27, 1652−1660

shown no accuracy is lost in the SO_3 to SO_2 ratio with the revised subset.

CONCLUSIONS

In the present work gaseous formation of sulfur oxides in a large low speed two-stroke diesel engine is modeled using a 0D multizone approach in combination with a detailed reaction mechanism where fuel is modeled as n-dodecane with nonbonded elemental sulfur. Computationally the fuel is separated in multiple burned gas zones to address the effect of high flame temperatures and local variations of fresh gas mixing. Results demonstrate that the rate of mixing is a very sensitive parameter regarding SO_3 formation. High mixing rates result in more SO_3 in a similar fashion as NO. An adjustable mixing rate is suggested and calibrated in order to meet experimental results of NO. The model simulates realistic results of SO_3 providing confidence with the applied reaction mechanism and model assumptions. In addition the present model is used in combination with CANTERA to reduce the sulfur subset of the overall reaction mechanism from 96 to 7 elementary reactions without compromising the accuracy of the SO_3 to SO_2 fraction in the burned gases. Moreover the number of required sulfur species is reduced from 14 to 4.

Due to thermodynamic restrictions SO_3 is weakly present at the highest temperatures close to the diesel flame. However SO_3 is increasingly favored as the gas temperature reduces during cylinder expansion. Basically all of the SO_3 is formed locally in the temperature range from about 2000 K and down to 1300 K. Moreover down to about 1650 K SO_3 is well described by general chemical equilibrium. The governing SO_3 reactions are frozen below 1300 K and down to about 800−1000 K where gaseous/corrosive H_2SO_4 is preferred from a fast reaction between SO_3 and H_2O. At about 50−60 crank angles past TDC the SO_3/H_2SO_4 concentration peaks in accordance with practical experience that shows the highest rates of surface corrosion in the upper part of the cylinder liner.

Overall sulfur to SO_3 conversion increases slightly with the engine load providing that the engine speed is similar but increases slightly inversely with the fuel sulfur content. In general the conversion is on the order of 3−5%, and the remainder is converted to SO_2

AUTHOR INFORMATION

Corresponding Author

*E-mail: rco@mek.dtu.dk.

Notes

The authors declare no competing financial interest.

NOMENCLATURE

h = enthalpy kJ/kg
m = mass kg
$\dot{m}_{mix}$ = fresh gas mixing kg/°CA
p = pressure Pa
Q_f = fuel heat kJ
Q_{HT} = heat transfer kJ
Q_{net} = net heat release kJ
R = gas constant J/mol K
T = temperature K
V = volume m^3
X_{res} = residual gas fraction at EVC m^3/m^3
γ = specific heat ratio -
λ = excess air ratio -
θ = crank angle position °C
θ_{start} = start of combustion °C
$\Delta\theta$ = computational step °C

ABBREVATIONS

ATDC = after top dead center
CA = crank angles
EVC = exhaust valve closing
EVO = exhaust valve opening
MCR = maximum continuous rating
MEP = mean effective pressure
res = residual gas
TDC = top dead center

REFERENCES

(1) Engel, P. K.; Thompson, R. E.; Silvestrinin, R. Corrosion and Fouling Potential in Diesel Exhausts. *Mech. Eng.* **1979**, *101*, 598−606.
(2) Dooley, A.; Whittingham, G. The Oxidation of Sulphur Dioxide in Gas Flames. *Trans. Faraday Soc.* **1946**, *42*, 354−366.
(3) Schramm, J.; Henningsen, S.; Sorenson, S. C. Modelling of Corrosion of Cylinder Liner in Diesel Engines Caused by Sulphur in the Diesel Fuel. *SAE Paper* **1994**, 940818.
(4) Jackson, P. J.; Hilton, D. A.; Buddery, J. H. Continuous Measurement of Sulphuric Acid Vapour in Combustion Gases using a Portable Automatic Monitor. *J. Inst. Energy* **1981**, *54*, 124−135.
(5) Land, T. Theory of Acid Deposition and its Application to the Dew-Point Meter. *J. Inst. Fuel* **1977**, *50*, 68−75.
(6) Boons, M.; Brand, R. Lubrication Challenges for Distillate Fuel Operated Two-Stroke Engines. In *26 CIMAC World Congress*; CIMAC: Bergen, 2010.
(7) Welsch, M. *Considerations for using low-sulphur fuel*; Wärtsila Corporation: 2002.
(8) Andreasen, A.; Mayer, S. Modeling of the oxidation of fuel sulfur in low speed two-stroke Diesel engines. In *26th CIMAC World Congress*; Bergen, 2010.
(9) Andersson, M.; Johansson, B.; Hultqvist, A. A Real-Time NOx Model for Conventional and Partially Premixed Diesel Combustion. *SAE Paper* **2006**, *2006-01-0195*.
(10) Goodwin, D. G. *Defining phases and interphases - Cantera 1.5*; Tech. rep.; California Inst. of Technology: 2003.
(11) Goodwin, D. G. *Cantera C++ users guide*; California Inst. of Technology: 2002.
(12) Hunter, S. C. Formation of SO3 in Gas Turbines. *J. Eng. Power* **1982**, *104*, 44−50.
(13) Lebedev, A. B.; Secundov, A. N.; Starik, A. M.; Titova, N. S.; Schepin, A. M. Modeling Study of Gas-Turbine Combustor Emission. *Proc. Combust. Inst.* **2009**, *32*, 2941−2947.
(14) Moniruzzaman, C. G.; Yu, F. A 0D Aircraft Engine Emission Model with Detailed Chemistry and Soot Microphysics. *Combust. Flame* **2012**, *159*, 1670−1686.
(15) Turns, S. R. *An introduction to combustion/concepts and applications*; McGraw-Hill: New York, 2012.
(16) In *Fossil fuel combustion/A source book*; Bartok, W., Sarofim, A., Eds.;Wiley: New York, 1991.
(17) Cullis, C. F.; Mulcahy, M. F. R. The Kinetics of Combustion of Gaseous Sulphur Compounds. *Combust. Flame* **1972**, *18*, 225−292.
(18) Johnson, G. M.; Matthews, C. J.; Smith, M. Y.; Williams, D. J. Distribution of Sulfur Species in the Burnt Gas of Fuel-Rich Propane-Air Flames. *Combust. Flame* **1970**, *15*, 211−214.
(19) Hedley, A. B. Sulphur Trioxide in Combustion Gases. *Fuel Soc. J.* **1962**, *13*, 45−54.
(20) Merryman, E. L.; Levy, A. Enhanced SO3 Emissions from Staged Combustion. *Symp. Int. Combust.* **1979**, 727−736.
(21) Gleason, J. F.; Howard, C. J. Temperature Dependence of the Gas-Phase Reaction HOSO2+O2=>HO2+SO3. *J. Phys. Chem.* **1988**, *92*, 3414−3417.

(22) Gleason, J. F.; Sinha, A.; Howard, C. J. Kinetics of the Gas-Phase Reaction HOSO2+O2=>HO2+SO3. *J. Phys. Chem.* **1987**, *91*, 719−724.
(23) Laakso, D.; Smith, C. E.; Goumri, A.; Rocha, J.; Marshall, P. Theoretical Studies of the RSOO, ROSO, RSO(2) and HOOS (R=H, CH(3)) Radicals. *Chem. Phys. Lett.* **1994**, *227*, 377−383.
(24) Goumri, A.; Rocha, J.; Laakso, D.; Smith, C. E.; Marshall, P. Computational Studies of the Potential Energy Surface for O(1 D)+H2S: Characterization of Pathways Involving H2 SO, HOSH, and H2OS. *J. Chem. Phys.* **1994**, *101*, 9405−9411.
(25) Goumri, A.; Laakso, D.; Rocha, J.; Smith, C. E.; Marshall, P. Computational Studies of the Potential Energy Surface for O-(3P)+H2S: Characterization of Transition States and the Enthalpy of Formation of HSO and HOS. *J. Chem. Phys.* **1995**, *102*, 161−169.
(26) Glarborg, P.; Kubel, D.; DamJohansen, K.; Chiang, H.; Bozzelli, J. Impact of SO2 and NO on CO Oxidation under Post-Flame Conditions. *Int. J. Chem. Kinet.* **1996**, *28*, 773−790.
(27) Hindiyarti, L.; Glarborg, P.; Marshall, P. Reactions of SO3 with the O/H Radical Pool under Combustion Conditions. *J. Phys. Chem. A* **2007**, *111*, 3984−3991.
(28) Reiner, T.; Arnold, F. Laboratory Investigations of Gaseous Sulfuric-Acid Formations via SO3+H2O+M=>H2SO4+M: Measurements of the Rate-Constant and Product Identification. *J. Chem. Phys.* **1994**, *101*, 7399−7407.
(29) Zabetta, E. C.; Kilpinen, P. Improved NOx Submodel for in-Cylinder CFD Simulation of Low- and Medium-Speed Compression Ignition Engines. *Energy Fuels* **2001**, *15*, 1425−1433.
(30) Lavoie, G. A.; Heywood, J. B.; Keck, J. C. Experimental and Theoretical study of Nitric Oxide Formation in Internal Combustion Engines. *Combust. Sci. Technol.* **1970**, *1*, 313−26.
(31) Heywood, J. B. *Internal combustion engine fundamentals*; McGraw-Hill: New York, 1988 .
(32) In *Internal combustion engines/applied thermosciences*; Ferguson, C. R., Kirkpatrick, A. T., Eds.; Wiley: New York, 2001.
(33) In *Design and Simulation of Two-Stroke Engines*; Blair, G. P., Ed.; SAE: Warrendale, PA, 1996.
(34) Dec, J. E.; Espey, C. Soot and Fuel Distributions in a D.I. Diesel Engine Via 2-D Imaging. *SAE Paper***1992**, 922307.
(35) Smith, G. P.; Golden, D. M.; Frenklach, M., et al. GRI-Mech 3.0.
(36) McKinley, T. L. Modeling Sulfuric Acid Condensation in Diesel Engine EGR Coolers. *SAE Spec. Publ. Sens. Actuators* **1997**, *1255*, 207−218.
(37) Mueller, P. Influence of Sulphuric Acid on DEW Point Temperature of Flue Gases. *Chem.-Ing.-Tech.* **1959**, *31*, 345−351.
(38) Hengeveld, J.; Schenk, C.; Aabo, K. The Role of Temperature and Pressure in the Wear Process in Low Speed Diesel Engines. *Shell* **2000**.
(39) Teetz, C. Investigation into Reducing Low Temperature Corrosion in Diesel Engines. *VDI Forschungsh.* **1984**, *626*, 13.
(40) van Helden, A. K.; Valentijn, M. C.; van Doorn, H. M. J. Corrosive Wear in Crosshead Diesel Engines. *Tribol. Int.* **1989**, *22*, 189−193.

energy&fuels

Article

pubs.acs.org/EF

Investigating SO_3 Formation from the Combustion of Heavy Fuel Oil in a Four-Stroke Medium-Speed Test Engine

Rasmus Cordtz,[†,*] Jesper Schramm,[†] and Rom Rabe[‡]

[†]Technical University of Denmark, 2800 Kgs, Lyngby, Denmark

[‡]Rostock University, 18059 Rostock, Germany

ABSTRACT: The validation of detailed models, in terms of SO_3 formation in large marine engines operating on sulfur-containing heavy fuel oils (HFOs), relies on experimental work. The requisite is addressed in the present work, where SO_3 is measured in the exhaust gas of an 80 kW medium-speed single-cylinder HFO-fuelled test engine. SO_3 formation is triggered by running the engine at altered operational conditions and speeds within 1050−1500 rpm. The test engine does not represent a large low-speed marine engine; however, the nature of high-temperature SO_3 formation may well be explored with the current engine and serve as reference for further modeling studies. SO_3 is measured using a continuous SO_3 monitor from PENTOL GmbH. The monitor offers online SO_3 readings and short sampling times, in contrast to other extractive methods. The measurement is based on SO_3 capture in isopropanol prior to chemical conversion and indirect detection via light absorption in a photometer. Present results show that SO_3 formation is favored by elevated pressure histories, premixed combustion, and reduced speeds. The fraction of fuel sulfur converted to SO_3 is measured to be on the order of 0.5%−2.4%, corresponding to 4−14 ppmv. SO_3 and NO_x are not comparable, according to thermodynamic considerations, yet both species involve the radical pool and are studied in parallel. Resulting emissions of SO_3 and NO_x in the exhaust gas follow a comparable trend throughout the experiments.

INTRODUCTION

Heavy fuel oil (HFO), which is used for ship propulsion in large, low-speed marine engines, contain sulfur (on the order of 3 wt %, on average). During combustion, the sulfur is rapidly converted to SO_2,[1,2] from which a fraction is further oxidized to SO_3,[3−5] which, at temperatures lower than ∼600 °C, reacts to form gaseous sulfuric acid H_2SO_4 from a fast reaction[6] with H_2O. For a typical exhaust gas, the equilibrium of eq R1 lies well to the right at temperatures of <300 °C.

$$H_2O(g) + SO_3(g) \rightarrow H_2SO_4(g) \quad \text{(R1)}$$

In large marine engines, H_2SO_4 is experienced to condense on internal surfaces such as the cylinder liner and accelerate surface corrosion. The acid dew point temperature is a function of the partial pressures of water vapor and gaseous sulfuric acid.[7,8] Even small concentrations of H_2SO_4 will increase the dew point considerably, compared to that of pure water.[9] Figure 1 illustrates dew point curves representing two gases with 5% or 10% H_2O at 1 atm). Below the dew point temperature, gaseous H_2SO_4 and water vapor condense as a sulfuric acid solution. However, acid and water condense in different proportions, depending on the H_2SO_4/H_2O ratio and the surface temperature, as experienced by the results of Müller[9] and Greenewalt,[10] who provided correlations for the partial pressures of H_2SO_4 and H_2O out of liquid sulfuric acid solutions. The share of water and acid is vital, because it determines the corrosive strength of the condensing acid.[11] In practice, alkali additives are blended in the lube oil of large marine engines to hamper corrosion on liner surfaces but the rate of acid condensation and thus the optimum dosing is linked to engine performance and fuel type. Unfortunately, practical evaluations of acid attack on cylinder liners are not straightforward. Consequently, detailed experimental work on the formation and fate of SO_3 in HFO-fuelled diesel engines is needed to support theoretical models of H_2SO_4 formation, condensation, and corrosion.

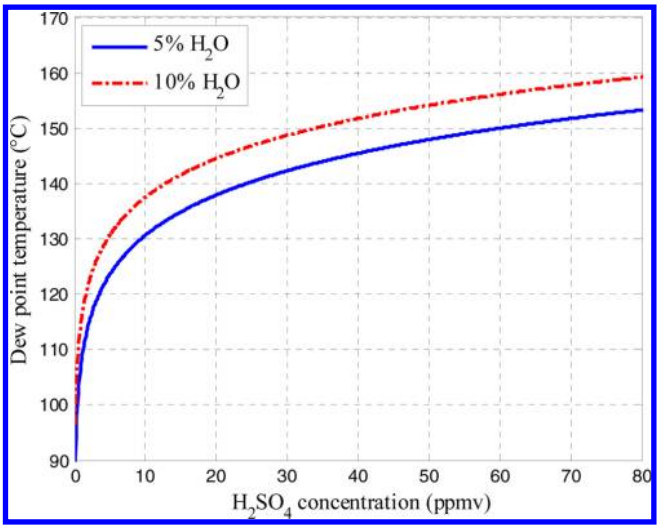

Figure 1. Calculated acid dew point curves[8] at 1 atm versus $[H_2SO_4]$ in 5% and 10% water vapor.

If fuel sulfur associated with particulate mass in the exhaust gas is neglected, and if H_2SO_4 is considered as SO_3, then the

Received: July 29, 2013
Revised: September 12, 2013

   dx.doi.org/10.1021/ef4014696 | *Energy Fuels* XXXX, XXX, XXX−XXX

fraction of fuel sulfur converted to SO_3 in the exhaust gas is expressed by ε in eq 1:

$$\varepsilon = \frac{[SO_3]}{[SO_2] + [SO_3]} \quad (1)$$

Published experimental data on the fraction of sulfur converted to SO_3 in large marine engines is almost absent and relies on theoretical models[6,12] as well as a not-so-accurate "rule of thumb" stating that a few percent is converted to SO_3. The SO_3 measurements by Engel[13] seem to be the only peer-reviewed results of SO_3 formation in diesel engines where SO_3 was measured in the exhaust gas from heavy duty diesel engines. Engel reported that ∼1%−8% of the fuel sulfur was converted to SO_3, depending on the fuel type and operational conditions. Still, it remains to be reported how the SO_3 fraction changes with operational conditions such as engine speed, pressure history, and fuel−air ratio that will serve as useful information in the case of model validations. To meet this, a series of SO_3 measurements is conducted in the exhaust gas produced by an 80-kW single-cylinder test engine with a rated speed of 1500 rpm. The engine operates on HFO and measurements are carried out with two test fuels with comparable sulfur contents of 1.6 wt % and 2.24 wt %. The measurements cover a range from low to high load under steady-state conditions, wherein injection timing, engine speed, and air−fuel ratio is varied to alter the combustion history that is examined via a pressure transducer in order to analyze the rate of heat release. Adjusting the fuel injection timing alters the cylinder pressure history and affects NO_x formation.[14] More specifically, NO_x formation has been shown to scale with the maximum cylinder pressure in diesel engines.[15] Both thermal NO_x and high-temperature SO_3 formation involves the radical pool[3,16] and their response (in the exhaust gas) are examined in parallel, relative to the maximum cylinder pressure. The radical pool is not subject to the exhaust gas chemistry where the temperature is <600 °C. A direct oxidation of SO_2 with molecular oxygen O_2 could potentially form SO_3 in the exhaust system, but the reaction is very slow[17] at temperatures below 1100 °C in the absence of appropriate catalysts and homogeneous reactions involving SO_3 formation are practically quenching during the cylinder expansion.

Complications arise from the reactive nature of SO_3, which makes its determination in flue gases a challenge, and measurements can be biased for several reasons:[18−20]

- SO_3 is a highly reactive gas and may react with minerals of alkali ash, such as magnesium oxide (MgO) and calcium oxide (CaO)
- SO_3 measurements can be biased due to the presence of a much higher concentration of SO_2
- SO_3 may react with surfaces such as those in the sampling line
- SO_3 and H_2O form gaseous H_2SO_4 at temperatures below ∼600 °C that may be lost at "cold" surfaces due to condensation

Current experiences of SO_3 measurements are primarily based on gas sampling in exhaust ducts of coal-fired power plants, where the conditions do not exactly represent a HFO exhaust gas. One reason for this is that the fraction of ash-forming matter in typical power plant coals is high and roughly lies within the range of 10%−30% (by mass),[21] from which a fraction is thermal decomposed and oxidized into an alkaline ash during combustion. However, HFOs produce much less ash than coals, since noncombustible materials (such as mineral inclusions) are virtually absent.[22]

The most common methods for measuring SO_3/H_2SO_4 involve (1) the absorption of H_2SO_4 in an isopropanol (IPA) solution,[19,23,24] (2) the separation of H_2SO_4 by controlled condensation,[25] and (3) H_2SO_4 dew point measurement.[26] Other methods involving Fourier transform infrared spectroscopy (FTIR),[19] H_2SO_4 capture in salts,[18,27] and indirect measurements of SO_3 as carbon dioxide[28] have yielded promising results but, for practical reasons, are not considered in this work. The controlled condensation (CCD) method (also called controlled condensation system (CCS)) is the most preferred technique and recommended by the U.S. Environmental Protection Agency (EPA). Nevertheless, the British and American standards for CCD have been withdrawn.[18] In this work, the PENTOL SO_3 monitor is used, which is a modified version of the instrument formerly known as the Severn Science Analyzer. The principle is described by Jackson[24] and has been used for many years at the Central Electricity Generating Board with apparent success,[23] as well as in several power plants in the United States.[19] The principle is based on SO_3 absorption in an IPA solution where gas sampling and subsequent SO_3 determination is automated. Published data on the accuracy and repeatability does not seem to exist, but the manufacturer states that the accuracy of the monitor is ±5% of the reading in the calibrated range. Moreover, measurements conducted with the SO_3 monitor and the CCD method in a HFO power station yielded SO_3 concentrations with no significant difference.[24]

PENTOL SO_3 Monitor. The sample gas is continuously extracted through a heated (200 °C) quartz glass-lined sample probe. In the probe head at the probe exit, the gas passes a quartz wool filter before it mixes with an IPA solution, wherein the H_2SO_4/SO_3 components condense and are absorbed/stored as sulfate ions (SO_4^{2-}). The solution is then transported via an umbilical (that implies an instrument delay of ∼5 min) to a reaction bed of barium chloranilate crystals where the SO_4^{2-} ions react to form acid chloranilate ions, as seen in reaction R2.

$$SO_4^{2-} + BaC_6O_4Cl_2 + H^+ \rightarrow BaSO_4 + HC_6O_4Cl_2^- \quad (R2)$$

The acid ions absorb light preferably at 535 nm and are detected using a photometer. By maintaining a constant flow of IPA and sample gas, the H_2SO_4 + SO_3 concentration in the exhaust gas is proportional to the absorbed light. Prior to use, the monitor is calibrated with liquids equivalent to 5 ppmv and 45 ppmv of SO_3 in the sample gas.

EXPERIMENTAL SECTION

The test engine used for the experiments is a modified four-stroke single-cylinder engine equipped with a needle-controlled common rail injector prepared for multiple injections, but, in the present investigation, the fuel is injected as a single jet (i.e., no pilot injection). The engine is HFO-capable and charge air is supplied from an external pressurized vessel to allow controllable air−fuel ratios. General engine specifications are listed in Table 1.

Two HFOs with similar sulfur contents (1.6 and 2.24 wt %) are used in the experiments. Specific fuel data are listed in Table 2. The Calculated Carbon Aromaticity Index (CCAI) is a dimensionless number that is frequently used to roughly rank the ignition quality of residual fuel oils.[29,30] The number is based on the kinematic viscosity and the fuel density: The lower the number, the better the ignition characteristics. The normal CCAI range is 800−880 and satisfies fuel

dx.doi.org/10.1021/ef4014696 | Energy Fuels XXXX, XXX, XXX−XXX

Table 1. Test Engine Specifications

parameter	value/comment
number of cylinders	1
displacement volume	3.18 L
bore/stroke	150 mm/180 mm
compression ratio	13−16 (15 in the present investigation)
rated speed	1500 rpm
rated power	80 kW
fuel injection pressure	max. 1600 bar

number 1 only. However, ignition performance is also linked to engine design and operating conditions and fuels with higher CCAI values may operate successfully,[30] as experienced with the present engine.

The cylinder pressure trace is recorded with a resolution of 0.25 crank angles over 80 consecutive engine cycles via a piezoelectric pressure transducer located in the combustion chamber. To provide noise-free pressure traces, the raw pressure data are smoothened using the procedure of Harndorf.[31] Combustion processes are examined from the resulting pressure traces $p(\theta)$ in combination with the first law of thermodynamics on a differential form (eq 2), whereby the rate of heat release (ROHR) (i.e., the fuel burn rates) are calculated. The rate of the internal energy (U) of the assumed homogeneous cylinder gas system is balanced by the fuel burn rate ($\dot{Q}_f$), a wall heat loss ($\dot{Q}_w$), the system work ($p\dot{V}$), and a blow-by loss ($\dot{H}_{bb}$), which is neglected. Consequently, the derivative of the mass of the cylinder gas (m_c) in eq 3 is equivalent to the rate of the injected fuel mass (m_f).

$$\frac{dU}{d\theta} = \frac{dQ_f}{d\theta} + \frac{dQ_w}{d\theta} + p\frac{dV}{d\theta} + \frac{dH_{bb}}{d\theta} = m_c\frac{du}{d\theta} + u\frac{dm_c}{d\theta} \quad (2)$$

$$\frac{dm_c}{d\theta} = \frac{dm_f}{d\theta} \quad (3)$$

In eq 2, the specific internal energy u of the cylinder gas is calculated using the approach of Zacharias,[32] where $u = u(T,p,\lambda)$ is rewritten in terms of temperature, pressure, and excess air. Differentiating u with respect to the crank angle position (θ) yields eq 4, where r represents the instantaneous fraction of excess combustion air.

$$\frac{du}{d\theta} = \left.\frac{\partial u}{\partial T}\right|_{p,r}\cdot\frac{\partial T}{\partial \theta} + \left.\frac{\partial u}{\partial r}\right|_{p,T}\cdot\frac{\partial r}{\partial \theta} + \left.\frac{\partial u}{\partial p}\right|_{r,T}\cdot\frac{\partial p}{\partial \theta} \quad (4)$$

The gas law (eq 5) is written in terms of a real gas constant R_z,[32] which is a function of temperature, pressure, and gas composition. Differentiating T with respect to θ yields $\dot{T}$ in eq 6 and closes the system of eqs 2−6 when $\dot{V}$ in eq 4 is written in terms of the cylinder geometry, and the wall heat loss follows the procedure of Hohenberg.[33,34]

$$T = \frac{pV}{m_c R_z} \quad (5)$$

$$\frac{dT}{d\theta} = \frac{p\frac{dV}{d\theta} + V\frac{dp}{d\theta} - m_c T\frac{dR_z}{d\theta} - R_z T\frac{dm_c}{d\theta}}{m_c R_z} \quad (6)$$

Exhaust gas emissions are sampled in a 100-mm circular exhaust pipe downstream from a gas receiver (Figure 2) that works as a gas

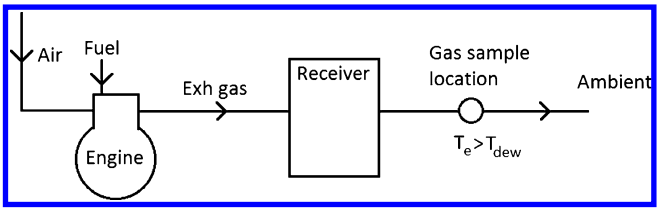

Figure 2. Experimental setup.

mixer and dampens the pressure pulsations. In all experiments, the engine is operated to produce a gas temperature that is above the acid dew point temperature all the way to the SO_3 sample probe. NO_x is measured with a chemiluminescence NO_x analyzer (CLD). CO and CO_2 are measured with an infrared gas analyzer (IRD) and O_2 is measured with a paramagnetic detector (PMD). By compensating for the sulfur bonded to SO_3 and by neglecting any sulfur associated with particulate mass, the SO_2 concentration in the exhaust gas is calculated from the fuel composition and the excess air. All experiments are conducted with the engine operating at steady state within a limited speed range of 1050 and 1500 rpm. Exhaust gas data are sampled over 4−5 min after the thermal response of the exhaust system had stabilized. In contrast, SO_3 samplings covered ∼20−30 min to detect any variations that are due to relatively long samplings. Recorded exhaust gas data are averaged and provided hereafter.

RESULTS AND DISCUSSION

Table 3 identifies the 25 individual experiments of the full test matrix that are divided into 6 test series. The experiments are listed in terms of operational data, including maximum cylinder pressure and gas emissions of SO_x and NO_x. For simplicity, the mass of trapped cylinder air is based on the charge air pressure, charge air temperature, and displacement volume. In experiments 1.1−1.4 and 2.2−2.3, the exhaust pressure was too high to allow immediate air flow through the intake valve. As a result, the trapped air−fuel ratio is set to the overall λ-value. In the remaining experiments, the trapped air−fuel ratio is lower than the overall λ-value as the intake pressure forced bypass air through the exhaust valve during the gas exchange.

Test series 1 in Table 3 represents a fuel injection timing analysis where a *fixed* amount of fuel burns equally lean at altered pressure histories. The engine speed and power output is fixed but the injection is retarded from 25 CA BTDC to 14.25 CA BTDC. [CA BTDC = crank angles before top dead center.] The different timings slightly altered the thermal efficiency between the experiments and slight variations in the fuel consumption and charge air pressures occurred. Yet, the fuel consumption did not differ by more than ±7% of the mean value.

Figure 3 illustrates the measured SO_3 profile in ppmv covering test series 1. The transition from one experiment produces a decay in the profile until a steady condition is reached that represents the subsequent experiment. The

Table 2. Specifications of Test Fuels

	Composition (wt %)									
	C	H	S	H_2O	N + O	ash	$(A/F)_s$[a] (kg_{air}/kg_{fuel})	kinematic viscosity @ 50 °C (mm^2/s)	CCAI	LHW (kJ/kg)
Fuel 1	83.47	11.08	1.6	1.68	2.1	0.06	13.4	188	838	38759
Fuel 2	88.5	8.9	2.24	0.01	0.34	0.105	13.3	115	926	40288

[a]Stoichiometric air−fuel ratio.

dx.doi.org/10.1021/ef4014696 | Energy Fuels XXXX, XXX, XXX−XXX

Table 3. Test Matrix[a]

Exp	rpm (1/min)	imep[b] (bar)	p_{max} (bar)	p_a (bar)	λ	λ_t	T_a (K)	$\dot{m}_a$ (kg/h)	SOI[c] (CAD)	Δt_{inj} (μs)	p_{inj} (bar)	fuel S (wt %)	SO_3 (ppmv)	SO_2 (ppmv)	ε (%)	NO_x (ppmv)	T_e[d] (K)	Δt_e (s)
1.1	1500	7.9	90	1.7	2.1	2.1	348	192	25	1480	920	2.2	8.3	685	1.20	1101	712	6.3
1.2	1500	8.0	84	1.7	2.0	2.0	349	191	21	1590	920	2.2	5.8	720	0.80	714	743	6.2
1.3	1500	8.3	83	1.9	2.1	2.1	350	209	17.5	1615	920	2.2	4.4	691	0.63	426	762	5.6
1.4	1500	7.9	81	1.9	2.1	2.1	351	218	14.25	1630	920	2.2	3.8	694	0.54	370	780	5.3
2.1	1200	6.3	89	1.4	3.3	2.8	346	179	21	1230	1020	2.2	10.7	441	2.37	1536	540	8.0
2.2	1200	6.1	83	1.3	2.5	2.5	346	142	21	1050	1020	2.2	13.1	576	2.22	1885	602	9.4
2.3	1200	5.9	75	1.2	2.0	2.0	348	107	21	1280	1020	2.2	14.2	719	1.94	1631	684	11.5
3.1	1500	17.3	124	2.4	2.3	1.6	345	485	23.5	3900	1020	1.6	7.2	443	1.60	648	783	2.3
3.2	1500	17.9	119	2.5	2.3	1.6	343	509	19.25	4220	1020	1.6	6.6	445	1.46	502	806	2.2
3.3	1500	17.7	113	2.6	2.4	1.7	345	530	15.25	4130	1020	1.6	6.2	424	1.44	453	799	2.2
4.1	1500	17.8	120	2.4	2.3	1.7	335	484	19.25	3470	1250	1.6	7.5	441	1.67	730	767	2.4
4.2	1500	12.8	93	2.1	2.5	1.8	346	409	15	3490	920	1.6	4.8	419	1.13	287	802	2.8
4.3	1500	12.8	90	2.0	2.3	1.7	346	395	15	2976	1120	1.6	4.9	445	1.09	340	804	2.9
4.4	1500	14.9	104	2.2	2.4	1.7	345	432	19	3470	1020	1.6	5.0	439	1.13	442	804	2.6
4.5	1500	14.7	100	2.2	2.3	1.7	346	433	18	3578	1020	1.6	4.6	460	0.99	410	815	2.6
4.6	1200	18.2	130	2.3	2.3	1.6	345	379	19	3414	1110	1.6	8.9	452	1.93	1296	702	3.2
4.7	1500	7.9	70	1.6	1.5	1.5	363	154	17.5	1600	920	2.2	4.6	952	0.48	563	863	6.9
5.1	1200	15.9	115	2.1	2.4	1.7	327	352	18.5	3250	1020	1.6	6.9	426	1.59	883	705	3.5
5.2	1200	15.9	105	1.9	2.0	1.5	328	307	18.5	3448	1020	1.6	7.2	516	1.38	1036	764	3.8
5.3	1200	15.8	124	2.4	3.1	2.1	337	416	18.5	3195	1020	1.6	6.3	336	1.84	792	619	3.2
6.1	1400	14.1	98	2.0	2.3	1.7	347	372	18.5	3098	1020	1.6	5.1	452	1.12	556	773	3.1
6.2	1300	13.8	97	1.9	2.2	1.6	347	335	18.5	3058	1020	1.6	5.6	464	1.19	672	759	3.5
6.3	1200	13.7	103	1.8	2.3	1.6	346	311	18.5	2980	1020	1.6	6.3	440	1.41	813	710	3.9
6.4	1100	14.1	105	1.7	2.2	1.6	337	274	18.5	3070	1020	1.6	8.5	463	1.80	1113	694	4.5
6.5	1050	14.4	111	1.8	2.3	1.6	327	272	18.25	3064	1020	1.6	9.3	444	2.05	1254	679	4.6

[a]The first column on the left-hand side represents the test series numbers and the experiment numbers. [b]Indicated mean effective pressure. [c]Start of fuel injection, in terms of crank angle degrees (CAD). Before top dead center (BTDC). [d]At the exhaust valve outlet.

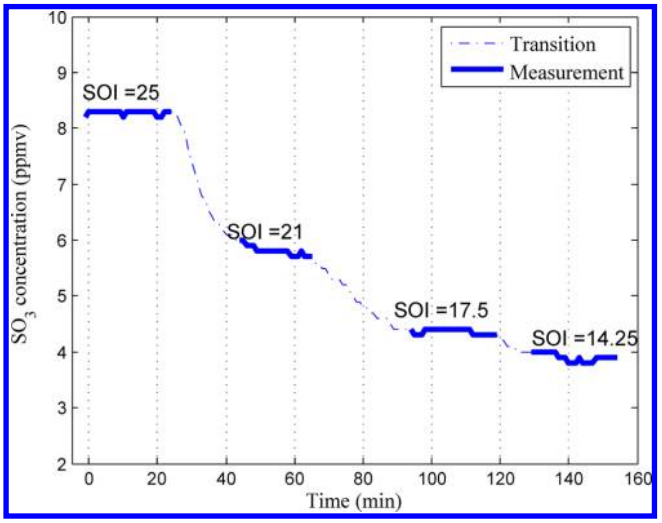

Figure 3. Measured SO_3 profile of test series 1. The numbers in the figure refer to the different injection timings.

transition is a combination of engine tuning and response time of the SO_3 monitor. During each experiment, a practically constant concentration is identified throughout the ~20 min of sampling. As illustrated, the SO_3 concentration/formation decreases as the injection timing is retarded and fairly small concentrations are detected consistently by the monitor.

In test series 1, the exhaust gas temperature (~475 °C at the engine exhaust valve) and the gas flow results in comparable gas residence times of ~5.5 s from the engine exhaust valve to the SO_3 probe, as seen in Table 3). The probe is heated to 200 °C and provides a sample gas residence time of ~2 s through the probe. At both temperature levels, SO_3 is thermodynamically preferred over SO_2. Yet, post-flame investigations indicate that gaseous SO_3 reactions are very slow at these temperatures and considered frozen in the exhaust system. Metal oxides such as iron oxide, chrome oxide, and vanadium oxide (all in various oxidation numbers) may be present in the gas stream and on internal surfaces. The metal oxides can serve as oxygen carriers and catalyze the oxidation of SO_2 to SO_3 in the exhaust gas. Although the SO_2 concentration in the exhaust gas is high, relative to SO_3, the fraction of SO_2 that is converted to SO_3 is low, especially in experiment 1.4 (ε = 0.54), as seen in Table 3. Consequently, the potential of a gaseous or catalytic SO_3 formation in the exhaust system seems very limited.

ROHR traces of test series 1 are shown in Figure 4. Earlier injections advance the point of fuel ignition relative to top dead center (TDC) (CA ATDC = 0) and promote the share of premixed combustion that is defined as the area below the peak in a ROHR trace around TDC. [CA ATDC = crank angles after top dead center.] The combined effect results in maximum pressure variations in the range of 81−90 bar that increases with earlier injections, since more fuel then burns around TDC, where the gas volume is small. Specific exhaust gas emissions of

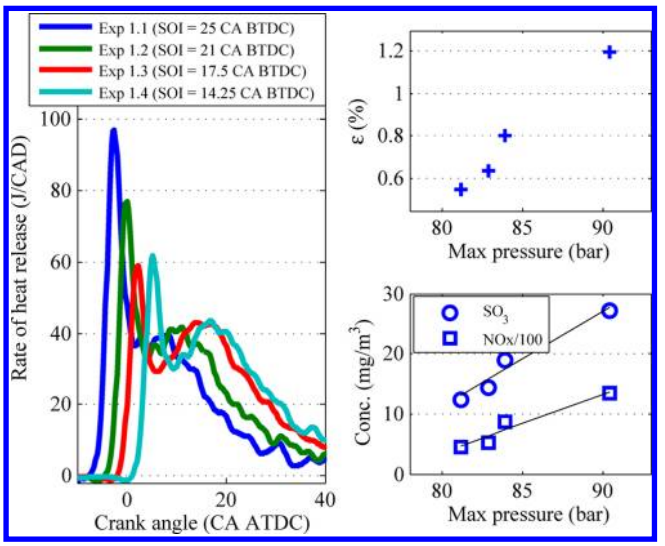

Figure 4. Test series 1: (left) ROHR traces, (upper right) sulfur to SO_3 conversion versus the maximum cylinder pressure, and (lower right) specific emissions of SO_3 and NO_x versus the maximum cylinder pressure. The maximum pressure increases with earlier fuel injections, relative to top dead center (TDC).

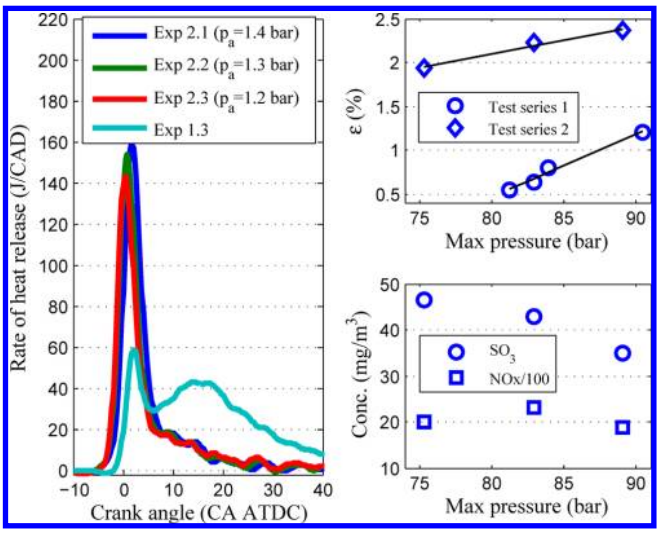

Figure 5. Test series 2: (left) ROHR traces, (upper right) sulfur to SO_3 conversion versus the maximum cylinder pressure, and (lower right) specific emissions of SO_3 and NO_x versus the maximum cylinder pressure. The maximum pressure increases with elevated charge air pressures (p_a).

NO_x and SO_3, expressed in units of mg per normal m^3 (mg/Nm^3) are plotted against maximum cylinder pressure in Figure 4. The response from the altered combustion history is comparable as both species are favored by elevated pressures. Hence, operating conditions that promote NO_x promote SO_3 in a similar fashion, under the present circumstances, and SO_3 emissions increase at the expense of SO_2, as illustrated by ε in the figure. Although SO_3 is clearly manipulated by the combustion history, it is not clear whether the altered pressure levels alone are responsible for this. An argument for this is that the share of premixed combustion is not comparable but varies from 17% to 34% over the four experiments, as indicated by the ROHR traces in Figure 4.

To quantify the influence of premixed combustion on SO_3 formation, test series 2 in Table 3 is performed, where the share of premixing is promoted by reducing the engine speed, combined with early injections. Moreover, the pressure history is altered via the charge air pressure. The resulting ROHR traces are presented in Figure 5, together with the trace of experiment 1.3 for comparison. The share of premixed combustion is comparably high and heterogeneous-mixing-controlled combustion is virtually absent in test series 2. Consistent with the results of test series 1, ε increases with the maximum pressure. However, despite an overlapping maximum pressure range, the ε-values are significantly higher in test series 2, as illustrated in Figure 5. Speed investigations presented later in the section demonstrate that the lower engine speed in test series 2 cannot explain the present observations. As a result, SO_3 is promoted with the share of premixed combustion and the slope of ε in test series 1 seems to be a consequence of altered pressure histories combined with inconsistent premixed proportions. Specific emissions of SO_3 and NO_x from test series 2 in Figure 5 are not readily comparable, because of different excess air ratios, as seen in Table 3. Yet, for both species, the emissions are remarkably higher than in test series 1 presented in Figure 4 and likely caused by the superior fractions of premixed combustion.

Premixed combustion refers to the fuel that evaporates and mixes partially with air prior to ignition and incomplete burning. As a result, *intermediate* gas products, such as CO, are formed before the more complete oxidation. CO flames produce high concentrations of oxygen atoms[35] which promotes thermal NO_x, and combined with SO_2, is a main source of SO_3 formation,[3] consistent with the superior species concentrations experienced in test series 2. In this respect, one-dimensional (1D) reactor experiments with staged combustion (i.e., rich combustion prior to secondary air entrainment) have been shown to increase SO_3 formation,[5,36] compared to single-stage combustion at identical overall lean air−fuel ratios. In addition, CO flames doped with sulfur species have been shown to produce increased amounts of SO_3, compared to sulfur-doped methane flames[37] that involve lesser concentrations of atomic oxygen.

Test series 3 in Table 3 involves retarded injection timings similar to test series 1 but is conducted at higher loads to produce low premixed proportions (~6%) and thereby provide practically full mixing controlled combustion histories, as illustrated by the ROHR traces in Figure 6. As expected, the variations of ε are decreased, compared to that observed in test series 1, but the altered pressure history still manipulates SO_3 and NO_x formation, as illustrated in the figure where the specific emissions increase moderately over the maximum pressure range.

The correlation between maximum cylinder pressure and SO_3 formation is examined over a widespread pressure range wherein engine operational conditions are altered to vary the pressure history. SO_3 formation is hereby studied in relation to engine power, engine speed, air−fuel ratio, and fuel injection timing. The operating points are recognized in Table 3 and the share of premixed combustion is <20% in the remaining experiments (test series 4−6) to provide comparable measurements for the data analysis. In the lower-pressure range, fuel 2 proved to be most successful, providing acceptable levels of premixing, in contrast to fuel 1, which is associated with the superior ε-values of test series 2.

In test series 4, the trapped air−fuel ratio is kept comparably constant but the fuel input is altered to investigate the response of SO_3, relative to engine load. The correlation between ε and

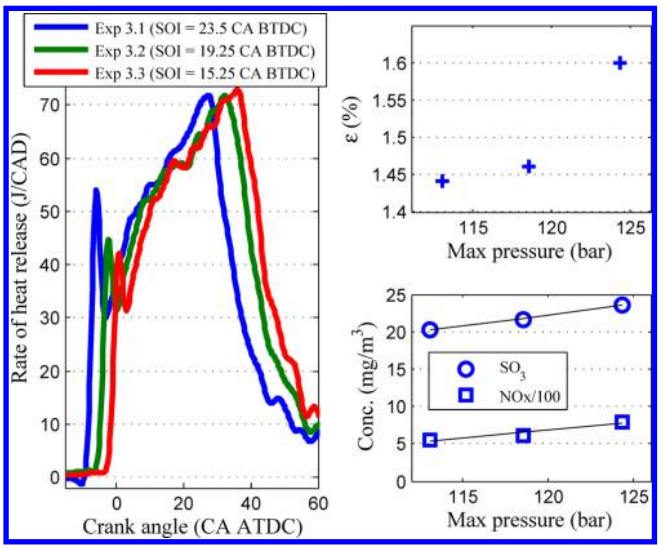

Figure 6. Test series 3: (left) ROHR traces, (upper right) sulfur to SO_3 conversion versus the maximum cylinder pressure, and (lower right) specific emissions of SO_3 and NO_x versus the maximum cylinder pressure. The maximum pressure increases with earlier fuel injections, relative to TDC.

the maximum pressure is well-represented by a linear fit, as seen in Figure 7, where ε increases from 0.5% to 1.8% at 70 and 130

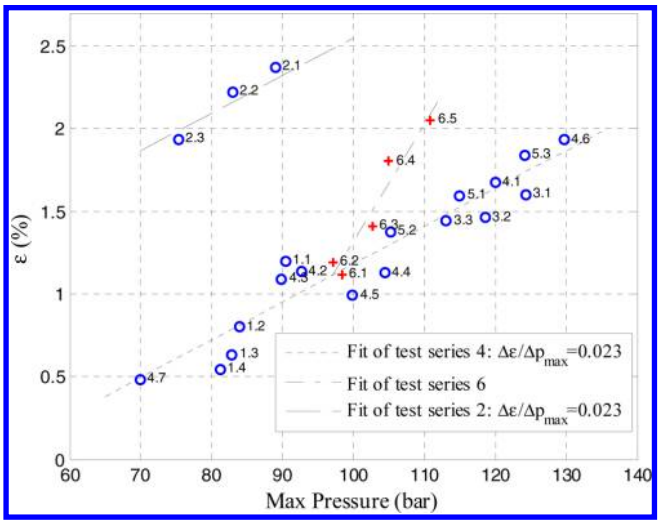

Figure 7. Correlation between fuel sulfur converted to SO_3 and maximum cylinder pressure. The numbers in the figure refer to the test series and experiments in Table 3.

bar, respectively. The accompanying emissions of SO_3 and NO_x are presented in Figure 8. Since the emissions are based on the exhaust gas composition, the trace of the two curves is partially governed by the different overall air−fuel ratios. Nonetheless, the response of SO_3 and NO_x is comparable over the 60 bar pressure range, as both species are favored with increasing maximum pressures.

In test series 5, the charge air pressure is altered, relative to the injected fuel mass, to investigate the influence of trapped air−fuel ratio. The different charge pressures alter the resulting max pressures that cover a range from 105 bar to 124 bar. Yet, the associated ε-values presented in Figure 7 respond to the linear fit of test series 4. Consequently, the different ε-values of test series 5 are caused by the altered charge air pressures rather

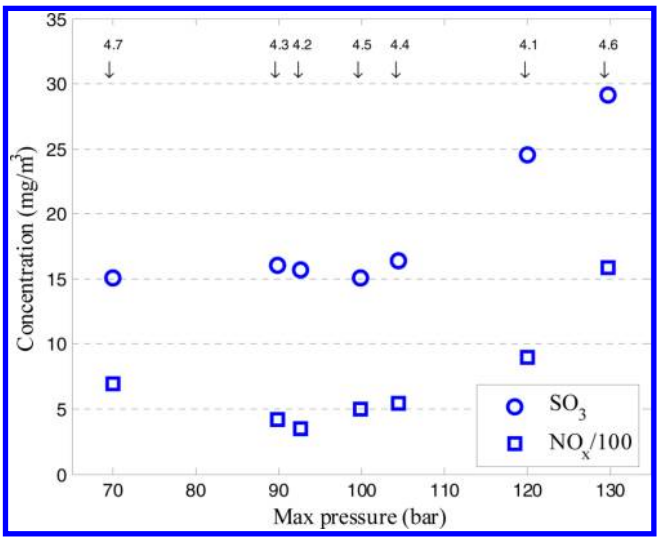

Figure 8. Test series 4: specific emissions of SO_3 and NO_x versus maximum cylinder pressure. The numbers in the figure refer to the test series and experiments in Table 3.

than the different air−fuel ratios. The statement is supported by the results of test series 2, where the charge air pressure is similarly altered and leads to a ε-slope that matches the linear fit of test series 4, as seen in Figure 7.

The combined results of test series 1 and 3−5 in Figure 7 demonstrates that a correlation between the maximum cylinder pressure and ε applies and is well-represented by a linear fit of the full dataset. The fuel flame temperature is weakly influenced by the pressure and neither is SO_3 favored at the highest temperatures in a diesel process.[6] However, elevated pressures promote SO_3 theoretically according to general chemical equilibrium. Moreover, a higher pressure increases the gas density and the partial pressures of gas species in the cylinder that, in reference to the current results, improve elementary reactions of SO_3 formation at the expense of SO_2.

The influence of engine speed is investigated in test series 6, which represents five experiments with different speeds in the range of 1050−1400 rpm. Basically, a fixed fuel mass is burned in a fixed amount of air but the rate of gas expansion is linked to the different engine speeds (rpm), which, in turn, cause altered pressure histories. Resulting ε-values are plotted in Figure 7. At speeds above 1200 rpm, the variations are small. Yet, a linear fit through the dataset demonstrates a steeper positive slope, compared to the remaining experiments. Consequently, a reduction of the engine speed favors SO_3 formation.

Figure 9 presents the specific emissions of NO_x and SO_3 for the speed analysis. The results are plotted against engine speed, although the variations, to some extent, are also governed by the different pressure histories. Reduced engine speed provides better gas mixing between hot gas products and air in the cylinder, as well as prolonged time for chemical reactions. When the temperature is still sufficient, the excess air provides free radicals such as atomic oxygen to the hot gas products. It is well-documented that oxygen is essential in the case of high-temperature SO_3 and thermal NO_x formation, which is consistent with the present results in Figure 9, where the emissions decrease with the engine speed. Moreover, in a modeling study,[6] the gas mixing was found to be essential, relative to SO_3 and NO_x formation.

dx.doi.org/10.1021/ef4014696 | Energy Fuels XXXX, XXX, XXX−XXX

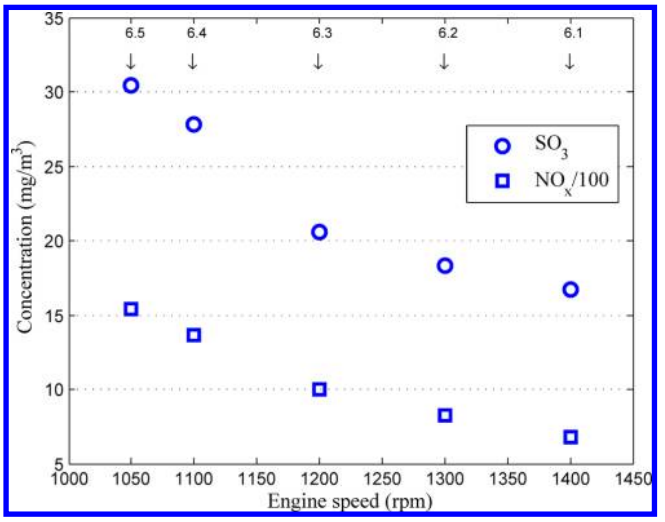

Figure 9. Test series 6: specific emissions of SO_3 and NO_x versus engine speed. The numbers in the figure refer to the test series and experiments in Table 3

CONCLUSIONS

The formation of SO_3 is investigated with an 80 kW heavy fuel oil (HFO)-fuelled medium-speed single-cylinder test engine running at steady state. For practical reasons, two fuels with comparable sulfur contents (1.6 and 2.24 wt %) are used in the investigations. SO_3 is measured in the exhaust gas with the PENTOL SO_3 monitor and the fraction of fuel sulfur converted to SO_3 is examined at different fuel injection timings, engine loads, speeds, and air−fuel ratios. The SO_3 monitor operated successfully in the HFO exhaust and provided consistent readings in the existing SO_3 range from 4 ppmv to 14 ppmv.

SO_3 is shown to scale proportionally with the maximum cylinder pressure and inversely with the engine speed. Present maximum pressures and speeds range from 70 bar to 130 bar and from 1050 rpm to 1500 rpm, respectively, where the measured sulfur to SO_3 fraction is on the order of 0.5%−2.4%. Elevated pressures yield higher partial pressures of the species involved in the elementary SO_3 reactions, and reduced speeds leave more time for air−gas mixing, in favor of SO_3 formation. Abnormal combustion with high shares of premixed combustion increases SO_3 formation remarkably and may be explained by the accompanied CO chemistry introducing high concentrations of atomic oxygen that, combined with SO_2, is a significant source of SO_3.

Specific emissions of NO_x and SO_3 are compared in parallel, since both species are governed by the radical pool in a high-temperature process. The response of SO_3 in the exhaust gas from altered operating conditions is comparable to NO_x in the sense that both species are favored by increased pressure histories and reduced engine speeds.

AUTHOR INFORMATION

Corresponding Author

*E-mail: rco@mek.dtu.dk.

Notes

The authors declare no competing financial interest.

ACKNOWLEDGMENTS

The support and guidance by PENTOL GmbH and MAN Diesel and Turbo is gratefully acknowledged.

NOMENCLATURE

H_{bb} = enthalpy of cylinder blow-by gas (kJ)
m_c = mass of trapped cylinder gas (kg)
m_f = injected fuel mass (kg)
$\dot{m}_a$ = charge air flow (kg/h)
p = cylinder pressure (Pa)
p_a = charge air pressure (bar)
p_{inj} = fuel injection pressure (bar)
p_{max} = maximum cylinder pressure (bar)
Q_f = latent fuel heat (kJ)
Q_W = cylinder wall heat transfer (kJ)
r = fraction of residual air in cylinder
R_z = real gas constant (J/(kg K))
T = cylinder gas temperature (K)
T_a = charge air temperature (K)
T_{dew} = acid dew point temperature (°C)
T_e = exhaust gas temperature (K)
u = specific internal energy of cylinder gas (kJ/kg)
U = internal energy of the cylinder gas (kJ)
V = cylinder volume (m^3)
ε = fraction of fuel sulfur converted to SO_3
θ = crank angle position (°,rad)
Δt_e = gas residence time in exhaust system (s)
Δt_{inj} = fuel injection duration (ms)
λ = overall excess air ratio (kg/kg)
λ_t = trapped (in cylinder) excess air ratio (kg/kg)

Abbreviations

CA ATDC = crank angles after top dead center
CA BTDC = crank angles before top dead center
CAD = crank angle degrees
HFO = heavy fuel oil
imep = indicated mean effective pressure
LHW = lower heating value of fuel
ROHR = rate of heat release
rpm = revolutions per minute
TDC = top dead center
SOI = start of fuel injection

REFERENCES

(1) Bartok, W.; Sarofim, A. *Fossil Fuel Combustion: A Source Book*; Wiley: New York, 1991.
(2) Johnson, G. M.; Matthews, C. J.; Smith, M. Y.; Williams, D. J. Distribution of sulfur species in the burnt gas of fuel-rich propane−air flames. *Combust. Flame* **1970**, *15*, 211−214.
(3) Hindiyarti, L.; Glarborg, P.; Marshall, P. Reactions of SO_3 with the O/H radical pool under combustion conditions. *J. Phys. Chem. A* **2007**, *111*, 3984−3991.
(4) Glarborg, P.; Kubel, D.; DamJohansen, K.; Chiang, H.; Bozzelli, J. Impact of SO_2 and NO on CO oxidation under post-flame conditions. *Int. J. Chem. Kinet.* **1996**, *28*, 773−790.
(5) Hedley, A. B. Sulphur trioxide in combustion gases. *Fuel Soc. J.* **1962**, *13*, 45−54.
(6) Cordtz, R.; Schramm, J.; Andreasen, A.; Eskildsen, S. S.; Mayer, S. Modeling the distribution of sulfur compounds in a large two stroke diesel engine. *Energy Fuels* **2013**, *27*, 1652−1660.
(7) Pierce, R. Estimating Acid Dewpoints in Stack Gases. *Chem. Eng.* **1977**, *84*, 125−128.
(8) Verhoff, F. H.; Banchero, J. T. Predicting Dew Points of Flue Gases. *Chem. Eng. Prog.* **1974**, *70*, 71−72.
(9) Mueller, P. Influence of sulphuric acid on dew point temperature of flue gases. *Chem.-Ing.-Tech.* **1959**, *31*, 345−351.
(10) Greenewalt, C. H. Partial pressure of water out of aqueous solutions of sulfuric acid. *Ind. Eng. Chem.* **1925**, *17*, 522−523.

(11) Teetz, C. Investigation into Reducing Low Temperature Corrosion in Diesel Engines (Beitrag zur Verminderung der Nasskorrosion im Dieselmotor, Nr 626). *VDI Forschungsh.* **1984**.
(12) Andreasen, A.; Mayer, S. Modeling of the oxidation of fuel sulfur in low speed two-stroke Diesel engines. Presented at the *26th CIMAC World Congress*, Bergen, Norway, 2010; Paper No. 39.
(13) Engel, P. K.; Thompson, R. E.; Silvestrinin, R. Corrosion and Fouling Potential in Diesel Exhausts. *Mech. Eng.* **1979**, *101*, 598−606.
(14) Gill, D.; Ofner, H.; Schwarz, D.; Sturman, E.; Wolverton, M. A. The Performance of a Heavy Duty Diesel Engine with a Production Feasible DME Injection System. *SAE Tech. Pap.***2001**, 2001-01-3629.
(15) Scholl, K. W.; Sorenson, S. C. Combustion of soybean oil methyl ester in a direct injection diesel engine. *SAE Tech. Pap.* **1993**, 930934.
(16) Ferguson, C. R., Kirkpatrick, A. T., Eds. *Internal Combustion Engines: Applied Thermosciences*; Wiley: New York, 2001.
(17) Cullis, C. F.; Mulcahy, M. F. R. The kinetics of combustion of gaseous sulphur compounds. *Combust. Flame* **1972**, *18*, 225−292.
(18) Fleig, D.; Vainio, E.; Andersson, K.; Brink, A.; Johnsson, F.; Hupa, M. Evaluation of SO_3 Measurement Techniques in Air and Oxy-Fuel Combustion. *Energy Fuels* **2012**, *26*, 5537−5549.
(19) Denne, C.; Himes, R. *Continuous Measurement Technologies for SO_3 and H_2SO_4 in Coal-Fired Power Plants*, Technical Report, Electric Power Research Institute (EPRI), Palo Alto, CA, 2004.
(20) Srivastava, R. K.; Miller, C. A.; Erickson, C.; Jambhekar, R. *Emissions of Sulfur Trioxide From Coal-Fired Power Plants*, Riley Power, Inc., Report No. RPI-TP-0178, 2002.
(21) Turns, S. R. *An Introduction to Combustion: Concepts and Applications*; McGraw−Hill: New York, 2012.
(22) Flagan, R. C.; Seinfeld, J. H. *Fundamentals of Air Pollution Engineering*; Prentice Hall: Englewood Cliffs, NJ, 1988.
(23) Jaworowski, R. J.; Mack, S. S. Evaluation of Methods for Measurements of SO_3/H_2SO_4 in Flue-Gas. *J. Air Pollut. Control Assoc.* **1979**, *29*, 43−46.
(24) Jackson, P. J.; Hilton, D. A.; Buddery, J. H. Continuous Measurement of Sulphuric Acid Vapour in Combustion Gases using a Portable Automatic Monitor. *J. Inst. Energy* **1981**, *54*, 124−135.
(25) United States Environmental Protection Agency (EPA): Available online: http://www.epa.gov/ttnemc01/ctm/ctm-013.pdf.
(26) Land, T. Theory of Acid Deposition and its Application to the Dew-Point Meter. *J. Inst. Fuel* **1977**, *50*, 68−75.
(27) Vainio, E.; Fleig, D.; Brink, A.; Andersson, K.; Johnsson, F.; Hupa, M. Experimental Evaluation and Field Application of a Salt Method for SO_3 Measurement in Flue Gases. *Energy Fuels* **2013**, *27*, 2767−2775.
(28) Ibanez, J. G.; Batten, C. F.; Wentworth, W. E. Simultaneous determination of $SO_3(g)$ and $SO_2(g)$ in a flowing gas. *Ind. Eng. Chem. Res.* **2008**, *47*, 2449−2454.
(29) Zeelenberg, A. P.; Fijn, v. D.; Barker, H. L. Ignition Performance of Fuel Oils in Marine Diesel Engines. *Int. Congress Combust. Engines* **1983**, 1455−1469.
(30) Valencia, F. A.; Armas, I. P. Ignition Quality of Residual Fuel Oils. *J. Mar. Res.* **2005**, *2*, 77−96.
(31) Harndorf, H.; Kösel, R.; Volkart, A. Optimierung der Mess- und Auswerteparameter zur Analyse von Zülinderdruckverlaufen. *Motortech. Z.* **1992**, *53*, 136 ff.
(32) Zacharias, F. *Analytische Darstellung der Thermodynamischen Eigenschaften von Verbrennungsgassen*, Dissertation Thesis, TU Berlin, Berlin, Germany, 1966.
(33) Hohenberg, G. *Experimentelle Erfassung der Wandwärme in Kolbenmotoren*, Habilitationsschrift, Technische Universität Graz, Graz, Austria, 1983.
(34) Hohenberg, G. F. Advanced Approaches for Heat Transfer Calculations. *SAE Tech. Pap.* **1979**, Paper No. 790825.
(35) Gaydon, A. G. Continuous Spectra in Flames: The Role of Atomic Oxygen in Combustion. *Proc. R. Soc. London, Ser. A* **1944**, *183*, 111−124.
(36) Merryman, E. L.; Levy, A. Enhanced SO_3 Emissions from Staged Combustion. *Symp. Int. Combust.* **1979**, 727−736.
(37) Dooley, A.; Whittingham, G. The Oxidation of Sulphur Dioxide in Gas Flames. *Trans. Faraday Soc.* **1946**, *42*, 354−366.

Characteristics of Sulfuric Acid Condensation on Cylinder Liners of Large Two-Stroke Marine Engines

Rasmus Cordtz, Stefan Mayer, Jesper Schramm, Svend S. Eskildsen

Abstract

The present work seeks to clarify the characteristics of sulfuric acid condensation on the cylinder liner of a large two–stroke marine engine. The liner is directly exposed to the cylinder gas (i.e. no protective lube oil film) and is represented by a constant temperature over the full stroke. Formation of corrosive sulfuric acid in the cylinder gas is modeled with a calibrated engine model that incorporates a detailed sulfur reaction mechanism. Condensation of sulfuric acid follows the analogy between heat and mass transfer. Average bulk gas acid dew points are calculated by applying two-phase thermochemistry of the binary H_2O-H_2SO_4 system. Max dew points of typically more than 200 °C are modeled close to max pressure and variations in terms of operating conditions are not large. However small increments of the dew point provided by e.g. the residual gas fraction, operating pressure, sulfur content and charge air humidity acts to increase the surface area that is exposed to condensation. Depending on the actual liner temperature the deposition of sulfuric acid can be very sensitive to the operating strategy. A higher liner temperature theoretically provides the means to hamper sulfuric acid condensation.

1. Introduction

When Heavy Fuel Oil (HFO) including sulfur is burned in a marine engine the cylinder liner is exposed to gas products of sulfur trioxide (SO_3) and sulfur dioxide (SO_2) where the latter is the primary sulfur compound. According to thermodynamic considerations the bulk gas temperature is generally too high to form corrosive sulfuric acid (H_2SO_4). Yet H_2SO_4 may form at the cooled liner surface from an instant reaction between SO_3 and water vapor (H_2O) that is a major combustion product. Consequently SO_3 and H_2SO_4 are lumped together and the fraction of fuel sulfur that is converted to corrosive species is formulated by eq. 1. In practice the fraction accounts for a few percent but it varies with operating conditions and fuel sulfur content [1,2].

$$\varepsilon = \frac{[SO_3]}{[SO_3]+[SO_2]} \quad (1)$$

If the liner temperature is lower than the sulfuric acid dew point then a part of the H_2SO_4 and H_2O in the bulk gas condense according to the thermochemistry of the binary H_2O-H_2SO_4 system. Liner corrosion is especially coupled to H_2SO_4 condensation as deposited liquid acid accelerates the degradation of the cast iron liner materiel. In practice it is experienced that uncontrolled corrosion can severely reduce the life time of a cylinder liner. To hamper

corrosion commercial cylinder lube oils are blended with acid neutralizing base additives that combined with the lube oil dosing strategy provides the means to prevent corrosion.

The sulfuric acid dew point may be determined from empirical formulas [3,4] that correlate the temperature with the pressure of SO_3 and H_2O. However such correlations do not provide information about the share of condensing H_2SO_4 and H_2O. A more convenient approach for the present study is to apply the thermochemistry of the two-phase H_2O-H_2SO_4 system. Theoretical correlations of this type are based on thermodynamic properties of the components in the gas and liquid phase. Abel [5] was among the first to derive the vapor-phase above a liquid solution of sulfuric acid and water. He used the best available thermodynamic data at that time. The theoretical models have been improved over the years as the thermodynamic data have been gradually upgraded. Today several correlations are suggested [5-9]. In this work the quite recent work of Bosen & Engels [10] is used to describe the complex nature of the H_2O-H_2SO_4 system. The model treats ideal gasses above a liquid solution where the partial pressures p_i (index i refers to H_2O and H_2SO_4) are calculated from the general expression in eq. 2. χ_i is the liquid mole fraction, γ_i is an activity coefficient and p_i^0 is the vapor pressure of the pure substance [11,12]. The activity coefficient is derived from the NRTL (Non-Random Two Liquid model) equation [13] wherein adjustable parameters are fitted to reproduce experimental data of total pressure, vapor phase composition and liquid molar enthalpy. The experimental data are cited in the work of Bosen & Engels that describe the phase equilibrium of the H_2O-H_2SO_4 system up to 96 % m/m H_2SO_4 in the temperature range between 0 - 240 °C.

$$p_i(T, c_a) = x_i \gamma_i {p_i}^0 \quad (2)$$

According to Gibbs phase rule the two phase H_2O-H_2SO_4 system yields two degrees of freedom. For a liquid phase at a given acid strength (c_a) eq. 2 provides the saturation pressures of H_2SO_4 and H_2O at a defined temperature. If the procedure is reversed then known pressures of H_2SO4 and H_2O can be applied to the equation from which the dew point temperature and the condensing acid strength can be determined.

The present work does not address liner corrosion directly but seeks to clarify the characteristics of H_2SO_4 condensation. The cylinder liner is directly exposed to the cylinder gas. I.e. the influence of the protecting lube oil is not considered. Gas species concentrations are simulated with a calibrated engine model [1] that includes a detailed sulfur reaction mechanism [14]. The process of condensation is modeled as molecular gas diffusion through the gaseous boundary layer very close to the liner surface. For the purpose the analytic expressions of Müller [15] are used which are based on the analogy between heat and mass transfer. In his theoretical approach Müller implemented the theory of a semi permeable gas-liquid interface that acts to hamper condensation due to convective motions from the non-condensable gases. Moreover the expressions are derived from the assumption of fully developed turbulence that reasonably fits the conditions in a large two-stroke marine engine.

2. Engine Model

In cylinder species formation is simulated with a multizone engine model that is previously developed by the authors [1]. The model incorporates a detailed sulfur reaction mechanism [14] besides the extended Zeldovich mechanism [16] in order to simulate products of sulfur compounds, mayor C-H-O species and nitrogen oxides (NO). The fuel is composed by n-dodecane ($C_{12}H_{26}$) and non-bonded elemental sulfur.
In the multizone approach the complex nature of the diesel spray and flame is not directly modeled. Instead the model seeks to reproduce flame conditions by separating the overall

fuel mass in multiple burned gas zones with no spatial location (0D model). At each crank angle from the point of fuel ignition and until the combustion is completed a new burned zone is created where the fuel burns stoichiometrically with fresh gas. The fresh gas is composed by charge air (normally dry air) including residual gasses that remain in the cylinder after the scavenging process. The flame temperature of a burned zone is calculated from the assumption that the gas products are immediately equilibrated at the high temperature in the order of ≈2600-2700 K. Hereafter a burned zone is diluted with fresh gas every crank angle during the expansion stroke at a defined rate. No more fuel is added to a burned zone and no gas exchange is considered between burned zones either. Consequently the ratio of air to combustion products increases in the burned zones during expansion and meanwhile the mass of the fresh gas is reducing. In the published material [1] the fresh gas chemistry is assumed to be frozen. In the present work however the fresh gas is treated as a homogenous zone wherein chemical reactions are considered from the point where compression starts and until the exhaust valve opens. The subsequent scavenging process is not modeled. Instead the residual gas fraction is set as a model input.
Due to the absence of experimental SO_3 measurements the model is calibrated against exhaust gas concentrations of NO produced by the large two-stroke reference engine specified in Table 1. The engine represents a modern marine engine that operates according to a simulated propeller curve [17] and experimental operating data are used as model input.

Number of cylinders	4
Bore/stroke	500mm / 2200 mm
Max speed	123 RPM
Max power	7050 kW

Table 1. *Specifications of the reference (two-stroke) marine engine used to investigate the characteristics of sulfuric acid condensation on the cylinder liner.*

3. Engine Simulations

In service the large marine engines operate at different loads and with fuels of varying sulfur contents. Consequently a cylinder liner will be exposed to gas species of varying densities that alter the properties of sulfuric acid condensation. In order to limit the number of simulations a constant sulfur content of 2 % m/m is used in this work at the operating conditions representing 25 % and 100 % engine load. Moreover the residual gas fraction is set to 3 % and 6 % m/m as seen in Table 2 that holds the four studied base cases.

	load	rpm	Fuel S	x_{res}	p_{boost}	T_{air}	p_{max}	λ_t	ε^*
Case	%	rev/min	% m/m	% m/m	bar	°C	bar	-	%
1	100	123	2.0	6	3.8	37	167	2.13	2.70
2	100	123	2.0	3	3.8	37	172	2.32	2.74
3	25	78	2.0	6	1.5	33	89	2.47	3.65
4	25	78	2.0	3	1.5	33	90	2.67	3.69

*at exhaust valve opening

Table 2. *Studied cases used to investigate the characteristics of sulfuric acid condensation in a large marine engine.*

In a previous work [1] the rate of combustion was determined for the two engine loads in Table 2 by combining a measured cylinder pressure trace with the first law of thermodynamics. In this work the process is reversed and the “known” combustion rate is used to calcu-

late the cylinder pressure history. This is a fair approach due to the slight variations of the residual gas fraction. The cylinder pressure plays a key role as it significantly affects SO_3 formation [2] and alters the properties of condensation throughout the cycle. The modeled pressure histories are presented in Figure 1. When the residual gas fraction is increased the mass of trapped fresh gas reduces a little. This leads to a slight reduction of the pressure trace as seen for the two engine loads in Figure 1.

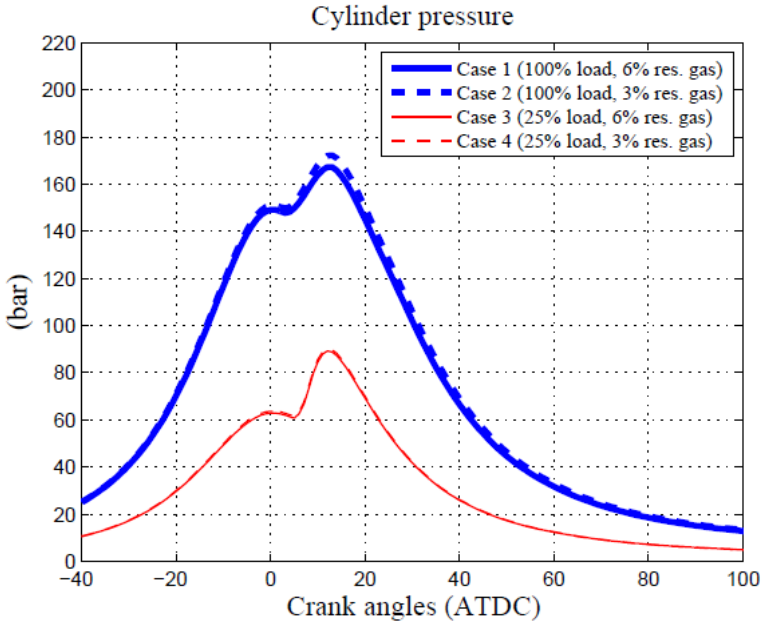

Figure 1. *Cylinder pressure traces of the studied cases in Table 2.*

4. Results

The ε-values defined in eq. 1 and listed in Table 2 describe the fraction of fuel sulfur that is converted to corrosive species at the point where the exhaust valve opens (EVO). Compared to the published material [1] the listed ε-values are slightly lower. This is explained by the implementation of improved experimental input data for the current engine simulations. Despite a higher operating pressure the ε-values are lowest at 100 % load. This reason for this is the lower engine speed at 25 % load that leaves more time for cylinder gas mixing which elevates the SO_3 formation [1, 2].

Modeled SO_3 concentrations over the expansion stroke are presented in Figure 2. Residual gasses from the prior engine cycle provide the initial SO_3 concentrations of less than 2 ppmv around TDC (Crank angles ATDC = 0). When the fuel sulfur burns SO_2 is the primary sulfur compound in the gas products. SO_3 forms at the expense of SO_2 during the expansion stroke at lower gas temperatures. However the governing SO_3 reactions are essentially quenched when the radical pool vanishes and final SO_3 concentrations are less than 20 ppmv.

Formation of H_2O reflects the fuel burn rate and H_2O exists in much higher concentrations than SO_3. As H_2O and SO_3 are formed under different thermal conditions the shape of their pressure traces are quite different as seen in Figure 2. Due to the operating conditions and the residual gas fraction the SO_3 pressure peaks in case 1 a little after TDC as seen in Figure 3. Otherwise the SO_3 pressure peaks some 50-80 CA ATDC when SO_3 is formed in the gas products.

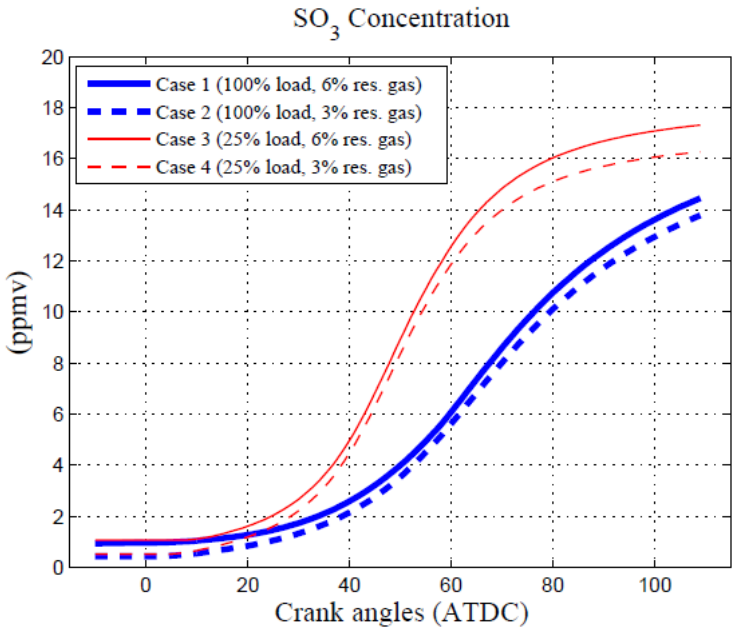

Figure 2. *Simulated SO_3 concentrations (average) of the studied cases in Table 2.*

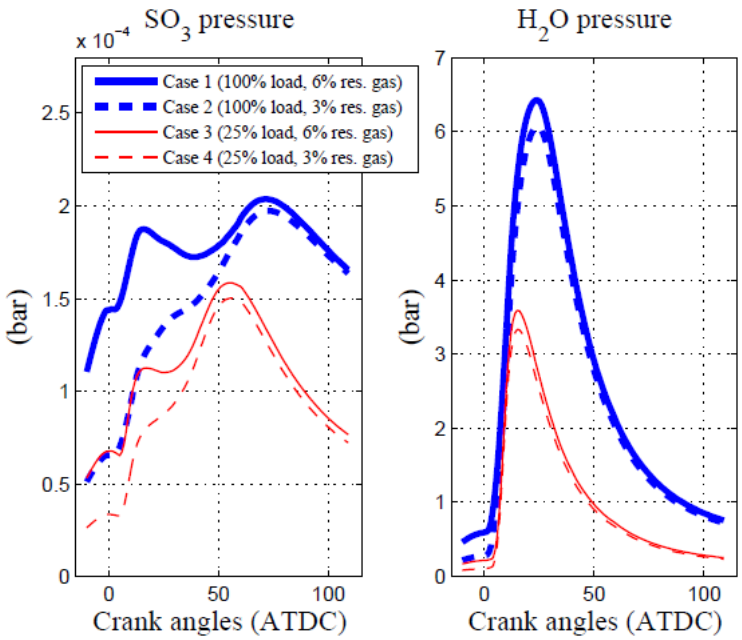

Figure 3. *Modeled SO_3 and H_2O pressures (average) of the studied cases in Table 2.*

The sulfuric acid dew points presented in Figure 4 are calculated with eq. 2 and are based on the SO_3 and H_2O pressure traces in Figure 3. Max dew points of typically more than 200 °C are located a little after TDC where the H_2O pressure is high. The ever reducing cylinder pressure during the expansion stroke provides that the acid dew point is comparably low even when SO_3 is formed in the cylinder gas (Fig. 2). Yet the acid dew point is strongly influ-

enced by the minor SO_3 concentrations as it clearly exceeds the dew point of H_2O as shown for case 1 and case 3 in Figure 4.
The dashed horizontal lines in Figure 4 represent constant liner temperatures of 170 °C and 210 °C that roughly correspond to 25 % and 100 % engine load respectively. The difference is rational but the liner temperature is highly variable in practice. It depends on the operating strategy and reduces from TDC and throughout the expansion stroke. Nevertheless the anticipated liner temperatures are reasonably applied to illustrate the characteristics of sulfuric acid condensation.
When the dew point is higher than the liner temperature sulfuric acid and water condense on the liner surface. Deposited liquid evaporates back into the gas phase if the dew point temperature is lower than the liner temperature. The liner area that is exposed to condensation scales with the number of crank angles between the point where condensation starts and stops. In case 3 the liner area is exposed to condensation from ≈5 - 70 CA ATDC. The higher liner temperature in case 1 provides that the exposed surface is comparably low (≈15 - 40 CA ATDC) despite a higher dew point trace. At both loads the exposed area increases slightly with the residual gas fraction and the exposed liner area can be reduced if the liner temperature is increased.
As shown in Figure 4 the dew point of H_2O remains lower than the anticipated liner temperatures. Consequently pure water does not condense on the liner under the given conditions. If pure water condenses the liquid acid will be highly diluted.

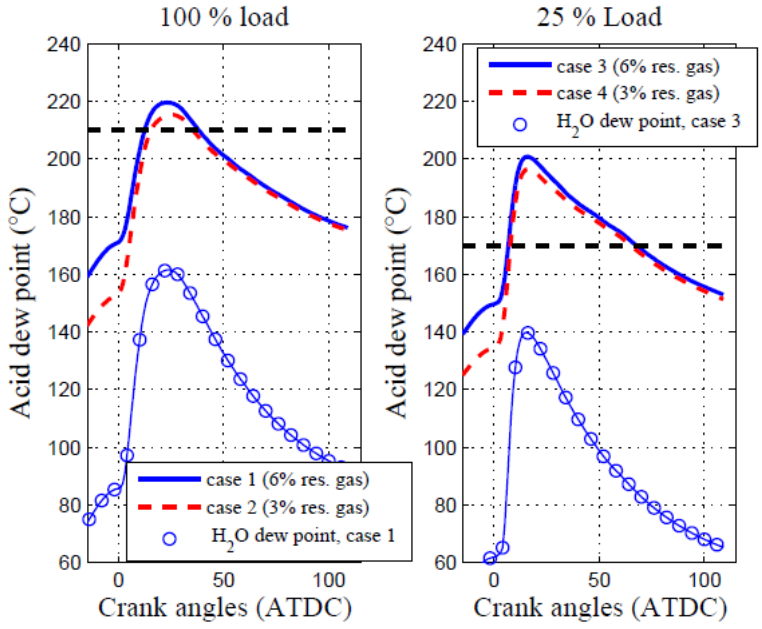

Figure 4. *Sulfuric acid dew points (average) of the studied cases in Table 2. The dashed horizontal lines represent constant cylinder liner temperatures of 170 °C and 210 °C.*

During a cycle the H_2O pressure is affected by the humidity of the intake air and the assumption of dry intake air conditions acts to underestimate real dew points since marine engines often operate in very humid environments. In Figure 5 the relative humidity (φ) of the intake air in case 3 is varied from 0 to 1. Engine simulations show that the SO_3 formation is weakly hampered by the humidity whereas the dew point temperature and the H_2O concentration is elevated as shown in Figure 5. The effect is most pronounced before TDC and the max dew point temperature is elevated ≈15 °C when the intake air is fully saturated instead of dry. In the remainder of the cycle the relative effect of the moist air reduces as H_2O forms

from the the fuel combustion. Nevertheless moist air increases the exposed liner area. At φ = 1 condensation of sulfuric acid initiates before TDC where the acid dew point exceeds the anticipated liner temp of 170 °C as seen in Figure 5.

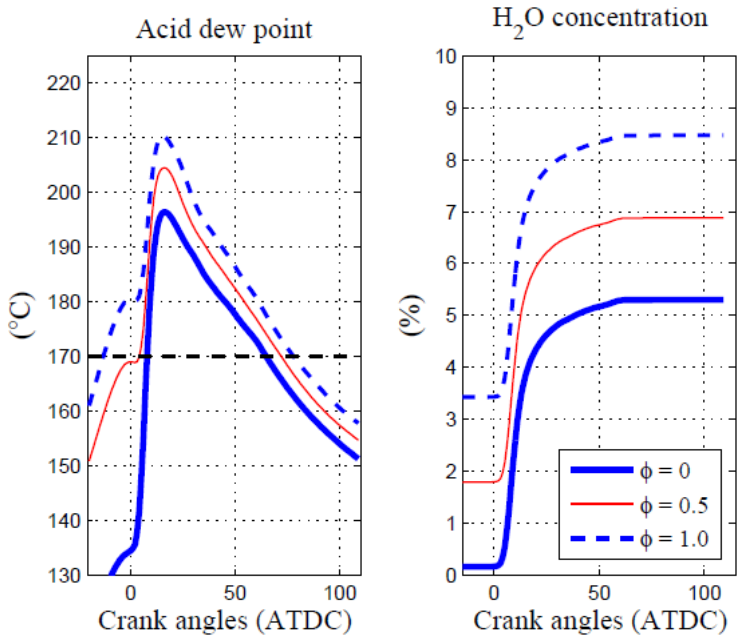

Figure 5. *Average sulfuric acid dew points and H_2O concentrations modeled at different intake air humidities (φ) for case 4 in Table 2. The dashed horizontal line represents a fixed cylinder liner temperature.*

The principles of condensation are illustrated in Figure 6. Close to the cooled liner surface SO_3 and H_2O from the bulk gas reacts instantly to form H_2SO_4. Together with H_2O the H_2SO_4 diffuses through the gaseous boundary layer to the gas liquid interface where the two compounds condense. Basically the H_2O and H_2SO_4 components are forced through the boundary layer due to partial pressure gradients. Transition from gas to liquid is not rate limiting [15] and phase equilibrium is assumed to exist at the interface.

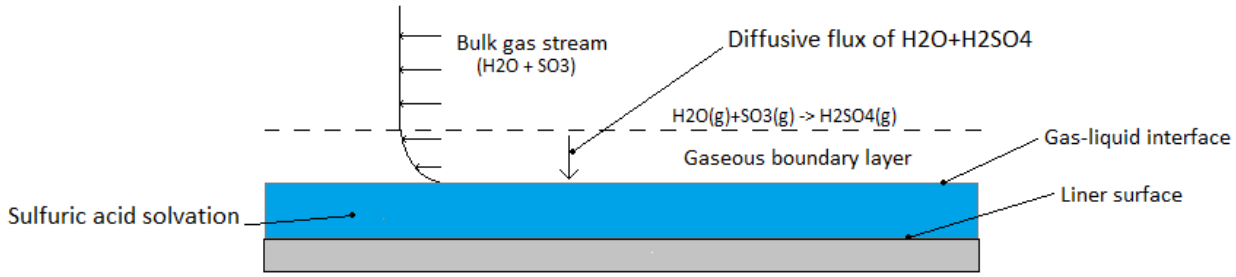

Figure 6. *The principles of H_2SO_4 and H_2O condensation on the cylinder liner.*

In order to determine the share of condensing H_2O and H_2SO_4 (eq. 2) one of these pressures are required at the gas liquid interface beside the liner temperature. The anticipated

liner temperatures are always higher than the dew point of H_2O and the H_2O contained in the bulk gas is orders of magnitude higher than the SO_3 content. As a result, the amount of H_2O that condenses together with H_2SO_4 is very small compared to the H_2O content in the bulk gas. For that reason the share of condensing H_2O and H_2SO_4 (acid strength) is reasonably determined (at each crank angle) from the assumption that the H_2O pressure at the gas-liquid interface equals the H_2O pressure in the bulk gas. Together with Müller's mass diffusion expressions in eq. 3 and 4 the condensing acid strength is used to calculate the condensation rates of H_2O and H_2SO_4. g_w and g_a denotes the transport/condensation rate of H_2O and H_2SO_4 respectively. In eq. 3 the H_2SO_4 pressure at the gas liquid interface ($p_{a,w}$) is found by applying the known acid strength (c_a) and the liner temperature to eq. 2. In eq. 4 the H_2O pressure at the interface ($p_{w,w}$) cannot be approximated by its pressure in the bulk gas ($p_{w,b}$) as before since one would have to evaluate ln(1)=0. Instead the definition of the condensing acid strength in eq. 5 is applied. Hereby the system of equations 3-5 that comprises the three unknowns g_a, g_w and $p_{w,w}$ can be solved.

Consistent with the heat and mass transfer analogy the rates in eq. 3 and 4 scale with the heat transfer coefficient (h) that is determined by Woschnis heat transfer correlation [16]. The coefficient is closely coupled to the system pressure and reduces throughout the expansion stroke after peaking around max pressure. The rate expressions also involve diffusion coefficients of H_2O and H_2SO_4 (k_w and k_a respectively). k_a is approximated by the binary diffusion coefficient of H_2SO_4 in a large excess of air [18] at 296 K (k_a = 0.08 atm cm^2 s^{-1}). Combined with the binary diffusion coefficient of H_2O in air [19] at 293 K (k_w = 0.260 atm cm^2 s^{-1}) the aspect ratio of k_w/k_a is around 3. If the coefficients are equally dependent on temperature and pressure the ratio is not altered throughout the engine cycle. In any case the condensation rates of the present study are highly independent of k_w/k_a ratios up to 100.

$$g_a = g_w \frac{k_w}{k_a}\frac{R_w}{R_a}\frac{\frac{p_{a,b}}{p}-\frac{p_{a,w}}{p}\left(\frac{p-p_{w,b}}{p-p_{w,w}}\right)^{\frac{k_w}{k_a}}}{1-\left(\frac{p-p_{w,b}}{p-p_{w,w}}\right)^{\frac{k_w}{k_a}}} \quad (3)$$

$$g_w = h\frac{R_g}{R_w c_{p,g}} ln\left(\frac{p-p_{w,w}}{p-p_{w,b}}\right) \quad (4)$$

$$c_a = \frac{g_a}{g_a+g_w} \quad (5)$$

Modeled rates of H_2SO_4 condensation over the expansion stroke are presented in Figure 7. A similar plot could be shown for H_2O condensation but is omitted. The condensation rates are expressed in mg/m^2 (deposited mass per exposed liner area) which means that the results of case 3 and 4 benefit from a lower engine speed compared to case 1 and 2. Condensation takes place when $g_a > 0$. When g_a is negative liquid H_2SO_4 evaporates from the liner surface and into the gas phase. In line with the dew point traces in Figure 4 the onset of

condensation is located a little after TDC in case 3 and 4. In case 1 and 2 the onset is "delayed" a few crank angles due to the higher liner temperature. With reference to the SO_3 concentrations in Figure 2 it is understood that the high condensation rates at ≈20 CA ATDC are realized by the SO_3 from the residual gasses combined with a high operating pressure and heat transfer rate. The rate reduces during the expansion stroke. However the deposition of acid increases significantly as the piston moves away from TDC due to the rapidly increasing surface area.
The liner temperature of 210 °C in case 1 and 2 provides that the evaporation of deposited sulfuric acid initiates before any significant SO_3 has yet been formed. A lower liner temperature involves more crank angles/time before the evaporation begins and the deposition of acid in case 3 and case 4 significantly profits from the SO_3 formed in the combustion products. As indicated in Figure 7 the rate of condensation represents large negative numbers during the gas compression (crank angles ATDC < 0) and late in the expansion stroke. Deposited acid will under the given conditions evaporate completely before condensation starts in the following cycle.

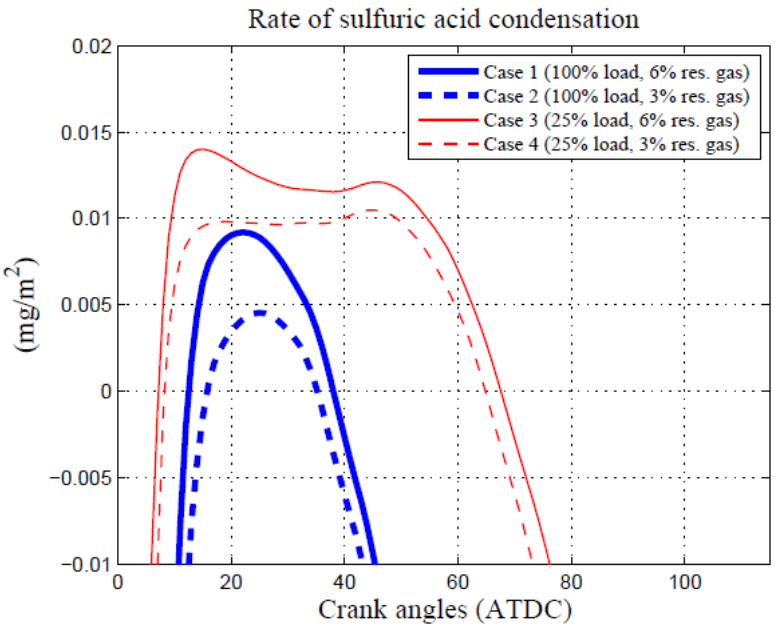

Figure 7. *Rate of H_2SO_4 condensation (average) on the cylinder liner for the studied cases in Table 2.*

To isolate the effect of the liner temperature in terms of sulfuric acid condensation the operating conditions of case 4 are used with two additional liner temperatures of 160 °C and 180 °C as seen in Figure 8. The initial deposition rates (around max pressure) are basically unchanged. However the traces in the figure illustrate that the exposed liner area is very sensitive to the liner temperature. At 160 °C condensation takes place over more than 80 crank angles ATDC. Moreover the impact from SO_3 formed in the current engine cycle increases when the liner temperature reduces. This is illustrated by the size of the peak rate that develops during the expansion stroke when temperature is lowered.

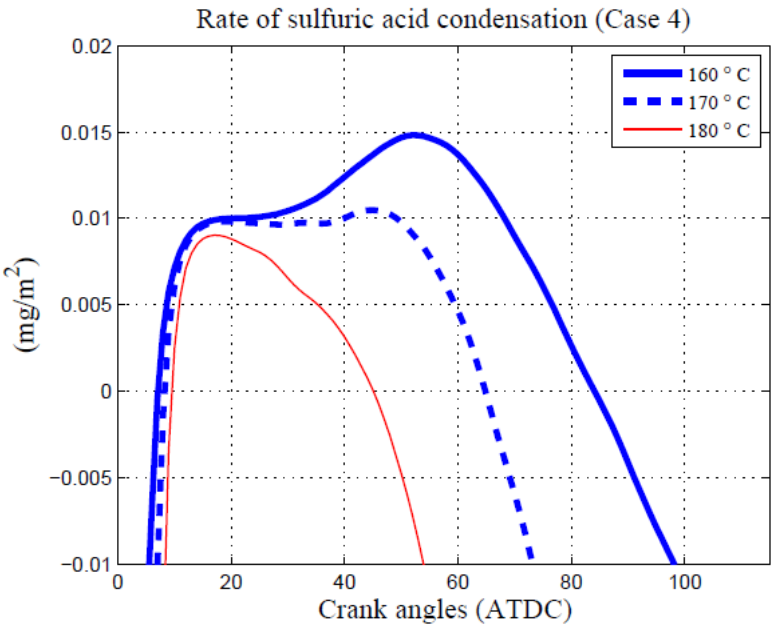

Figure 8. *Rate of H_2SO_4 condensation (average) on the cylinder liner for case 4 in Table 2. The legends refer to a constant liner temperature.*

The accumulated sulfuric acid mass over the expansion stroke until EVO are illustrated in Figure 9. The traces in the figure are at a max when the evaporation of acid begins. From the assumption that the condensate is uniformly distributed on the exposed liner area the following removal/evaporation of acid is completed after ≈20-25 crank angles as seen in the figure. The influence of the operating conditions becomes clearer when the peak points in Figure 9 are compared. At 100 % engine load (case 1 and 2) the high liner temperature provides that the exposed liner area is comparably small and the resulting acid mass is low. Nevertheless if the residual gas fraction is reduced from 6 % to 3 % the mass of condensate is reduced by ≈ 60 %. At 25 % engine load (case 3 and 4) the SO_3 forming in the combustion products significantly adds to the deposition of acid due to the lower liner temperature. At the same time the effect of the higher residual gas fraction is reduced to ≈22 %. The lower engine speed at 25 % engine load (Table 2) implies that the number of operating cycles is reduced by 1/3 relative to 100 % load. As a result the weight of case 3 and 4 should be reduced accordingly. Nonetheless the deposited mass per time unit will under the given conditions will still be several times higher at 25 % load.

Case 4^* in Figure 9 are based on the same operating conditions as case 4 but the liner temperature is reduced by 10 °C to 160 °C. The difference between case 4 and 4^* illustrates the influence of the temperature/exposed liner area. At the reduced temperature the deposited acid mass increases by a factor of more than 2 under the given conditions.

As shown in Figure 5 moisturized intake air elevates the exposed surface area through a higher dew point trace. Case 4^{**} in Figure 9 represents the same operating conditions as case 4 but the intake air is saturated. As illustrated the moist air basically doubles the deposited acid mass under the given conditions.

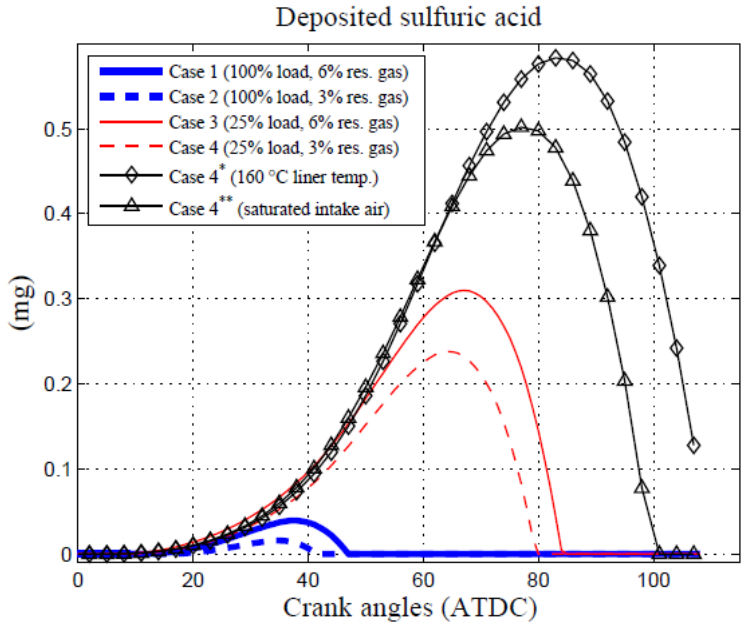

***Figure 9**. Deposited acid on the cylinder liner of the studied cases in Table 2. *The liner temperature is 160 °C instead of 170 °C. **The intake air is saturated.*

In Figure 10 the fraction of fuel sulfur that is converted to corrosive species (ε) at EVO is plotted against the fuel sulfur content. The results represent the operating conditions of case 4 in Table 2. In the typical fuel sulfur range from 1 - 4 % m/m the ε-value decreases slightly. As the sulfur content approaches very low numbers the ε-value tends to increase asymptotically, yet the presence of SO_3 in the cylinder gas will disappear in line with the vanishing sulfur content. Under the given conditions the combined effect of higher SO_3 pressures and exposed liner areas provides that the deposition of sulfuric acid scales with a quadratic regression of the sulfur content as illustrated in the figure.

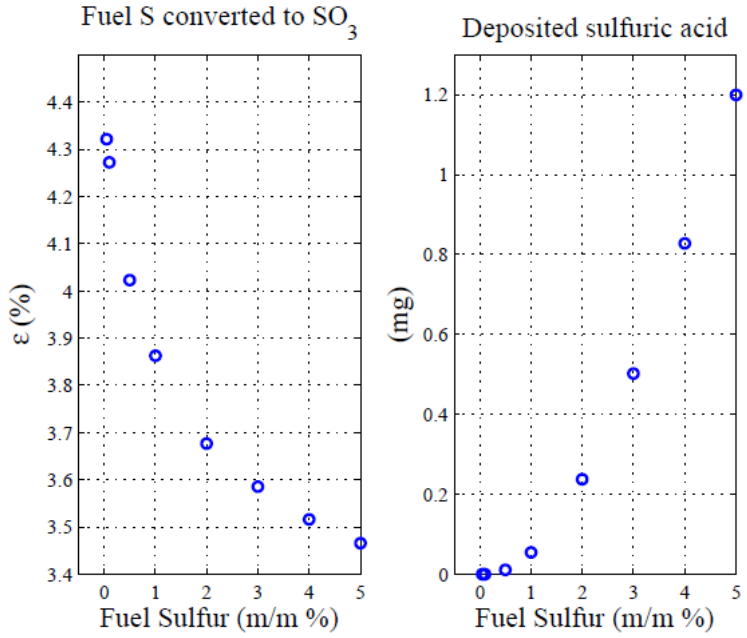

***Figure 10**. Fraction of fuel sulfur converted to corrosive species and deposited sulfuric acid on the cylinder during a cycle. The figures represent operating conditions at 25 % engine load.*

5. Discussion

With respect to sulfuric acid condensation on a marine engine cylinder liner the applied assumption of a homogenous cylinder gas mixture is not truly representative. The actual gas conditions of the mixing controlled combustion process are clearly heterogeneous in terms of composition and turbulence intensity etc. This challenges the modeled dew points and acid deposition rates. Moreover to the author's knowledge the applied thermochemistry of the H_2O-H_2SO_4 is system not directly validated against experimental measurements of sulfuric acid dew points.
In the present work the liner temperature is constant throughout the expansion stroke where condensation takes place. The actual temperature profile is highly variable. It depends on the operating strategy and reduces from TDC towards the bottom dead center. In practice the condensation of acid will strongly depend on the resulting liner temperature profile.
In this work the residual gas fraction and intake air humidity significantly alters the deposition of sulfuric acid. However if the actual liner temperature is generally lower than the acid dew point throughout the expansion stroke the influence of these conditions will decrease. In addition the accumulated acid mass on the liner can be considerably higher than predicted in this work because a larger liner area is exposed to condensation at lower liner temperatures.
A flue gas that contains SO_3 can form an acid mist if it is abruptly cooled below the acid dew point [20]. This may occur in practice when hot gas products reach the cooled liner surface. Mist formation is not treated in this work and the applied analogy between heat and mass transfer may overestimate the rate of acid condensation as the mist tends to stay in the bulk gas.

6. Conclusions

Formation of SO_3 in a large two-stroke marine engine is modeled with a multizone engine model and combined with diffusive mass transfer theory in order to examine the characteristics of sulfuric acid condensation on the cylinder liner. The liner is assumed to have a constant temperature over the full stroke. I.e. 170 °C and 210 °C at 25 % and 100 % engine load respectively. Sulfuric acid dew points are calculated from the thermochemistry of the two-phase H_2O-H_2SO_4 system. Acid dew points and condensation rates are based on a homogenous cylinder gas mixture. The reaction between H_2O and SO_3 instantly forms H_2SO_4 at the cooled liner surface. Thus SO_3 and H_2SO_4 are lumped together.
SO_3 from the residual gasses provides that the sulfuric acid dew point peaks close to max cylinder pressure at temperatures of typically more than 200 °C. Under the given conditions the condensation of sulfuric acid is very sensitive to the operating strategy. The operating pressure, fuel sulfur content and residual gas fraction elevates the SO_3 pressure that increases the rate of condensation as well as the acid dew point. When the dew point trace is elevated a larger liner area is exposed to condensation from which the deposition of acid can increase remarkably. Similarly the deposition increases with the charge air humidity.
In order to counteract condensation of acid the liner temperature is essential as it determines the size of the exposed liner area. Even a small reduction of the liner temperature will under the given conditions significantly increase the deposition of acid.

Nomenclature

Symbol		Unit
c_a	Condensing acid strength	kg/kg
$c_{p,g}$	Specific heat capacity of gas	J/kg-K
g_a	Rate of condensing sulfuric acid	mg/m^2-s
g_w	Rate of condensing water	mg/m^2-s
h	Heat transfer coefficient	W/m^2-K
k_a	Binary diffusion coefficient of H_2SO_4 in air	atm cm^2 /s
k_w	Binary diffusion coefficient of H_2O in air	atm cm^2 /s
$p_{a,b}$	Partial pressure of H_2SO_4 in bulk gas	Pa
$p_{a,w}$	Partial pressure of H_2SO_4 at gas-liquid interface	Pa
P_{boost}	Boost/charge air pressure	bar
$p_{w,b}$	Partial pressure of H_2O in bulk gas	Pa
$p_{w,w}$	Partial pressure of H_2O at gas-liquid interface	Pa
p_i^0	Vapor pressure of a pure substance	Pa
R_a	Specific gas constant of H_2SO_4	J/kg-K
R_w	Specific gas constant of H_2O	J/Kg-K
R_g	Specific gas constant of cylinder gas	J/Kg-K
T	Temperature	K
T_{air}	Charge air temperature	°C
x_i	Mole fraction in the liquid solvation	-
x_{res}	Residual gas fraction	% m/m
γ_i	Activity coefficient	-
ε	Fraction of fuel sulfur converted to SO_3	-
λ_t	Trapped excess air ratio	-

Abbreviations

ATDC	After top dead center
EVO	Exhaust valve opening
rpm	Revolutions per minute
S	Sulfur
TDC	Top dead center

Literature

[1] Cordtz, R.; Schramm, J.; Andreasen, A.; Eskildsen, S. S.; Mayer, S. Modeling the distribution of sulfur compounds in a large two stroke diesel engine. *Energy Fuels* **2013**, *27*, 1652-1660.

[2] Cordtz, R.; Schramm, J.; Rabe, R. Investigating SO_3 Formation from the Combustion of Heavy Fuel Oil in a Four-Stroke Medium-Speed Test Engine. *Energy and Fuels* **2013**, *27*.

[3] Verhoff, F. H.; Banchero, J. T. Predicting Dew Points of Flue Gases. *Chem. Eng. Prog.* **1974**, *70*, 71-72.

[4] Pierce, R. Estimating Acid Dewpoints in Stack Gases. *Chem. Eng.* **1977**, *84*, 125-128.

[5] Abel, E. The Vapour-phase above the System Sulphuric Acid-Water. *J. Phys. Chem.* **1946**, *50*, 260.

[6] Greenewalt, C. H. Partial pressure of water out of aqueous solutions of sulfuric acid. *Ind. Eng. Chem.* **1925**, *17*, 522-523.

[7] Gmitro, J. I.; Vermeulen, T. Vapor-Liquid Equilibria for Aqueous Sulfuric Acid. *A. I. Ch. E J.* **1964**, *10 No 5*, 740-746.

[8] Wilson, R. W.; Stein, F. P. Correlation of sulfuric acid-water partial pressures. *Fluid Phase Equilib.* **1989**, *53*, 279-288.

[9] Pessoa, F. L. P.; Siqueira Campos, C. E. P.; Uller, A. M. C. Calculation of vapor-liquid equilibria in aqueous sulfuric acid solutions using the UNIQUAC equation in the whole concentration range. *Chemical Engineering Science* **2006**, *61*, 5170-5175.

[10] Bosen, A.; Engels, H. Description of the phase equilibrium of sulfuric acid with the NRTL equation and a solvation model in a wide concentration and temperature range. *Fluid Phase Equilib.* **1988**, *43*, 213-230.

[11] Nist Chemistry WebBook: http://webbook.nist.gov/chemistry/.

[12] Luchinskii, G. P. Physical-chemical Study of the H2O-SO3 System, I. Equilibrium in the vapor and the liquid phase. *Zh. Fiz. Khim.* **1956**, *30*, 1207.

[13] Renon; Prausnitz Local compositions in thermodynamic excess functions for liquid mixtures. *AIChE J.* **1968**, *14*, 135-144.

[14] Hindiyarti, L.; Glarborg, P.; Marshall, P. Reactions of SO3 with the O/H radical pool under combustion conditions. *J. Phys. Chem. A* **2007**, *111*, 3984-3991.

[15] Mueller, P. Dew point temperatures in cylinders of diesel engines working with fuel that contains sulfur (Taupunkttemperaturen im Zylinder von Dieselmaschinen bei schwefelhaltigen Kraftstoffen, Nr 486). *VDI -- Forschungsheft* **1961**, *27*, 1-56.

[16] Ferguson, C. R.; Kirkpatrick, A. T., Eds.; *Internal combustion engines / applied thermosciences;* Wiley: New York, 2001; .

[17] Andreasen, A.; Mayer, S. Modeling of the Oxidation of Fuel Sulfur in Low Speed two-Stroke Diesel Engines. In *26 CIMAC World Congress*; CIMAC: Bergen, 2010; .

[18] Poschl, U.; Canagaratna, M.; Jayne, J. T.; Molina, L. T.; Worsnop, D. R.; Kolb, C. E.; Molina, M. J. Mass Accommodation Coefficient of H2SO4 Vapor on Aqueous Sulfuric Acid Surfaces and Gaseous Diffusion Coefficient of H2SO4 in N2/H2O. *J. Phys. Chem.* **1998**, *102*, 10082.

[19] Reid, R. C.; Sherwood, T. K., Eds.; *The properties of gases and liquids. Their estimation and correlation;* McGraw-Hill Book Company: New York, 1958; .

[20] Land, T. Theory of Acid Deposition and its Application to the Dew-Point Meter. *J. Inst. Fuel* **1977**, *50*, 68-75.

The rate of a chemical reaction is described via the Arrhenius expression in eq. A.1.

$$k_f = A \cdot T^{\beta} exp\left(-\frac{E}{RT}\right) \quad \text{(A.1)}$$

Forward and backward rates are related through the equilibrium constant K_c in units of concentration as shown in eq. A.2.

$$k_b = \left(\frac{k_f}{K_c}\right) \quad \text{(A.2)}$$

The relationship between the equilibrium constant in concentration units and in pressure units is expressed in eq. A.3

$$K_c = K_p \left(\frac{P^o}{RT}\right)^{\sum_1^n v_n} \quad \text{(A.3)}$$

The equilibrium constant in pressure units is given by eq. A.4 where The Δ refers to the change that occurs in passing completely from reactants to products in the reaction.

$$K_p = \exp\left(\frac{\Delta S^o}{R} - \frac{\Delta H^o}{T}\right) \quad \text{(A.4)}$$

$$\frac{\Delta S^o}{R} = \sum_1^n v_n \frac{{s_k}^o}{R}$$

$$\frac{\Delta H^o}{RT} = \sum_1^n v_n \frac{{H_k}^o}{RT}$$

DTU Mechanical Engineering
Section of Thermal Energy
Technical University of Denmark

Nils Koppels Allé, Bld. 403
DK- 2800 Kgs. Lyngby
Denmark
Phone (+45) 4525 4131
Fax (+45) 4588 4325
www.mek.dtu.dk
ISBN: 978-87-7475-421-3

DCAMM
Danish Center for Applied Mathematics and Mechanics

Nils Koppels Allé, Bld. 404
DK-2800 Kgs. Lyngby
Denmark
Phone (+45) 4525 4250
Fax (+45) 4593 1475
www.dcamm.dk
ISSN: 0903-1685